Iowa Research Online
The University of Iowa's Institutional Repository

University of Iowa
Iowa Research Online

Theses and Dissertations

2013

New algorithms for in vivo characterization of human trabecular bone: development, validation, and applications

Yinxiao Liu
University of Iowa

Copyright 2013 Yinxiao Liu

This dissertation is available at Iowa Research Online: http://ir.uiowa.edu/etd/1679

Recommended Citation
Liu, Yinxiao. "New algorithms for in vivo characterization of human trabecular bone: development, validation, and applications." PhD (Doctor of Philosophy) thesis, University of Iowa, 2013.
http://ir.uiowa.edu/etd/1679.

Follow this and additional works at: http://ir.uiowa.edu/etd

Part of the Electrical and Computer Engineering Commons

NEW ALGORITHMS FOR IN VIVO CHARACTERIZATION OF HUMAN TRABECULAR BONE: DEVELOPMENT, VALIDATION, AND APPLICATIONS

by

Yinxiao Liu

A thesis submitted in partial fulfillment
of the requirements for the Doctor of
Philosophy degree in Electrical and Computer Engineering
in the Graduate College of
The University of Iowa

December 2013

Thesis Supervisor: Professor Punam K. Saha

Copyright by

YINXIAO LIU

2013

All Rights Reserved

Graduate College
The University of Iowa
Iowa City, Iowa

CERTIFICATE OF APPROVAL

PH.D. THESIS

This is to certify that the Ph.D. thesis of

Yinxiao Liu

has been approved by the Examining Committee
for the thesis requirement for the Doctor of Philosophy
degree in Electrical and Computer Engineering at the December 2013
graduation.

Thesis Committee: _____
Punam K. Saha, Thesis Supervisor

_____
Milan Sonka

_____
Joseph Reinhardt

_____
Nicole Grosland

_____
Steven M. Levy

For my parents Zhang Liu and Jianping Wang

ACKNOWLEDGMENTS

After six years, Iowa City is the place where I have spent the longest time ever besides my hometown. It is not just a span of time to pursue a Ph.D. degree, but a lifelong memory and treasure that I will cherish and enjoy. It is my great fortune to be here in the University of Iowa and meet the important people who will influence my whole life. The best and worst of my Ph.D. life were shared with them. I want to thank all those who ever and are still giving me help, bringing me happiness and enlightening my future.

Above all, the most important person I want say thank you is my advisor, Dr. Punam K. Saha, without whose guidance and help, the path for me will be much harder during my six year of Ph.D. study. He patiently provided the vision, encouragement and advice necessary for me to go through the program and complete my dissertation. He would help me hand by hand when I got stuck at the beginning of the program, and he would trust me to take charge of a project when I became senior. And I greatly appreciate the advice he gives me in both work and life which will benefit my whole life, just like an old friend. His spirit, hardworking attitude, intelligence, carefulness and pursuing of perfection really impresses and changes me all the time. It is my great honor to finish my degree under his instruction.

Special thanks to my committee members, Dr. Milan Sonka, Dr. Joseph M. Reinhardt, Dr. Nicole Grosland, and Dr. Steven M. Levy for their support, guidance and helpful suggestions. Their guidance has served me well and I owe them my heartfelt appreciation. Also, I want to thank Dr. Xiaodong Wu and Dr. Ei-wei Bai for serving on my Master defense committee and providing me valuable suggestions in May 2009.

Sincere acknowledgement goes to all my lab members, Zhiyun Gao, Ziyue Xu, Guoyuan Liang, Yan Xu, Weichen Gao, Cheng Li, Dakai Jin, Cheng Chen and other colleagues Qi Song, Kunlin Cao, Xin Dou, Ying Wei, Mingqing Chen, Honghai Zhang,

Shanhui Sun, Ping Yu and Cheng Zhang. It is because of you that my life here is enriched, and full of beautiful memories.

I would also like to thank the department secretary Catherine Kern and the administrative assistant Dina Blanc for their patient assistance.

Most of all thanks are for my parents and other family members. It is impossible for me to go this far without their love and support.

This work has been partially supported by internal funds from the Departments of Radiology and Electrical & Computer Engineering at the University of Iowa.

ABSTRACT

Osteoporosis is a common bone disease that increases risk of low-trauma fractures associated with substantial morbidity, mortality, and financial costs. Clinically, osteoporosis is defined by low bone mineral density (BMD). BMD explains approximately 60-70% of the variance in bone strength. The remainder is due to the cumulative and synergistic effects of other factors, including trabecular and cortical bone micro-architecture. In vivo quantitative characterization of trabecular bone (TB) micro-architecture with high accuracy, reproducibility, and sensitivity to bone strength will improve our understanding of bone loss mechanisms and etiologies benefitting osteoporotic diagnostics and treatment monitoring processes.

The overall aim of the Ph.D. research is to design, develop and evaluate new 3-D imaging processing algorithms to characterize the quality of TB micro-architectural in terms of topology, orientation, thickness and spacing, and to move the new technology from investigational research into the clinical arena. Two algorithms regarding to this purpose were developed and validated in detail – (1) star-line-based TB thickness and marrow spacing computation algorithm, and (2) tensor scale (t-scale) based TB topology and orientation computation algorithm.

The TB thickness and marrow spacing algorithm utilizes a star-line tracing technique that effectively accounts for partial voluming effects of in vivo imaging with voxel size comparable to TB thickness and also avoids the problem of digitization associated with conventional algorithms. Accuracy of the method was examined on computer-generated phantom images while the robustness of the method was evaluated on human ankle specimens in terms of stability across a wide range of resolutions, repeat scan reproducibility under in vivo condition, and correlation between thickness values computed at ex vivo and in vivo resolutions. Also, the sensitivity of the method was examined by its ability to predict bone strength of cadaveric specimens. Finally, the

method was evaluated in an in vivo human study involving forty healthy young-adult volunteers and ten athletes.

The t-scale based TB topology and orientation computation algorithm provides measures characterizing individual trabeculae on the continuum between perfect plate and perfect rod as well as individual trabecular orientation. Similar to the TB thickness and marrow spacing computation algorithm, accuracy was examined on computer-generated phantoms while robustness of the algorithm across ex vivo and in vivo resolution, repeat scan reproducibility, and the sensitivity to experimental mechanical bone strength were evaluated in a cadaveric ankle study. And the application of the algorithm was evaluated in a human study involving forty healthy young-adult volunteers and ten patients with SSRI treatment.

Beside these two algorithms, an image thresholding algorithm based on the class uncertainty theory is developed to segment TB structure in CT images. Although the algorithm was developed for this specific application, it also works effectively for general 2-D and 3-D images. Moreover, the class uncertainty theory can be utilized as adaptive information in more sophisticated image processing algorithms such as Snakes, ASMs and graph search.

TABLE OF CONTENTS

LIST OF TABLES ix

LIST OF FIGURES x

CHAPTER

I. INTRODUCTION 1

1.1 Specific Aims 2
1.2 Trabecular Bone, Osteoporosis and Diagnosis 6
1.2.1 Bone Density and Trabecular Architecture 6
1.2.2 Recent Study of Osteoporosis Imaging 8
1.2.3 Image-based Approaches to TB Architecture 11
1.3 Digital Topological Analysis 14
1.4 TB Thickness and Marrow Spacing Computation 15
1.5 Tensor Scale 16
1.6 TB Segmentation 18
1.7 Skeletonization and Back Propagation 19
1.8 Experimental Plan 20

II. QUANTITATIVE CHARACTERIZATION OF TRABECULAR BONE THICKNESS AND MARROW SPACING 24

2.1 Definition of Thickness at Individual Location 24
2.2 Thickness Computation Algorithm 28
2.3 Improved Feature Propagation Algorithm 32
2.4 Experimental Plan 34
2.4.1 Cadaveric specimens and MD-CT and μ-CT imaging 36
2.4.2 Mechanical testing and determination of bone strength 36
2.4.3 Human volunteers for the *in vivo* study 38
2.4.4 Image processing 39
2.4.5 VOI selection for the cadaveric study on bone strength prediction 39
2.4.6 Individual-specific VOI selection for the *in vivo* pilot study 40
2.5 Results 40
2.5.1 Accuracy results 41
2.5.2 Robustness under various conditions 45
2.5.3 Reproducibility analysis 49
2.5.4 Predicting bone strength 51
2.5.5 Results of *in vivo* pilot study 53
2.6 Conclusion 56

III. TENSOR-SCALE-BASED QUANTITATIVE ANALYSES OF TRABECULAR BONE MICRO-ARCHITACTURE 57

3.1 Tensor Scale Computation 57
3.2 Characterization of Individual Trabeculae 62
3.3 Experimental Plan 66

3.4 Results 66
3.4.1 Accuracy results 68
3.4.2 Robustness under various conditions 70
3.4.3 Reproducibility analysis 72
3.4.4 Predicting bone strength 73
3.4.5 Results of *in vivo* pilot study 75
3.5 Conclusion 77

IV. TRABECULAR BONE THRESHOLDING 79

4.1 Class Uncertainty 81
4.2 Optimum Threshold Selection 86
4.3 Experimental Plan and Results 90
4.3.1 Accuracy analysis 92
4.3.2 Reproducibility analysis 96
4.4 Conclusion 98

V. DISCUSSION AND FUTURE WORK 100

5.1 Ultimate Goal the Research 100
5.2 Limitation of the Current Research 101
5.3 Possible Future Research Work 103

REFERENCES 105

LIST OF TABLES

Table

1. Computation error of thickness for different parameters.....43

2. Results of linear correlation (R^2 values) between TB thickness and marrow spacing measures and experimental TB strength parameters 52

3. Results of linear correlation (R^2 values) of different TB measures between MD-CT and μ-CT 72

4. Results of linear correlation (R^2 values) between different TB measures and experimental TB strength parameters.. 74

5. Results of "leave-one-out" method for different TB measures in predicting bone strengths 75

LIST OF FIGURES

Figure

1. 3D rendered of a trabecular bone sample. The bone sample displayed on the right predominantly contains rod-like trabeculae while the left one on the right mostly consists of plates.....11

2. Comparison among different definitions of thickness in terms of satisfying Property 1. (a) Local thickness distribution on an ellipse using the largest MIB option except that the intensity at an axial point a is enforced as the diameter of the MIB centered at that point. (b-d) Same as (a) but for thickness computation using the options of smallest MIB (b), nearest MIB center (c), and farthest MIB circumference (d). Axial lines are partially visible in (a,b) indicating the failure of the corresponding thickness definitions in satisfying Property 1. The axial lines in (c,d) are not visible indicating that both the nearest MIB center and the farthest MIB circumference options satisfy Property 1.....27

3. Comparison among different definitions of thickness in terms of their performance for two overlapping disks of different scales. Disk boundaries are shown by dotted lines. (a) Local thickness distribution using the largest MIB option. Here, the larger ball gets higher preference and it enters inside the smaller ball. (b) Same as (a) but for the smallest MIB option; here, the artifact just opposite of that of (a). (c) Same as (a) but using the MIB with the nearest center. The failure of this option is obvious. (d) Same as (a) but using the MIB with the farthest circumference. A major advantage of this option is that it divides the intersecting regions between the two balls eliminating bias artifacts.....28

4. Illustration of star line-based TB thickness in two-dimensions. Candidate point (red), star lines (blue), edge locations (purple) and shortest intercept (orange) in TB thickness computation are shown. 32

5. Compressive mechanical testing of TB specimens. (a) Extensometertesting. (b) Nonextensometer testing; note black lines indicating original extensometer position, with damaged bone removed from the bottom (proximal part) of the specimen.....38

6. Illustration of the TB thickness and marrow spacing measures for three different TB specimens – (a) strong (yield stress: 11.5 MPa), (b) moderate (7.1 MPa) and (c) weak (3.4 MPa) 41

7. Computer-generated phantoms data at different levels of noise and down sampling. (a) Three-dimensional rendition of the true binary phantom. (b-d)

Axial image slices of test phantoms at SNR values of 24, 12 and 6 and down-sampling rates of three, four, and five voxels 43

8. Illustration of the error rate against down-sampling rate between the proposed method and the FDT-based methods. 45

9. Illustration of the μ-CT down sampled at different levels of resolution: (a) 28.5 μm, (b) 114.0 μm, and (c) 199.5 μm 47

10. Illustration of the stability of the new algorithm across different image resolutions. (a) The mean thickness τ_O over a cylindrical VOI change as the resolution changes. (b) The Error of the mean thickness value τ_O as the resolution changes compared to the average thickness from all ten images 47

11. Illustration of matched axial image slices from post-registered μ-CT and MD-CT images of a cadaveric specimen: (a) μ-CT and (b) MD-CT 48

12. Illustration of the linear correlation of TB thickness and marrow spacing computed from post-registered μ-CT and MD-CT images: (a) TB thickness and (b) marrow spacing. 49

13. Illustration of reproducibility of the TB thickness measure under repeat MD-CT scans. (a-b) color coded trabecular bone thickness images. (c-d) trabecular bone image without color coding. (e) color coding bar. Specimens were repositioned on the CT table before each repeat scan 50

14. Illustration of repeat MD-CT scan ICC values at different VOI diameters using both the new algorithm and FDT-based algorithm. As displayed, at a VOI diameter of 3.45 mm or greater, the ICC value using the new algorithm exceeded the mark of 0.95, while the TB thickness measure using the FDT-based algorithm requires a VOI diameter of 6.15 mm or greater 51

15. Ability of different TB measures using the new algorithm to predict bone strength shown in terms of R^2 values of linear correlation between yield stress and each of TH_B (a) and SP_M (b). (c,d) Same as (a,b) but for the FDT-based method [116] 52

16. Illustration of the new thickness computation algorithm for in vivo imaging on an age-BMI-similar female and male pair: (a) female healthy volunteer and (b) male healthy volunteer. 54

17. Same as Figure 16, but comparison between an age-sex-BMI-similar athlete and a non-athlete: (a) non-athlete and (b) athlete 55

18. 2D Illustration of steps in t-scale computation. (a) Radially opposite sample line pairs (blue) with the candidate point as origin (red), edge points (pink) on radial sample lines (blue) and repositioned edge points (yellow) from the center point (red). (b) The edge point and repositioned edge points (gray) are

translated the original and rotated to align with the coordinate axis (white) after applying PAC on the points, bounding box (dotted) and the best-fit ellipse (grey) (c) Final t-scale ellipsoid (green) 58

19. Illustration of the t-scale ellipsoid fits for different points on the TB structure. To obtain accurate descriptions of local dimensions, these measures must be derived from the mid-point of the respective dimension. (a) A generic trabeculae with sample points defined on the surface skeleton, r, the arc skeleton, q, and defined at the central point on the structure, p. (b) T-scale accurately captures the thickness information only when considering an arbitrary point on the surface skeleton; (c) captures the thickness and width information when considering a point on the arc skeleton; and (d) captures all three dimensions when considering the central point 62

20. Characterization of TB structure analysis using the t-scale. (a) One TB region selected from μ-CT image of a human ankle specimen. (b) TB orientation analysis using t-scale. (c) Color-coding for (b). (d-e) TB characterization on the continuum be-tween a perfect plate (green) and a perfect rod (red) using the t-scale (d) and VTA (e). (f) Color-coding for (d-e). 67

21. Illustration of the t-scale plate measure for three different TB specimens - (a) strong (Yield stress: 11.1MPa), (c) moderate (7.1MPa) and (d) weak (3.4 MPa). (b) Color bar 68

22. Results of linear correlation analysis between true structure width and computed width using t-scale and VTA methods on computational phantoms 69

23. Illustration of error rate for different phantoms using t-scale and VTA 70

24. Illustration of the stability of the t-scale algorithm across different image resolutions. (a-c) The mean plate width measures SW_{TS} (a), the mean surface to curve ratio SCR_{TS} (b) and longitudual bone volume fraction $BMDl_{TS}$ (c) over a cylindrical VOI change as the resolution changes. (d-f) The Errors of the corresponding measures SW_{TS} (d), SCR_{TS} (e), and $BMDl_{TS}$ (f) as the resolution changes compared to the average thickness from all ten images. 71

25. Illustration of repeat MD-CT scan ICC values at different VOI diameters using both the t-scale and VTA. (a) At a VOI diameter of 1.05 mm or greater, the ICC value of plate surface width SW_{TS} using t-scale exceeded the mark of 0.95, while the measure using VTA requires a VOI diameter of 3.15 mm or greater. (b) At a VOI diameter of 3.15 mm or greater, the ICC value of surface to curve ratio SCR_{TS} using both t-scale and VTA exceeded the mark of 0.95. (c) The ICC value of longitudual bone volume fraction $BMDl_{TS}$ at different VOI diameters 73

26. Ability of different TB measures using the t-scale-based method to predict bone strength shown in terms of R^2 values of linear correlation between yield

stress and each of TW_{TS} (a), SCR_{TS} (b), and $BMDl_{TS}$. (d,e) Same as (a,b) but for the VTA method [116] 74

27. Illustration of the t-scale plate-width measure for in vivo imaging on an age-BMI-similar female and male pair: (a) female healthy volunteer and (b) male healthy volunteer 76

28. Same as Figure 27, but comparison between an age-sex-BMI-similar SSRI patient and a non-athlete: (a) health volunteer and (b) SSRI patient. 77

29. An illustration of the relationship between prior class distributions and class uncertainty for a two class problem. It should be noted that class uncertainty is maximum around the threshold selected under minimum-error criterion. Image points with intensity values of either t_1 or t_2 are classified as object points. However, the class-uncertainty associated with points having intensity t_1 is significantly higher than that for points with intensity t_2 82

30. An illustration of the relationship between class uncertainty and tissue interfaces under different conditions of thresholding. (a) An image slice from a CT data of a patient's lower abdomen. (b) Image intensity histogram for (a) with three thresholds marked as th_1, th_2 and th_3. The first two thresholds are manually selected to segment proper tissue regions while the third one is intentionally picked as a bad threshold. (c,d) Thresholded tissue regions and class uncertainty image for the threshold th_1. (e,f), (g,h) Same as (c,d) but for thresholds th_2 and th_3, respectively. Note that class-uncertainty images in (d) and (f) depict respective tissue boundaries while the same in (h) fails to indicate any tissue interface and spills out into the entire soft tissue region 83

31. An illustration of intrinsic basins on an energy line $E_{\sigma 1}$. Different colors are used to indicate different intrinsic basins; however, one intrinsic basin may include multiple colors. For example, the intrinsic basin marked in blue on the right side includes all the regions marked in yellow and cyan along with the two small regions marked in red. All invalid valley points are marked red and others represent valid valley points 88

32. An illustration of different types of optimum locations on an energy surface/function. The energy function is rendered using a 3D MATLAB display function, with color indicating the energy value (red: high, blue: low). Here, valley lines are shown in red; Type I (pit) and II optimum locations on the energy surface are denoted by hollow black and hollow red circles, respectively. 89

33. A graphical illustration of the error measure between a selected threshold s and the true threshold t. Essentially, it computes the pixel/voxel density weighted distance (the area of the grey region) between the two thresholds and normalized by image size, i.e., the total area under the histogram. 92

34. Results of application of different thresholding methods on a CT image slice of lower abdomen. (a) Original CT image slice. (b) Optimum thresholds (red lines). (c) The energy surface with valley lines (red) and optimum threshold and gradient parameters (hollow circles). (d) Thresholded regions in different colors as applied to the original image. (e) Same as (d), but applied to a smoothed image. (f) Object class uncertainty maps at different optimum thresholds. Note that the class uncertainty image highlights different tissue interfaces at different optimum thresholds. (g,h,i) Same as (b,d,e), respectively, but for Otsu's method. (j,k,l) Results of thresholding as obtained by the MSII, ME, MHUE algorithms, respectively 95

35. Results of quantitative analyses of image threshold errors by different methods. For each ankle CT image, indicated by a number between one and twelve on the horizontal axis, height of the bar indicates the percentage image threshold error. The line one each bar denotes the standard deviation (in percentage scale) of threshold errors for different interfaces of an image 96

36. Results of reproducibility analysis and intra-class coefficient (ICC) of threshold values in repeat CT scans. (a) ICC for threshold values of different tissue interfaces of four specimens in three repeat scans using the new method. (b) Same as (a) but for Otsu's method. (c,d) Same as (a,b) but for ICC value of thresholds for matching interfaces in different specimens using the first CT scan. 98

CHAPTER 1. INTRODUCTION

Trabecular bone (TB) is a network of interconnected plates and rods that dominates near the ends of long bones and in the axial skeletal bones, e.g., proximal femur and vertebrae. In order to adapt to stresses in our daily life, TB constantly remodels through a dynamic bio-equilibrium of bone formation (osteoblast) and resorption (osteoclast) (Wolff's Law [1]). In osteoporosis, this dynamic biological equilibrium between bone formation and resorption is perturbed where the bone formation lags behind the resorption, leading to net bone loss and structural deterioration. It leads to increased skeletal fragility, enhancing the risk of low-trauma osteoporotic fracture associated with substantial morbidity, mortality, and financial costs [2]. Approximately, 30% of postmenopausal white women in the United States suffer from osteoporosis [3] and the prevalence in Europe and Asia is similar. In the United States alone, 10 million individuals are estimated to have osteoporosis and almost 34 million more have low bone mass, a condition called "osteopenia," placing the latter at high risk of developing osteoporosis.

Clinically, osteoporosis is defined by low bone mineral density (BMD) measured using dual-energy X-ray absorptiometry (DXA). However, BMD only explains about 60% to 70% of the variance in bone strength [4, 5], while the remaining variance is due to the cumulative and synergistic effects of various factors, including bone macro- and micro-architecture, tissue composition, and micro-damage [6, 7]. Most osteoporotic fractures occur at sites rich in TB (vertebrae, radius, proximal femur), which leads to the notion of TB bone quality, chief among which is architecture as a determinant of TB strength. Several clinical studies [8-12] have observed results supporting the role of TB architectural quality in determining skeletal strength. Recent advances in imaging technologies including magnetic resonance imaging (MRI) [4, 13-18], high resolution peripheral quantitative computed topography (HR-pQCT) [19-21], and multi-row detector computed tomography (MD-CT) [22-29] offer opportunities to segment TB

networks *in vivo* at peripheral sites. However, *in vivo* TB imaging is hampered by the limited signal-to-noise ratio (SNR) that precludes voxel sizes much smaller than trabecular thickness (100-150μm); therefore, resulting images are inherently fuzzy. Thus, most quantitative approaches designed for TB micro-architectural analysis using histologic [30] or micro-CT (μ-CT) imaging [31, 32] techniques fail in the presence of partial volume averaging common at the limited resolution regime achievable under *in vivo* conditions. These challenges and necessities open an avenue for research programs leading to new solutions for quantitative assessment of the quality of complex quasi-random TB micro-architecture where individual trabeculae may be segmented only with significant partial voluming. Although several novel research efforts have been reported in the literature, a gold standard solution with consensus has yet to emerge and there are significant opportunities to advance quantitative TB micro-architectural analytic techniques available in literature. This overall aim of the research designed in the current PhD thesis is to design, develop and evaluate new quantitative techniques for characterization of the integrity of human TB micro-architectural quality at *in vivo* imaging resolution as described in the following chapter.

1.1 Specific Aims

It has been repeatedly demonstrated that the TB network consists of individual trabecular bone plates and rods and their balance plays an important role in determining the integrity and strength of a TB network [17, 33-35]. Saha *et al.* [36] introduced the notion of characterizing the plate and rod geometry of individual trabeculae using digital topology [37, 38], but a major limitation of the method is that resulting classifications are inherently discrete, failing to distinguish between narrow and wide plates. The balance between plates and rods changes gradually during bone formation at younger ages [39], as well as during bone loss [11] or anti-resorptive treatment [40], and, therefore, demands classification of TB geometry/topology on the continuum between a perfect plate and a

perfect rod. One of the aims of the current research design is to develop a computation solution to quantitatively characterize the topology of individual trabeculae on the continuum between a perfect plate and perfect rod at *in vivo* imaging resolution. Later, Saha *et al.* developed a volumetric topological analysis algorithm (VTA) [41] characterizing the topology of individual trabeculae on the continuum between a perfect plate and a perfect rod. Although VTA provides an effective measure of TB micro-architecture from *in vivo* image, its premise is built on digital topology and path propagation approaches making it more suscceeptible to digitization errors and cumulative errors incurred during path propagation. Also, VTA ignores some important information related to structural orientation and anisotropy.

TB is a highly anisotropic structure, so along with the topology properties, researchers also use the orientation property of TB network to determine its quality. According to the study of Oden *et al*. [42], mean intercept length along the specimen's primary axis is strongly associated with failure stress ($r^2 = 0.85, p < 0.001$) and concluded that orientation is a strong determinant of trabecular strength. Siffert *et al*. [43] reported that incorporation of architectural measures increases predictability of bone mass for observed bone strength from 65% to 94%. Odgaard *et al*. [44] provided quantitative evidence of Wolff's law by showing that stress and fabric tensors coincide. Evidence exists that during aging and osteoporosis structural anisotropy increases [39]. Thus, the measurement about the trabecular bone orientation will be a meaningful indication for TB structure strength. The current thesis will develop a new method for characterization of TB orientation properties using a direct orientation measure of individual trabeculae.

Besides topology and orientation, TB thickness and marrow spacing play an important role in TB quality analysis. The TB thickness property represents the length of the shortest path through a bone point within the TB structure; thus the TB thickness is directly related to the bone mass and its strength. Just as the opposite of TB thickness,

marrow spacing measures of the size of space between the TB networks. Specifically, stronger TB will be characterized with smaller marrow spacing and larger TB thickness. One of the aims of this PhD thesis is to develop new methods to accurately measure TB thickness and spacing at the level of individual trabeculae.

Recently, Saha *et al.* [45, 46] conceived a local 3D morphometric index called tensor scale (t-scale) – a local morphometric scale using an ellipsoidal model that yields a unified representation of local structure size, orientation, and anisotropy. The fundamental principle of t-scale in 3D is to represent a local structure by fitting a largest possible ellipsoid in the homogeneous region. The unique property of t-scale is that the ellipsoid's shape, orientation and size simultaneously determine the topology (plates versus rods), orientation, thickness and marrow spacing of trabeculae. The overall aim of this Ph.D. thesis is to ***design, develop and evaluate new 3D image processing techniques to quantitatively characterize the quality of TB micro-architecture in terms of topology, orientation, thickness and marrow spacing, and to move the new technologies from investigational research into the clinical arena.*** This overall aim will be accomplished by undertaking the following specific aims:

Aim 1 Development of a star-line-based algorithm for an accurate and robust measure of TB thickness and marrow spacing at *in vivo* resolution.

Aim 2 Development of algorithms for t-scale-based quantitative analyses of TB micro-architecture at *in vivo* resolution.

- **Aim 2a** Development of algorithms for efficient computation of t-scale for *in vivo* TB images.
- **Aim 2b** Development of algorithms for computing different t-scale-based TB micro-architectural measures, including (a) structural plate-width and (b) structural orientation.

Aim 3 Evaluation of the accuracy of the different TB architectural measures using computer-generated phantom images with known structural thickness or width.

Aim 4 Evaluation of the robustness of the different TB architectural measures in terms of stability across a wide range of resolutions, repeat scan reproducibility under *in vivo* conditions, and correlation between the measures computed at *ex vivo* (μ-CT) and *in vivo* (MD-CT) resolutions.

Aim 5 Evaluation of the sensitivities of the different TB architectural measures by their abilities in predicting bone strength of cadaveric specimens.

Aim 6 Examination of the application of the new algorithms detecting the effects of bone loss and anti-resorptive treatment with existing *in vivo* MD-CT data and comparison of the results with MD-CT-based BMD measures.

The above aims will offer solutions for characterization of the integrity of TB micro-architecture in terms of topology, orientation, thickness and marrow spacing that is accurate, reproducible, and sensitive. The new methods will facilitate detection of TB alteration among different study groups with known differences bone metabolism. These claims will be evaluated by examining the following hypotheses:

Hypothesis 1: The TB architectural measures obtained using the above methods from 3D images are more robust and have superior repeat scan reproducibility than conventional morphometric and topological parameters.

Hypothesis 2: The TB architectural measures obtained using the above methods from 3D images are more sensitive in detecting early remodeling changes reflecting either disease progression or regression in response to therapy than conventional morphometric and topological parameters.

Hypothesis 3: The TB architectural measures from the above methods provide better discrimination among different TB strength than different BMD measures.

The aims have been accomplished and the results are published in [47, 48]. The Ph.D. research project involves research works related to the following major areas – (1) trabecular bone properties, (2) TB thickness and marrow spacing computation, (3) t-scale theory, (4) image thresholding, (5) skeletonization and feature propagation. The overall

methods, strategy and experimental plans will be introduced in the following subchapters. A brief literature survey on each of the above research topics is presented, with emphasis on the contribution from the current research study.

1.2 Trabecular Bone, Osteoporosis and Diagnosis

Trabecular bone is a network of interconnected plates and rods fused to and encased by a thin cortex. It is predominant in the axial skeleton and near the joints of long bones. In the human skeleton, trabeculae are typically 100-150 μm thick, whereas the thickness of the cortex varies between 1 and 5 mm. In the adult skeleton bone constantly remodels through complex interplay between bone formation by osteoblasts and bone resorption by osteoclasts. In osteoporosis, this dynamic equilibrium between bone formation and resorption is perturbed, leading to bone loss and structural deterioration, both of which increase fracture risk. Most osteoporotic fractures occur at skeletal sites rich in TB, which remodels up to an order of magnitude faster than cortical bone. The majority of osteoporotic fractures occur in older women, due to the increased remodeling rate associated with a net negative bone balance after menopause [49]. Approximately 30% of post-menopausal white women in the United States have osteoporosis [50] and the prevalence in Europe and Asia is similar.

1.2.1 Bone Density and Trabecular Architecture

The clinical definition of osteoporosis refers to a condition in which bone mineral density (BMD) is at least 2.5 standard deviations (also referred to as “T-score”) below the mean of the young adult population [51]. BMD derived from quantitative CT or dual-energy X-ray absorptiometry (DXA) is an apparent density measured as the amount of mineral per unit volume (for CT) or area of tissue (for DXA), expressed in g/cm^3 or g/cm^2, respectively. The latter measure has further limitations as it represents a density obtained from projection imaging and thus depends on bone size. The BMD paradigm rests on the notion that ultimate strength scales as a power of BMD (with an exponent of

approximately 2[52]) and further, that the intrinsic material strength remains invariant (i.e., that "normal" and osteoporotic bone are no different in their ultra-structural and chemical make-up). It may be reasonable to state that, as long as both structure and intrinsic material properties remain unaltered during bone loss, BMD is an accurate predictor of the bone's mechanical competence. In the laboratory, it has been shown that BMD explains, on the average, about 60% of bone strength as estimated from a meta-analysis of 38 studies investigating some measure of bone strength [4]. The data demonstrate the dramatically reduced strength resulting from loss of entire TB elements as opposed to homogeneous thinning for the same amount of bone loss. These findings emphasize the importance of architecture, in particular the maintenance of structural connectivity, which can be assessed by evaluating the topological changes that accompany bone loss and treatment [53]. The lack of changes in BMD values in response to treatment with antiresorptive therapy lends further support to the role of architecture in conferring fracture resistance. The Multiple Outcomes of Raloxifene Evaluation Trial [54] involving 7,700 women with osteoporosis showed that only 4% of the reduction in fracture incidence could be explained by changes in BMD. In a trial on the efficacy of nasal-spray salmon calcitonin, Chestnut *et al*. [55] found that treatment decreased fracture risk by 36% while BMD increased by a mere 1.2%. The discrepancy between the two measures was conjectured to be the consequence of antiresorptive therapy induced reduction of bone turnover [56] because rapid bone remodeling is known to result in a less connected and thus mechanically compromised network [57]. Siffert *et al*. [43] reported that incorporation of architectural measures increases predictability of bone mass for observed bone strength to 94% from 65%. Odgaard *et al*. [44] provided quantitative evidence of Wolff's law by showing that stress and fabric tensors coincide. Evidence exists that during aging and osteoporosis structural anisotropy increases [39]. In the vertebrae, for example, preferential loss of transverse trabeculae in women renders the bone more anisotropic and more prone to failure by buckling [58]. Certain pathologic

processes such as the action of supraphysiologic levels of corticosteroid, primarily lead to homogeneous thinning and during the early phase of atrophy would not significantly reduce connectivity [59]. Hwang *et al*. [60] found that BV/TV (BV/TV=sum of the bone volume fraction of all voxels divided by the total number of voxels) accounts for 57% of the variations of Young's modulus, whereas an additional 34% could be explained by incorporation of architectural parameters.

These findings are not surprising in that they merely reflect that bone cannot defy general engineering principles that dictate that the arrangement and shape of the structural elements determine the critical load a structure can sustain. The dichotomies between density and strength have spurred the search for other predictors of bone strength and fracture risk, notably what has been loosely denoted bone quality, a term collectively referring to various parameters, including structure, matrix and mineral properties.

1.2.2 Recent Study of Osteoporosis Imaging

The conventional tool for assessing TB structure is histomorphometry from bone biopsies (see, for example, [61]). The method yields two-dimensional representations of the TB architecture from which the third dimension is obtained in an inferential manner using the mathematical tools of stereology [62, 63]. Since TB networks are inherently three-dimensional, 2-D histomorphometric approaches have, in recent years, been superseded by direct 3-D analysis of biopsy specimens imaged by μ-CT (see, for example, [63] and references cited). Commercial desktop μ-CT instruments, available from several manufacturers, are now indispensable research tools. They have maximum resolution on the order of 8 μm isotropic, therefore providing detailed insight into TB micro-architecture. Although the method is nondestructive, it is invasive, since bone biopsies are required, but rarely indicated clinically and not suited for following patients longitudinally to evaluate treatment response. More recently, the μ-CT cone-beam scanning technology has been incorporated into dedicated CT systems designed for high-

resolution imaging of TB at the distal extremities, i.e., the distal radius and tibia (see, for example, [64, 65]).

In 2012, Link [66] did an extensive survey of current state-of-the-art imaging techniques in the diagnosis of osteoporosis. Compared to traditional BMD measurements, which are standardized and part of normal clinical routine, techniques to measure bone quality *in vivo* are more challenging and are research topics, such as the previously mentioned magnetic resonance (MR) imaging, multi-row detector CT (MD-CT), quantitative ultrasound (US) and high-resolution peripheral quantitative (HR-pQ) CT.

HR-pQCT [19, 67-70] provides higher signal to noise ratio (SNR) and spatial resolution compared to MRI and MD-CT. Also, the effective radiation dose is substantially lower compared to whole-body MD-CT and the dose primarily does not involve critical, radiosensitive organs. The scan time is approximately 3 minutes for each scan of the tibia or femur. One other advantage of the system is that it allows acquisition of BMD, trabecular and cortical bone architecture at the same time. However, this technique is limited to peripheral skeletal sites, and therefore can provide no direct insight into bone quality in the lumber spine or proximal femur-common sites for osteoporotic fragility fracture [70]. Moreover, it has a limited life span and motion artifacts sometimes limit morphologic analysis of the bone architecture.

MD-CT is standard in clinical practice, with superior spatial resolution compared with previous spiral CT scanners. However, during the imaging of trabecular bone structure, the spatial resolution is still limited (0.25-0.3 mm^3 [71] compared to 0.05-0.2 mm in diameter for individual trabeculae) leading to substantial partial voluming effects. Despite that fact, it is been shown that MD-CT correlates with those determined on contact radiographs from histologic bone sections and micro-CT [72, 73]. An advantage of MD-CT over HR-pQCT is access to central regions of the skeleton such as the spine and proximal femur, sites at risk for fragility fractures; however at the same time, it requires high radiation exposure [74]. Clinical studies have demonstrated that MD-CT-

derived structure measures at the proximal femur and lumbar spine improve differentiation between osteoporotic patients with proximal femur fractures and healthy controls [75], as well as individuals with and those without osteoporotic spine fractures [76]. In addition, the technique was shown to be well-suited for monitoring teriparatide-associated changes of vertebral microstructure [74]. Recently, Keaveny *et al.* [77-79] used finite element analysis to study vertebral body strength and therapy-related changes in multidetector CT data sets of the spine and proximal femur; the results of this work suggested improved monitoring of treatment effects compared with DXA and greater sensitivity in fracture risk assessment.

Advances in MR imaging software and hardware, including 3-T imaging and improved coil design, have allowed substantially enhanced trabecular bone architecture imaging. A number of clinical studies were performed that demonstrated that MR imaging–derived structure measures provided additional information to BMD in differentiating individuals with from those without fragility fractures [80-82]. In addition to postmenopausal women, trabecular bone was studied with MR imaging in hypogonadal men, patients with cardiac and renal transplants, and patients with renal osteodystrophy [33, 83, 84].

A recent meta-analysis on osteoporosis screening found that both DXA and calcaneal quantitative ultrasound (US) could be used to predict fractures in an older patient population but that the correlation between the two techniques was low [85]. Quantitative US is a low-cost technique performed with dedicated scanners acquiring data mostly at the calcaneus. The strong power of quantitative US to predict osteoporotic fractures has suggested that the technique could be well-suited to assess bone quality [86]. However, there has been a proliferation of quantitative US devices that are technologically diverse, measuring and reporting variable bone parameters in different ways [87]. While quantitative US has been shown to differentiate individuals with from

those without fragility fractures [88, 89] and to predict fracture risk [90], it has not been established to diagnose osteoporosis such as DXA has [87].

1.2.3 Image-based Approaches to TB Architecture

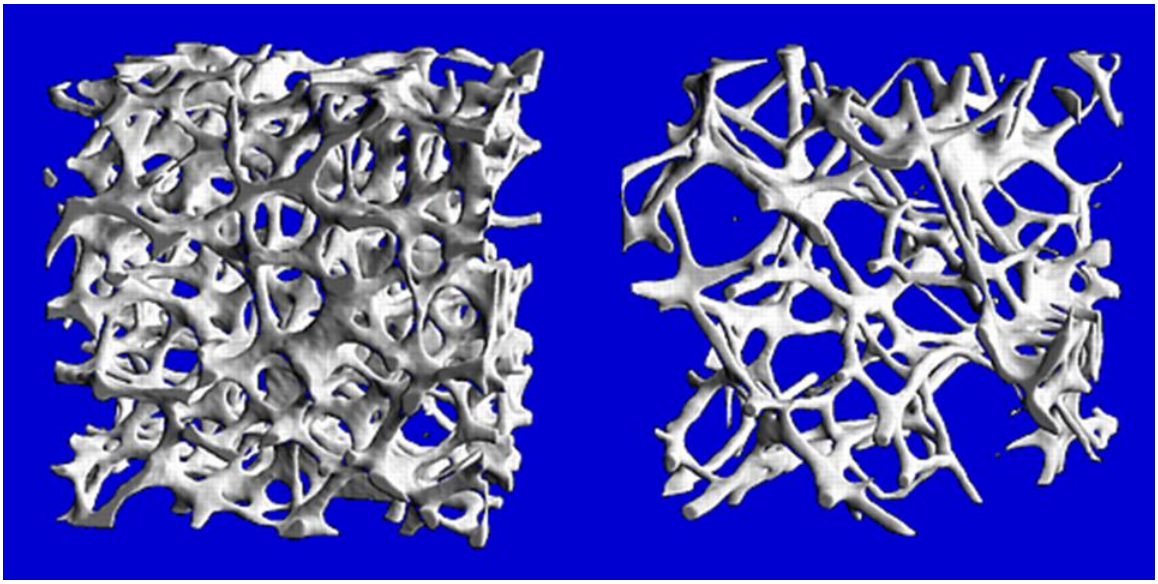

Figure 1 3D rendered of a trabecular bone sample. The bone sample displayed on the right predominantly contains rod-like trabeculae while the left one on the right mostly consists of plates.

Topology and geometry: The striking difference in topological make-up of bone from the same anatomic site is illustrated in Figure 1 [31] for predominantly plate- and rod-like trabeculae in the calcaneus. Various topological and geometric properties of TB networks for characterizing TB architecture have been reported in the literature [13-15, 31, 38, 60, 63, 91-106]. Parfitt [91] conceived a parallel interconnected plate model of TB yielding bone area fraction, TB volume fraction, TB spacing and TB number from 2D histomorphometric sections. This approach has also been adopted for the analysis of MR images [13, 107]. Vesterby [94, 95] conceived a new stereologic parameter, called star volume, which is the average volume of an object region that can be seen from a point

inside that region un-obscured in all directions. This approach provides an effective measure of marrow space geometry, which increases as a result of osteoclastic resorption. Hahn *et al*. [97] introduced the "Trabecular Bone Pattern factor" (TBPf) which captures TB connectivity in terms of convexity property of TB surface defined as ratio of the differences in perimeter and area under dilation. Hildebrand *et al*. [31, 100] developed a 3D structure model index (SMI), a function of global plate-to-rod ratio, based on the observation that the rate of change of volume with thickness for a plate is different from that for a rod. Majumdar *et al*. [14, 15] have adopted apparent TB number (app. TB.N), apparent TB thickness (app TB.Th), apparent TB spacing (app TB.Sp) and fractal dimension to quantify TB structural quality. Several architectural parameters of TB networks were introduced utilizing autocorrelation techniques [60, 102] by exploiting the quasi-regularity of TB networks. Stampa *et al*. [104] introduced two new measures, namely, relative plate and relative rod volume (rPV and rRV, respectively) using TB voxel counts in 3×3 planes around each TB voxel. Some investigators [92, 96] have analyzed the nodes and free ends of TB and others [99] have used ridge number density measuring the bone skeletal length. Feldkamp *et al*. [93] first showed that the makeup of TB networks can be expressed in terms of topological entities such as the 3D Euler number. Gordon *et al*. [98] introduced a connectivity index using the numbers of nodes, free ends, isolated points, and the network length. By means of a skeleton line graph analysis method of high-resolution MR images, Pothuaud *et al*. [63] explored whether the network topology in osteoporosis was different from that in osteoarthritis. In a later work [103], using a multivariate model, the same group of researchers studied the strengths of topological parameters and bone volume fraction to predict TB's mechanical behavior. Although quantification of network topology on the basis of the Euler-Poincaré characteristic can provide useful insight, the method is limited in its ability to quantify the topological implications of bone resorption. The potential fallacy of the Euler number is a measure of bone resorption becomes evident when we consider the consequences of

non-homogeneous thinning. Whereas perforation of a surface increases the number of loops, disconnection of a rod-like element removes a loop. Thus, although both processes affect the topology of the structure, they do so in opposite ways. The result could thus have very little or no effect on the Euler number.

Structural anisotropy: TB remodels in response to the stresses to which it is subjected [1] in such a manner that the trabeculae become aligned with the major stress lines, thus leading to a highly anisotropic network. Structural anisotropy of TB was first quantified by Whitehouse who showed in sections of TB that by plotting the mean intercept length (MIL) in the marrow spaces in a polar diagram, an ellipse is traced [108]. In a direct extension of this approach, Harrigan [109] proposed a general method based on analyzing the three faces of a cubic specimen for three-dimensional mapping of structural anisotropy, yielding the Eigenvalues and Eigenvectors of the mean intercept ellipsoid. Chung *et al*. [107] applied this approach to map the TB fabric tensor of bovine tibia, human vertebrae, and radial bone on the basis of 3D μ-MRI images. Recently, Gomberg *et al*. [110] developed a direct method called digital topological analysis-based orientation (DTAO) analysis to yield regional orientation and anisotropy after identifying the topological type (plates and rods) of each trabecula and observed a clear orientation difference between the medial and lateral sides of axial cross sections in μ-MRI images of the human distal wrist.

TB thickness and spacing: The thickness of TB is an important architectural determinant of bone strength [111]. Corticosteroid exposure, for example, is well known to cause TB thinning [59]. Conversely, treatment with anabolic agents, such as parathyroid hormone, causes TB thickening. The classical approach toward measuring TB thickness is based on histomorphometry of bone biopsies and involves measuring bone perimeter and area [91]. Hildebrand *et al*. [100] introduced a model-independent 3D method to compute TB thickness at any bone location in a binary image as the diameter of the largest inscribed sphere containing that location. Laib *et al*. [99] used the standard

deviation of apparent intra-individual distribution of TB separations as a discriminator of fractures. Gordon *et al*. [98] defined mean hole-area in cross-sectional images of TB by dividing total marrow area by the number of holes. This parameter is essentially a measurement of average marrow-hole size in 2D.

1.3 Digital Topological Analysis

In 1996 Saha and Chaudhuri [37] conceived the theory and algorithms to compute local topological parameters, i.e. the number of objects, tunnels, and cavities, in the $3 \times 3 \times 3$ neighborhood of an object voxel after the hypothetical transformation of the latter to a background voxel. The topological parameters permit unambiguous determination of the local topological classes (surface, curve, and junction) in the skeletonized representation [112] of a structure. This algorithm was subsequently applied to digital images of TB [38, 106]. In this work, DTA was showed on the basis of *in vivo* MRI structure analysis that the etiology of bone loss proceeds via a conversion of TB plates to rods and eventual disconnection of the latter structure elements [101]. Unlike in the approach by Pothuaud *et al*. [63] in which the TB structure is reduced to a line skeleton, Saha *et al*.'s method preserves TB plates by skeletonizing the structure such that plates are reduced to surfaces and rods to curves. Two composite parameters, the surface-to-curve ratio (S/C) and erosion index (EI) were derived from individual topological parameters obtained using digital topological analysis (DTA). EI, for example, was defined as the ratio of the sum of parameters expected to increase upon osteoclastic resorption, divided by the sum of parameters expected to decrease secondary to such processes.

Despite the power of local network topology for characterizing the quality of TB architecture, the method has limitations: (1) binarization: DTA requires binary segmentation into bone and bone marrow voxels introducing significant errors at *in vivo* resolution where most bone voxels are only partially occupied. (2) hard classification: the

method classifies a trabeculae as a plate (S) or a rod (C) and, therefore, is unable to distinguish among trabeculae constituting narrow and wide plates. As a result, the method would be a less effective discriminator at the early stage of conversion of trabeculae from plates to rods – an etiology of osteoporotic bone loss [35, 113]. Moreover, such a classification is highly resolution-dependent. These limitations do not apply only to DTA, but equally to most other methods described above. Moreover, the majority of structure analysis methods are capable of providing only global measures and, therefore, cannot be used to explore the spatial distribution of network architecture.

1.4 TB Thickness and Marrow Spacing Computation

The classical approach of measuring trabecular thickness is based on histomorphometry of transiliac bone biopsies [61]. The emergence of imaging technologies such as micro CT (μ-CT) [114] enables reconstruction of high resolution three-dimensional (3-D) images calling for more elaborate techniques for computing TB thickness. Recently, *in vivo* imaging techniques including magnetic resonance (MR), high resolution peripheral quantitative CT (HR-pQCT), and multi-row detector CT (MD-CT) have become promising modalities for high quality TB imaging at peripheral sites [23, 25, 76] that avoid the problems of invasive bone biopsies. Therefore, an accurate and robust algorithm of computing TB thickness and marrow spacing that is applicable to *in vivo* imaging would be useful as an effective indicator of quantitative bone quality for clinical trials evaluating fracture risks under different clinical conditions.

Several methods for computing TB thickness and marrow spacing have been reported [115-118]. Hildebrand et al. [115] presented a model-independent binary approach involving inscribing spheres into the target TB structure where trabecular thickness at any location is computed as the diameter of the largest inscribed sphere containing that location. A star-volume-based algorithm which calculates the mean volume of all parts of an object that can be seen un-obscured from any point within the

target object, has been developed and used to measure TB marrow spacing in binary images [117, 118]. These approaches are well-suited for high-resolution images that can easily be segmented but it is bound to fail when significant partial voluming is present. Saha et al. [116] overcome this issue of partial voluming at low resolution in TB thickness computation by introducing the use of fuzzy distance transform and a global compensation.

1.5 Tensor Scale

Scale [119-121] may be thought of as the spatial resolution, or more generally, a range of resolutions needed to ensure a sufficient yet compact representation of target information [119]. Scale plays an important role in image processing applications. Witkin [120] and Koenderink [121] mathematically formulated the concept of scale in the form of scale-space theory. Discrete scale-space representations [122] have been used in several imaging applications, including segmentation [123], clustering [124], classification [125], and structural analysis [126]. Although scale-space image representations have provided significant insight, it is not obvious – (1) how to unify the information from images at different scales, and (2) how to identify the optimal scale at each individual image point. A knowledge of "local scale" [127-130] would allow us to spatially tune the neighborhood size in different processes leading to selection of small neighborhoods in regions containing fine detail or near an object boundary, versus large neighborhoods in deep interiors [45]. Also, local scale would be useful in developing an effective space-variant parameter controlling strategies [46].

The notion of local morphometric scale was introduced using a spherical model in [45, 46] and was applied to different image processing algorithms; see [131] for a survey on local scale. Although the preliminary results have demonstrated effectiveness of this notion of local scale in different image processing applications, a major limitation of the spherical model is that it ignores orientation and anisotropy of local structures. Recently,

Saha *et al.* [131] proposed a new local morphometric scale, called “tensor scale” (t-scale) using an ellipsoidal model which gives a unified local parametric representation of structure size, orientation, and anisotropy. T-scale is a valuable feature associated with every image point and is potentially useful in several image processing and computer vision applications, especially medical imaging applications where local structural and scale information could play important roles. A few works have been reported on representing local orientation using gradient structure tensor [132] and its applications have been demonstrated in image filtering [132] and adaptive image morphological analysis [133]. Although structure tensor is a useful concept and efficiently provides orientation information near edges, it primarily captures information derived from local gradient fields and may not directly relate to local structure geometry that yields shape and size or thickness information. For example, in a homogeneous region, structure tensor may not carry meaningful information related to local structure. Here, we formulate t-scale from a geometric perspective where, at each image point, the tensor captures information related to local structure geometry.

Effectiveness of t-scale in image segmentation [110], registration [134], filtering [131] and also in quantifying local morphometry in complex quasi-random networks of trabecular bone [36, 135] have been studied. Andalo [136, 137] presented an efficient computational solution for t-scale and demonstrated its usefulness in detecting salient points on a given contour. As mentioned in previous sections, in TB quality analysis, t-scale computation is able to provide information on TB plate and rod classification, orientation analysis, surface curve ratio (SCR), and TB thickness and marrow spacing. All those are closely connected to TB quality and will be discussed in detail in later chapters.

1.6 TB Segmentation

Automatic selection of a robust and accurate threshold parameter has remained a challenge in image segmentation. Over the past five decades, many automatic threshold selection methods have been reported in the literature [138-157]. In the late 80's, Sahoo *et al.* [138] published a survey of optimum thresholding methods while Lee *et al.* [139] reported results of a comparative study of several thresholding methods. Glasbey [140] reported results of another comparative study involving eleven histogram-based thresholding algorithms. A relatively recent survey of thresholding algorithms for change detection in a surveillance environment has been presented by Rosin and Ioannidis [158]. Among early work on automatic thresholding, Prewitt and Mendelson [141] suggested using valleys in a histogram, while Doyle [142] advocated the choice of median. Otsu [143] developed a thresholding method maximizing between-class variance. Tsai [146] proposed a choice of threshold at which resulting binary images have the identical first three moments where the *i*-th moment is defined by the sum of pixel intensity values raised to the *i*-th power. Later works on thresholding methods have utilized entropy of original and thresholded images to construct an optimization criterion. For example, Pun [147] maximized the upper bound of posterior entropy of histogram. Wong and Sahoo's method [148] selects the optimum threshold that maximizes posterior entropy subjected to certain inequality constraints characterizing the uniformity and shape of segmented regions. Pal and Pal [149] utilized the joint probability distribution of neighboring pixels which they further modified [150] using a new definition of entropy. Kapur *et al.* [151] proposed a thresholding method by maximizing the sum of entropies of segmented regions and a similar method was reported by Abutaleb [152] that maximizes 2D entropy. The method by Brink [153] maximizes the sum of entropies computed from two autocorrelation functions of thresholded image histograms. Li and Lee's method [154] minimizes relative cross entropy or Kullback-Leibler distance between original and thresholded images. Kitler and Illingworth [155] developed a thresholding method by

minimizing segmentation errors defined from an information-theoretic perspective, while Dunn *et al.* [156] used a uniform error criterion. Leung and Lam [157] developed a method that maximizes segmented image information derived using an information-theoretic approach and demonstrated that their method is better than the methods based on minimum and uniform errors [155, 156]. Sahoo *et al.* [159] developed a thresholding method using Renyi's entropy that includes both maximum entropy as well as entropic correction methods. Zenzo *et al.* [160] introduced the notion of "fuzzy entropy" and demonstrated its application to image thresholding using a functional cost minimization approach. Oh and Lindquist [161] developed an indicator kriging based two-class segmentation algorithm for two- and three-dimensional images characterized by a stationary and isotropic two-point covariance function. Recently, several image thresholding methods [162, 163] have been reported using Tsallis entropy [164] that generalizes the Boltzmann-Gibbs-Shannon statistics describing thermo-statistical properties of non-extensive systems. Tizhoosh [165] developed an image thresholding algorithm using type II fuzzy subsets where the range of membership function is the power of [0,1] interval. Bazi *et al.* [166] developed a two-class image thresholding method using expectation-maximization under the assumption of a generalized Gaussian distribution for each class. Image thresholding algorithms have also been studied in the context of document and handwritten image processing [167-172].

1.7 Skeletonization and Back Propagation

Since t-scale is a local property, the measures at an individual voxel location can be directly computed from its local t-scale. However, it can be shown that these measures suffer from edge artifacts when the target voxel is far from the skeleton due to the failure of covering the entire geometry of the local structure within its t-scale. In order to overcome this problem, skeletonization is done on TB structure to obtain the center line, then the measures are evaluated at those center points to avoid the edge artifacts, and

finally, the measures are back-propagated to all TB voxels. Specifically, a surface skeletonization is computed using the algorithm by Saha *et al.* [37] and the feauture propagation is accomplished using the classical algorithm introduced in [41].

The skeletonization process is done in two steps: primary and secondary skeletonization. Primary skeletonization iteratively erodes bone voxels from the current outer layer of a TB object while preserving its topology and so-called "shape." In order to preserve TB object topology, only (26, 6)-simple voxels [173, 174] are considered for erosion. Both surface- and arc-like shape voxels [112] are preserved during the erosion process. The output of primary skeletonization may contain two-voxel thick surfaces and curves. Extra thick voxels [112] are removed using an extra iteration referred to as secondary skeletonization. For noise removal, the basic idea here is to distinguish skeletal branches contributed by true geometric features in the original object from those originated by noisy bumps or dents, often, common in digital images.

After the t-scale-based measures are evaluated at the skeleton points, the last step would be propagating the measures from skeleton points to the entire TB volume for statistical analysis. Bonnassie *et al*. [175] proposed a feature propagation method from skeletal voxels to entire volume by copying feature values from a skeletal voxel p to all voxels within the maximal ball centered at p. However, as mentioned by the authors, the method suffers from the fact that final results depend on the order in which skeletal voxels are processed. The solution we applied is the classic propagation algorithm: 1) initiate the measures at each voxel p on the skeletal scale S of O and 2) at a non-skeletal voxel q, inherit the measures from its nearest skeletal voxel. The algorithms will be discussed in detail in the following chapters.

1.8 Experimental Plan

The experiments were designed following the guidelines of Aims 3-6. Specifically, we performed the following experiments – (1) Accuracy of different TB

structural measure: thickness and marrow spacing, as well as the t-scale-based TB characterization measures, (2) Robustness and repeat scan reproducibility of TB structural, (3) Correlation between the TB structural measures computed at *ex vivo* (μ-CT) and *in vivo* (MD-CT) resolutions using human ankle specimens, (4) Sensitivity of the TB structural measures to predict TB strength of cadaveric specimens, (5) Robustness of the TB structural measures on *in vivo* MRI images and (6) Application of the TB structural measures on *in vivo* MD-CT data. These experiments are further elaborated on here:

Accuracy of TB thickness and marrow spacing, as well as the t-scale-based measures: computer-generated phantom images. For TB thickness and marrow spacing measures, three-dimensional (3-D) binary phantoms along with ground true regional thickness distribution at high resolution were generated. Then the test phantom images were generated by down-sampling binary phantoms at $3 \times 3 \times 3$, $4 \times 4 \times 4$, and $5 \times 5 \times 5$ and by adding noise at signal-to-noise ratios (SNR) of 6, 12 and 24. Error was calculated at individual voxel location in a phantom as the absolute difference between the true and computed thickness values. For t-scale-based measures, 3-D fuzzy phantoms with different widths at 50 μm resolution were generated. Then the test phantom images were generated by down-sampling binary phantoms at 150 μm resolution and by adding noise at signal-to-noise ratios (SNR) of 12. Mean plate width was calculated over the whole phantom region, and error was computed from the difference between the true width and computed values.

Robustness of TB thickness and marrow spacing, as well as the t-scale-based measures: for thickness and marrow spacing measures, three different experiments were conducted to assess the robustness. The first experiment was designed to examine robustness of the method under errors in skeletal location. The second experiment quantitatively examined the stability of the measures at different down-sampled μ-CT TB images. And the third experiment further examined the performance of the measures

under different resolutions, with the correlation computed from *ex vivo* μ-CT and *in vivo* MD-CT imaging. For the t-scale-based measures, only the second and the third experiments were done, because the algorithm is highly sensitive to the location of candidate points.

Reproducibility of TB thickness and marrow spacing, as well as the t-scale-based measures: three repeat MD-CT scans of fifteen cadaveric ankle specimens were used to examine reproducibility. For quantitative analyses, ten spherical VOIs of the same radius were randomly selected in the first MD-CT scan of each specimen above the position 8 mm proximal to the distal endplate, leading to a total of 150 VOIs. A post-registration algorithm was used to locate the matching VOIs in the second and third repeat scans. It is obvious that the results of reproducibility analysis depend on the scale of VOI, with larger VOIs showing improved reproducibility. The relationships between the TB structural measures' reproducibility and VOI size were examined.

Accuracy of TB thickness and marrow spacing, as well as the t-scale-based measures to predict TB strength: The purpose of this experiment was to compute ability of different TB structural measures in predicting TB biomechanical properties. This goal was achieved by measuring actual bio-mechanical parameters of TB cores and evaluating their correlation with the measures. Cylindrical TB specimens nominally 8 mm in diameter and 20.9±3.3 mm in length were cored from each distal tibia specimen *in situ* along the proximal-distal direction for mechanical testing. The experiments will be performed on a servo-hydraulic material testing machine (MTS 858 Bionix, MTS Systems Corp., Eden Prairie, MN) at the Orthopaedic Biomechanics Laboratory, Department of Orthopaedics and Rehabilitation, University of Iowa, under the supervision of Dr. Heiner, Associate Research Engineer.

T-scale-based measures on *in vivo* MD-CT patient data: All data come from the ongoing Iowa Bone Develop Study (IBDS) let by Dr. Steven M. Levy. Specifically, a total of 60 young adults (age: 18-21 years) were recruited in four different groups of

young adults with anticipated differences in bone mineralization to investigate several questions concerning associations of TB BMD and t-scale-based measures, and differences among study groups. Specifically, Group 1 was healthy young adult, Group 2 was high-impact-sport athletes, Group 3 was cystic fibrosis patients and Group 4 was selective serotonin reuptake inhibitor (SSRI)-treated patients. For all measurements, the difference between healthy young male and female was quantitatively examined. For the TB thickness and marrow spacing measures, the differences between Group 2 and age-, sex- and BMI-matched healthy controls were examined, while for the t-scale-based measures, the different between Group 4 and age-, sex- and BMI-matched healthy controls were examined.

CHAPTER 2. QUANTITATIVE CHARACTERIZATION OF TRABECULAR BONE THICKNESS AND MARROW SPACING

In this chapter, we describe the theory and algorithm of a new thickness computational method that is applicable to a fuzzy digital representation of any object at a relatively low resolution. The membership value at a given image voxel is interpreted as partial occupancy of the target object within the voxel. In other words, the membership value of a fuzzy object is treated as local object density. Although the thickness computation method is primarily designed for fuzzy digital objects at relatively low resolution, its premise is built on objects in the continuous space. In the following, we first establish the definition of "local thickness" in an object in the continuous space, and then we describe the algorithm that provides an effective solution for fuzzy digital objects at low resolution such as *in vivo* condition.

Novel research works as presented in this chapter:

1) Explore the definition of thickness at individual location within an object.
2) Introduction of a new feature propagation algorithm which preserves the properties at skeleton points.
3) Computation of TB thickness and marrow spacing at skeleton points based on the star-line algorithm.

2.1 Definition of Thickness at Individual Location

Let R^3 denote the continuous three-dimensional (3-D) space and let $O \subset R^3$ be an *object* in R^3. A ball $B \subset O$, is a *maximally included ball (MIB) in* O, if there exists no other ball $B' \subset O$ that contains B. Obviously, at a given point $p \in O$, the local thickness should be related to the diameters of the maximally included balls containing the point p [176]. However, the challenge arises from the fact that a point p is contained in multiple MIBs and the basic question is which one should be used to define the thickness at p.

Consider first the axial points of O. A point $a \in O$ is an *axial point* in O if there is a MIB of O that is centered at a. Following the fact that the maximally included ball $B_O(a)$ centered at a given axial point a is unique and it symmetrically defines the extent of a local object on both sides of the local axis, $B_O(a)$ is the natural choice for defining the thickness at a. Therefore, a proper choice of local thickness should satisfy the following property:

Property 1 For any object $O \subset R^3$ and any axial point $a \in O$, the thickness of O at a is the length of the diameter of the unique MIB $B_O(a)$ centered at a.

Additional importance of Property 1 is that it provides the necessary and sufficient condition for reconstruction of an object from its thickness distribution at axial points. Now, let us examine different possible options of defining local thickness at a non-axial point $p \in O$ using the MIBs containing p; let $\mathcal{M}_O(p)$ denote the set of all MIBs in O containing p. Hildebrand and Rüegsegger [176] used the largest ball in $\mathcal{M}_O(p)$ to define the thickness at p, which was further studied by Moreno *et al.* [177]. Another variation of this choice is to select the diameter of the smallest ball in $\mathcal{M}_O(p)$ to define the thickness at p. We will refer to these options as the largest and smallest MIB options. Both of these options fail to satisfy Property 1 as illustrated in Figure 2(a,b). Also, we examine the behavior of these options for an object formed by two overlapping disks of different scales and the results are illustrated in Figure 3(a,b). The largest MIB option shows thickness bias toward the larger disk, while the smallest MIB option picks the same artifact, but in the opposite direction. Thus, both the largest and the smallest MIB options suffer from serious drawbacks. Here, we introduce the idea of selecting the MIBs based on the distance from the center or from the circumference.

Liu *et al.* [178] introduced the idea of selecting the MIB in $\mathcal{M}_O(p)$ whose center is closest to the candidate point p and used its diameter to define the thickness at the given point p. Although the method satisfies Property 1 as illustrated in Figure 2(c), its

performance in the case of two intersecting balls is seriously flawed as shown in Figure 3(c). Here, we propose the following definition of thickness which satisfies Property 1 (see Figure 2(d)) and an unbiased thickness distribution is obtained for two overlapping balls with varying scales (see Figure 3(d)).

Definition 1 For any object $O \subset R^3$ and any point $p \in O$, the thickness of the object O at the point p, denoted as $\tau_O(p)$ is the length of the diameter of the MIB in $\mathcal{M}_O(p)$, whose circumference is farthest from p.

In the rest of this chaper, we will use the above definition of local thickness computation. It can be shown that, for any object $O \subset R^3$ and any point $p \in O$, the MIB in $\mathcal{M}_O(p)$ whose circumference is farthest is unique. Therefore, the above definition produces a unique thickness distribution for any given object. Also, following Property 1, the thickness values $\tau_O(p)$ at axial points may reconstruct the original object O. In the following, we discuss other challenges of computing thickness in a digital fuzzy object at a relatively low resolution regime.

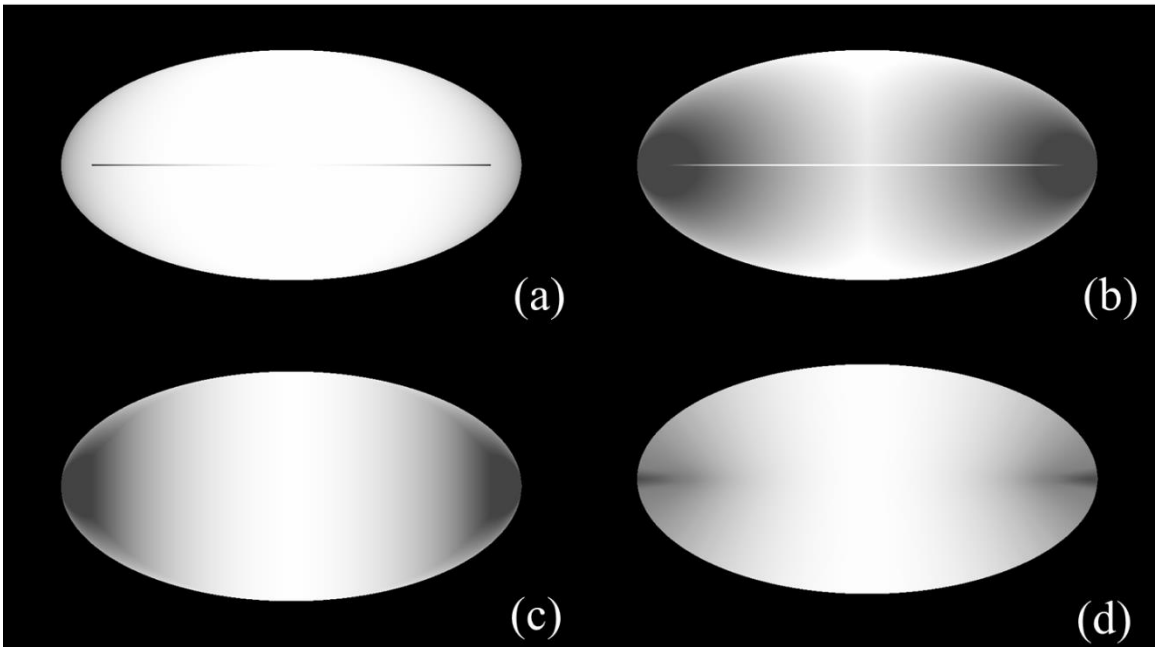

Figure 2 Comparison among different definitions of thickness in terms of satisfying Property 1. (a) Local thickness distribution on an ellipse using the largest MIB option except that the intensity at an axial point a is enforced as the diameter of the MIB centered at that point. (b-d) Same as (a) but for thickness computation using the options of smallest MIB (b), nearest MIB center (c), and farthest MIB circumference (d). Axial lines are partially visible in (a,b) indicating the failure of the corresponding thickness definitions in satisfying Property 1. The axial lines in (c,d) are not visible indicating that both the nearest MIB center and the farthest MIB circumference options satisfy Property 1.

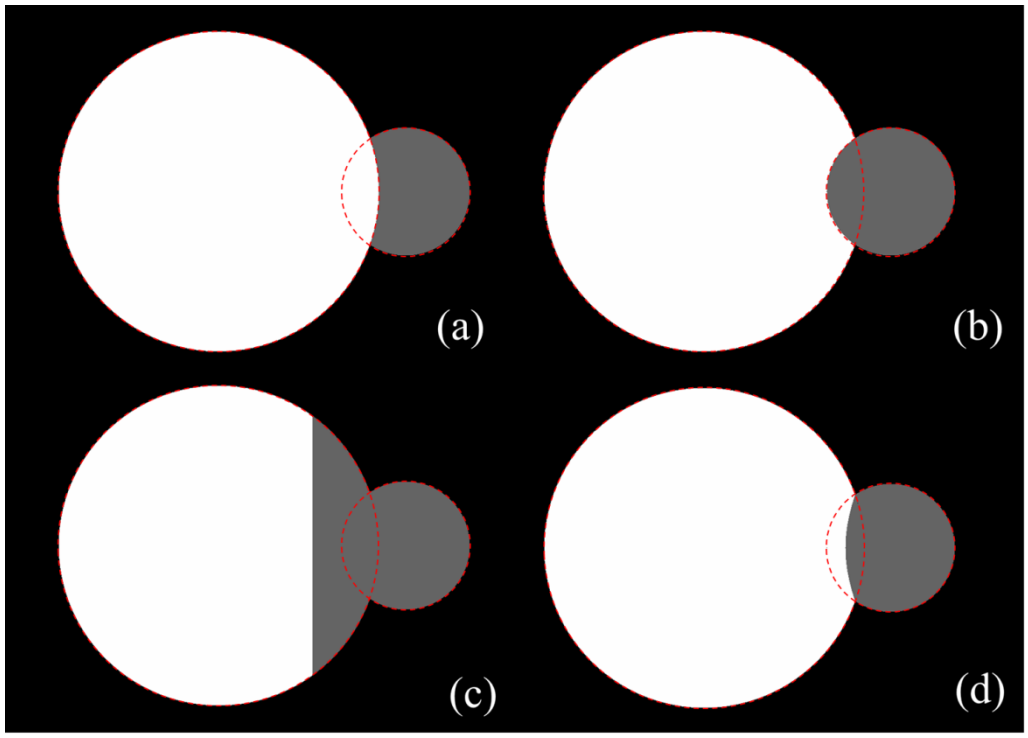

Figure 3 Comparison among different definitions of thickness in terms of their performance for two overlapping disks of different scales. Disk boundaries are shown by dotted lines. (a) Local thickness distribution using the largest MIB option. Here, the larger ball gets higher preference and it enters inside the smaller ball. (b) Same as (a) but for the smallest MIB option; here, the artifact just opposite of that of (a). (c) Same as (a) but using the MIB with the nearest center. The failure of this option is obvious. (d) Same as (a) but using the MIB with the farthest circumference. A major advantage of this option is that it divides the intersecting regions between the two balls eliminating bias artifacts.

2.2 Thickness Computation Algorithm

A thickness computation algorithm in a low resolution fuzzy digital object following Definition 1 needs two major steps – (1) computation of local thickness at axial points and (2) inheritance of local thickness values at non-axial points from axial points.

In conventional algorithms [116, 176], local thickness at axial points is determined by sampling the binary distance transform [179] at axial locations. Such

methods work fine when the image resolution is high and the objects are relatively large, but they may fail when the resolution is close to object thickness. This effect is reduced by using the fuzzy distance transform (FDT) [116] instead of the binary distance transform but FDT does not solve the other fundamental problem related to digitalization of the location of axial points. A thickness computation algorithm based on sampling binary or fuzzy distance transform [180] at axial locations is associated with random negative errors caused by digitalization of axial point locations and magnitudes of the random error are bound by the interval $\left[0, \sqrt{3}\Delta/2\right]$, where Δ is the voxel size. This error was thoroughly discussed by Saha and Wehrli [116] (see Figure 1 in [116]) and a resolution-dependent global compensation factor under several assumptions on structural anisotropy was proposed. The compensation is only applicable on the global measure of average thickness and it seems difficult to correct local thickness measures using Saha and Wehrli's approach [116]. Further, the approach makes several assumptions on structural anisotropy which may not be applicable everywhere. Therefore, it is of paramount interest to develop a method that produces accurate thickness measures at axial points in a fuzzy object at relatively low resolution.

Here, we introduce an intercept-based algorithm of computing thickness at axial points which is robust under small deviations of axial points that frequently happen during digitization of axial points. Let $\mathcal{O} = \{(p, f_{\mathcal{O}}(p)) | p \in Z^3\}$ be a fuzzy object and let $O = \{p | f_{\mathcal{O}}(p) \neq 0\}$ be the support of the fuzzy object. Let us consider a point $p \in O$; an intercept of $\mathcal{O}$ at p along a direction $\langle polar: \theta,\ azimuth: \varphi \rangle$ is the membership-weighted length of the straight line segment $\ell_{\theta,\varphi}(p, O)$ passing through p with the two ends coinciding with the boundary of O. It should be noted that, for a given point $p \in O$, there can be infinitely many intercepts of $\mathcal{O}$ passing through p. Let $\prod_{O}(p)$ denote the set of all-possible intercepts of $\mathcal{O}$ that pass through a point p. The thickness measure $\tau_{\mathcal{O}}(a)$ at an axial point a on an elongated or surface-like region of an object is approximately equal to the length of the shortest intercept of $\mathcal{O}$ passing through a, i.e.,

$$\tau_{\mathcal{O}}(a) = \min_{\ell \in \Pi_{\mathcal{O}}(a)} \pi(\ell).$$

Equation 1

The above equation offers a new algorithm of computing thickness measure at an axial point as the minimum intercept length at that point. In the context of medical imaging, major advantages of this approach of defining local thickness are that – (1) the minimum-intercept length measure is highly robust under small random shifts of axial points, alleviating the resolution-dependent errors caused digitization of axial points [FDT] and by other error incurred during skeletonization and (2) partial voluming effects are efficiently handled during intercept length computation, yielding improved robustness across a wide range of image resolutions covering the range between *in vivo* and *ex-vivo* regimes. These claims are thoroughly examined and the experimental results are presented in Chapter 2.5.

The algorithm for computation of the term $\min_{\ell \in \Pi_{\mathcal{O}}(a)} \pi(\ell)$ at an axial point a may be designed using a star-line tracing approach (Figure 4). Specifically, the star-line-based thickness computation algorithm is performed by locally tracing an object along m pairs of mutually opposite sample lines emanating from a candidate point p (red dot in Figure 4). These sample lines are selected at a pseudo-uniform distribution over the entire 3-D angular space [131]. For all experiments reported in this chapter, we used 123 pairs of sample lines at an approximate angular separation of 12° between every two neighboring sample lines. The extent of the fuzzy object $\mathcal{O}$ along an individual sample line is determined by integrating object membership function $f_{\mathcal{O}}$ at sample points along the specific sample line until the sample line enters into background, i.e., the object membership at the last sample point reaches the value of zero. The local extent of the object along each sample line is recorded (purple dots in Figure 4). For each pair of opposite sample lines, the local intercept length for the target object along the specific direction is determined by adding the object intercept lengths along the two opposite directions. So far, the method provides m possible object intercept lengths along the m

different directions of sample line pairs. Finally, thickness of the target object at the candidate axial point a (red dot in Figure 4) is computed as the shortest (orange line segment in Figure 4) among the m different object intercept lengths along different directions. Once the thickness values are computed at all axial points [181] using the above algorithm, thickness values at non-axial points are inherited from the axial points following Definition 1. Let the thickness at a given point p in a fuzzy object $\mathcal{O}$ be denoted as $\tau_{\mathcal{O}}(p)$. The thickness computation algorithm can be summarized in the following three steps:

Step 1. Computation of the surface skeleton S [112] of the support O of the fuzzy object as the set of axial points.

Step 2. Computation of thickness $\tau_{\mathcal{O}}(a)$ at all axial points $a \in S$ using the star-line-based algorithm described above.

Step 3. Inheritance of thickness $\tau_{\mathcal{O}}(p)$ at all non-skeletal points $p \in O - S$ by inheriting the local TB thickness $TH_B(p)$ from skeletal points following Definition 1.

In the above algorithm, Step 1 is accomplished using the surface skeletonization algorithm by Saha *et al.* [112], while Step 2 is accomplished as described above. In the following, we describe the process for Step 3.

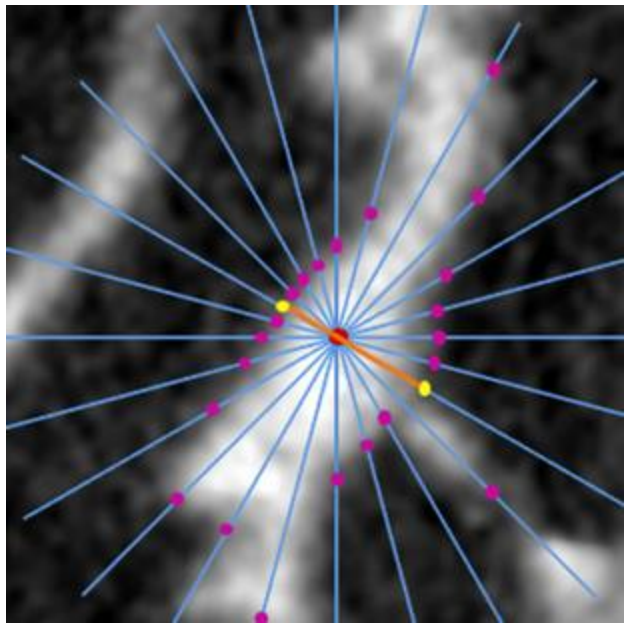

Figure 4 Illustration of star line-based TB thickness in two-dimensions. Candidate point (red), star lines (blue), edge locations (purple) and shortest intercept (orange) in TB thickness computation are shown.

2.3 Improved Feature Propagation Algorithm

Let $a \in O$ be an axial point and let $p \in O$ be a non-axial point. The distance of p from the circumference of the MIB $B_{\mathcal{O}}(p)$ centered at the axial point a is essentially the following measure $\tau_{\mathcal{O}}(a) - \omega_{\mathcal{O}}(a,p)$, where the $\omega_{\mathcal{O}}(a,p)$ is the fuzzy distance between a and p in $\mathcal{O}$ [45]. Therefore, following Definition 1, p inherits the thickness from an axial point a for which the measure $\tau_{\mathcal{O}}(a) - \omega_{\mathcal{O}}(a,p)$ is maximized; in other words the term $\omega_{\mathcal{O}}(a,p) - \tau_{\mathcal{O}}(a)$ is minimized and the task is accomplished by the following algorithm.

begin *algorithm-thickness-inheritance-from-axial-points*

input:

$\mathcal{O}, O$: a fuzzy object and its support

$A, \tau_{\mathcal{O}}$: the set A of axial points of $\mathcal{O}$ and the thickness value $\tau_{\mathcal{O}}(a)$ at each axial point $a \in A$

output:

the thickness value $\tau_{\mathcal{O}}(p)$ at every object point $p \in O$

auxiliary data:

FDT: each non-axial point $p \in O$, $FDT(p)$ is the negative of the fuzzy distance from the farthest MIB circumference

NAP: for each object point $p \in O$, $NAP(p)$ indicates the center of the MIB whose circumference is farthest from p

Q: a queue indicating the points yet to be processed

initialization:

for all axial points $a \in A$

$FDT(a) = -\tau_{\mathcal{O}}(a)$

$NAP(a) = a$

push a in the Q

for all non-axial points $p \in O$

$FDT(p) = \text{maxValue}$

$NAP(p) = p$

propagation:

while Q is non-empty

pop a point p from Q

for all point $p' \in N^*(p)$

if $FDT(p') > FDT(p) + (f_{\mathcal{O}}(p) + f_{\mathcal{O}}(p'))|p - p'|/2$

$FDT(p') = FDT(p) + (f_{\mathcal{O}}(p) + f_{\mathcal{O}}(p'))|p - p'|/2$

$NAP(p') = NAP(p)$

push p' in Q

thickness inheritance:

for all non-axial points $p \in O$

$$\tau(p) = \tau\big(NAP(p)\big)$$

end *algorithm-thickness-inheritance-from-axial-points*

It should be noted that the above algorithm essentially records the term $-(\tau_O(a) - \omega_O(a,p))$ in FDT which is minimized and the corresponding axial point a is recorded in NAP which eventually determines the inheritance of thickness value τ_O at a non-axial point p.

2.4 Experimental Plan

As mentioned earlier in this chapter, the target application for the new thickness computation algorithm is computation of TB thickness and marrow spacing at *in vivo* MD-CT imaging of human distal tibia. To compute trabecular thickness, a fuzzy representation of bone structure is used where the membership value at a given voxel p represents the bone volume fraction (BVF) at that voxel denoted as $BVF(p)$. Marrow space represents the marrow-filled region among trabeculae. Therefore, marrow spacing among individual trabeculae is computed from marrow volume fraction image (MVF) derived as the inverse of the BVF image as follows:

$$MVF(p) = 1.0 - BVF(p).$$

Equation 2

Computation of both trabecular thickness and marrow spacing are performed using the algorithm described in Chapter 2.2. Specifically, the two TB measures, namely, TB thickness (TH_B) and marrow spacing (SP_M), are computed over a target volume-of-interest (VOI) V as follows:

$$TH_B = \sum_{p \in V} TH_B(p) / |V|$$

Equation 3

$$SP_M = \sum_{p \in V} SP_M(p)/|V|$$

Equation 4

where $|\cdot|$ is the total number of voxels in a region. In addition to the two TB micro-architectural measures, average BMD over the V was computed as described in [181].

The overall experimental study was designed – (1) to evaluate the method's accuracy and stability under random local shifts in axial points and across a wide range of image resolutions, (2) to assess the method's inter-modality correlation and repeat scan reproducibility, (3) to examine the ability of the method to predict TB strength, and (4) to assess the method's application in *in vivo* studies. The accuracy of the method was evaluated using computer-generated phantoms at different levels of noise and down-sampling. The stability of the method was assessed using μ-CT images down-sampled at different image resolutions from 28.5 μm to 199.5 μm covering the range between *in vivo* and *ex-vivo* regimes. Also, the correlations of TB thickness and marrow spacing measures derived from *ex vivo* μ-CT imaging and *in vivo* MD-CT imaging modalities, as well as their repeat-scan MD-CT reproducibility, were examined using cadaveric ankle specimens. Linear correlation of bone measures with experimentally determined bone strength was examined on the same cadaveric specimens. All cadaveric experiments were performed at the distal tibia site and the following sequence of steps was applied to each specimen – (1) MD-CT imaging, (2) removal of soft tissue and dislodgement of distal tibia from the ankle joint, (3) μ-CT imaging, (4) specimen preparation and TB core extraction, and (5) mechanical testing to compute compressive Young's modulus and Yield stress. Application of the method in a pilot study included *in vivo* MD-CT imaging of forty healthy young adult volunteers and ten young-adult athletes. In the following, we describe the materials and methods used to conduct each of these experiments.

2.4.1 Cadaveric specimens and MD-CT and μ-CT imaging

Fifteen fresh-frozen human cadaveric ankle specimens were obtained from 11 body donors (age: 55Y to 91Y). The bodies were collected under the Deeded Bodies Program, The University of Iowa, Iowa City, Iowa, USA, and the ankle specimens were removed at the mid-tibia region. Exclusion criteria for this study were evidence of previous fracture or knowledge of bone tumor or bone metastasis. These ankle specimens were kept frozen until the performance of MD-CT imaging.

High resolution MD-CT scans of the distal tibia were acquired at the University of Iowa Comprehensive Lung Imaging Center on a 128-slice SOMATOM Definition Flash scanner (Siemens, Munich, Germany) using the following CT parameters: Single tube Spiral acquisition at 120 kV, 200 effective mAs, 1 sec rotation speed, pitch factor 1.0, nominal collimation 16×0.3 mm, scan length of 10 cm beginning at the distal tibia end-plateau, and total effective dose equivalent to 17 mrem (≈ 20 days of environmental radiation) in the USA. Following all MD-CT repeat scans, each specimen was further scanned on an Imtek Micro-cat II scanner at 28.5 μm isotropic resolution, after removing soft tissue and dislocating the tibia from the ankle joint.

2.4.2 Mechanical testing and determination of bone strength

Cylindrical TB specimens nominally 8 mm in diameter and 20.9±3.3 mm in length were cored from each distal tibia specimen *in situ* along the proximal-distal direction for mechanical testing. A-P and M-L radiographs were first used to determine the plane of an initial distal cut done to eliminate the growth plate from a test specimen, and then to determine the central axis of the bone and thus the core location; the initial distal cut was located 2 mm proximal to the growth plate. Each specimen was cored with saline immersion using an 8.25 mm inner diameter diamond coring bit (Starlite Industries, Rosemont, PA). The core was released from the distal radius by cutting it with a razor saw, and the specimen ends were sanded smooth, flat, and parallel. Specimen length and

diameter were measured three times and averaged, and the middle 6 mm of the specimen length was marked for extensometer attachment position. For extensometer testing, a minimum specimen length of 18 mm was desired, to achieve both the minimum aspect ratio of 2:1 recommended for TB compression specimens [182] and a 3:1 ratio of specimen length to extensometer gage length used in an earlier study [182]; all specimens satisfied the required aspect ratio. For the subsequent non-extensometer testing, specimen length was dependent on how much bone needed to be removed from the damaged ends. The resulting aspect ratios were all greater than 1:1 for all specimens, except for two with the two-lowest Young's modulus values, which were excluded for the test. Thus, thirteen specimens were used for the non-extensometer test. For both extensometer and non-extensometer tests, specimen length, diameter and its location from the distal tibial endplate were recorded and used to determine the VOI to compute MD-CT-based measures. Each core was wrapped in saline-soaked gauze and frozen until thawed for testing.

Compressive Young's modulus of each TB core was mechanically tested on an electromechanical materials testing machine as shown in Figure 5 (MTS Insight, MTS Systems Corp., Eden Prairie, MN). Each specimen was placed between unlubricated, polished, plano-parallel steel platens. For the extensometer test, to minimize specimen end effects, strain was measured with a 6 mm gage length extensometer (model 632.29F-30, MTS Systems Corp., Eden Prairie, MN) attached directly to the midsection of the bone. For the non-extensometer test, strain was measured with the testing machine at the compressing platens. A compressive preload of 10 N was applied and strains then set to zero. At a strain rate of 0.005 sec^{-1}, each specimen was preconditioned to a low strain with at least ten cycles and then loaded to failure. Young's modulus (E) was determined for each specimen as the highest 20% section slope of the stress-strain curve. Yield stress was determined as the intersection of the stress-strain curve and a 0.2% strain offset of the modulus.

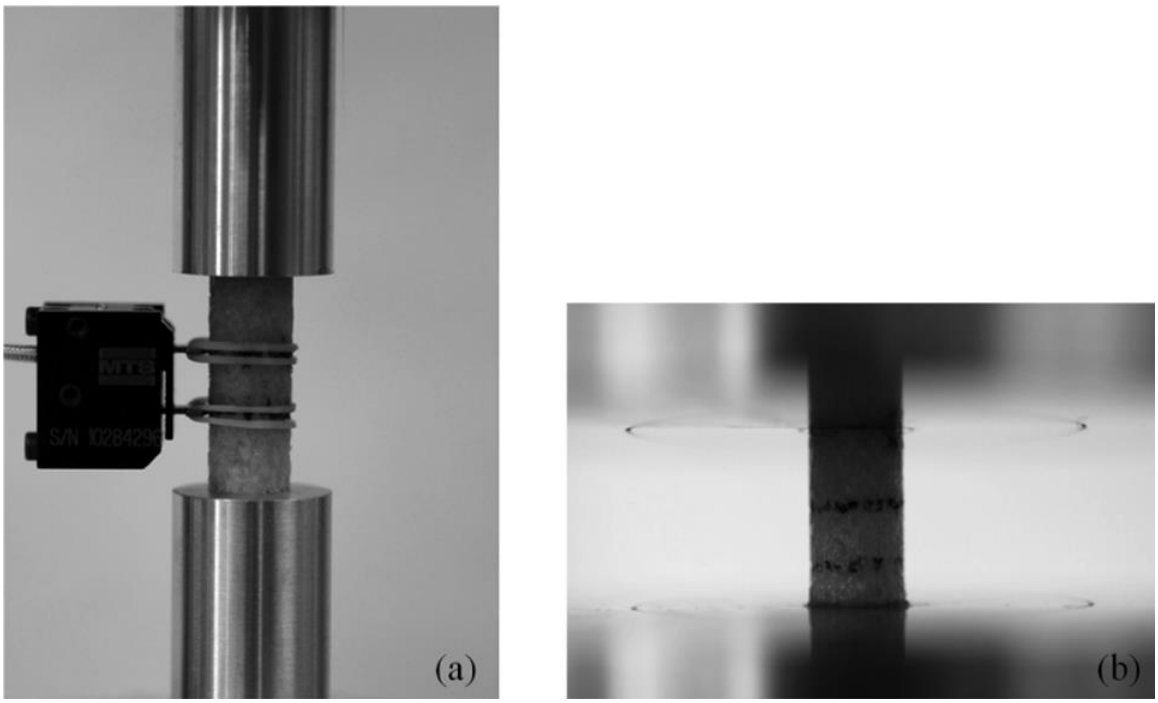

Figure 5 Compressive mechanical testing of TB specimens. (a) Extensometertesting. (b) Nonextensometer testing; note black lines indicating original extensometer position, with damaged bone removed from the bottom (proximal part) of the specimen.

2.4.3 Human volunteers for the *in vivo* study

In vivo MD-CT distal tibia bone scans of twenty healthy male (M) and twenty healthy female (F) volunteers 19 to 21 years of age were collected from the ongoing Iowa Bone Development Study (IBDS). MD-CT scans were performed on the left lower leg of each volunteer following the protocol at 120 kV and 200 effective mA. Each volunteer's tibial length was determined by locating the distal and proximal tibial plateaus in the AP projection MD-CT scout scan of the entire tibia. Along with the healthy volunteers, six male (M) and four female (F) athletes 19 to 21 years of age were recruited and the same MD-CT bone scan was performed.

2.4.4 Image processing

Both cadaveric and *in vivo* MD-CT bone images were processed through the following cascade of steps: (1) computation of BMD image; (2) conversion of BMD to BVF and MFV images; (3) re-sampling of the BVF and MVF image using the windowed-sinc interpolation method to produce 0.15 mm isotropic voxels; and (4) computation of trabecular bone thickness (TH_B) and marrow spacing (SP_M) by applying the thickness computation algorithm of Chapter 2.2 to BVF and MVF images, respectively. For μ-CT images, BVF images were directly computed from the raw CT data using the bimodal intensity distribution. MD-CT imaging acquires data in Hounsfield units (HU) and these numbers were converted to BMD (mg/cc) measures using a calibration phantom. For the experiments presented in this chaper, two different calibration phantoms were used. Specifically, the INTable™ calibration phantom was used for all cadaveric specimen scans, while the Gammax™ calibration phantom was used for all human *in vivo* scans. Finally, a BMD image was converted to BVF image using the following equation [183]:

$$BVF(p) = \begin{cases} 0, & \text{if } BMD(p) < 940\text{mg/cc}, \\ \dfrac{BMD(p) - 940}{2184 - 940} & \text{if } BMD(p) \geq 940\text{mg/cc and } < 2184\text{mg/cc}, \\ 1 & \text{othewise.} \end{cases}$$

Equation 5

2.4.5 VOI selection for the cadaveric study on bone strength prediction

The objective of VOI selection for the cadaveric study was to select a region that is close to the region that was drilled during specimen preparation for mechanical testing. The size and location of these VOIs were chosen as per the information recorded during specimen preparation for each experiment. First, the bone was oriented to align its axis along the coordinate z-axis using the following two steps – (1) generation of a cylinder C with its axis lying on the coordinate z-axis and its cross-sectional area equating to the average tibial cross sectional area, and (2) reorientation of the tibial volume to align its

axis with C by maximizing the overlap between the tibial volume and the cylinder C. After reorienting the bone image, a VOI cylinder of 8 mm diameter along the coordinate z-axis was generated and its proximal end was manually positioned at the center of the cortical rim using in-plane translation through a graphical user interface. The location of the distal end of the VOI cylinder in the slice direction and its length were determined as per the core location and length recorded during specimen preparation; the growth plate was visually located in the CT data of each specimen. Finally, the central 6 mm region from the cylinder was used as the VOI for the extensometer test; for the non-extensometer study, the length of the VOI was determined as per data collected during specimen preparation for the second mechanical test.

2.4.6 Individual-specific VOI selection for the *in vivo* pilot study

The purpose of VOI computation in the *in vivo* pilot study was to adjust the VOI for the individual-specific tibia length and width. The following protocol was adopted for the current study – (1) determination of tibial length by locating distal and proximal end plateaus on the MD-CT scout scan; all proximal sites are defined as percentage of tibial length in reference to the distal end plateau, (2) reorientation of the tibial image to align its axis with the coordinate z-axis using the same protocol described in the previous section, (3) location of the distal end plateau in the MD-CT volume scan, and (4) determination of the ROI at the 5% proximal site of the distal tibia covering 2% of the tibial length after applying a 45% peel on each cross-sectional slice.

2.5 Results

Results of TB thickness measures for three specimens with different experimental mechanical bone strengths are illustrated in Figure 6. As observed in the figure, an 8% difference in BMD from a strong bone (a) to a weak bone (c) leads to a 70% loss in bone strength and manifests as a 20% reduction in TB thickness and a 42% increase in marrow spacing. This observation supports that TB thickness and marrow spacing measures are

highly sensitive to bone loss and therefore, play a significant role in early detection of bone diseases.

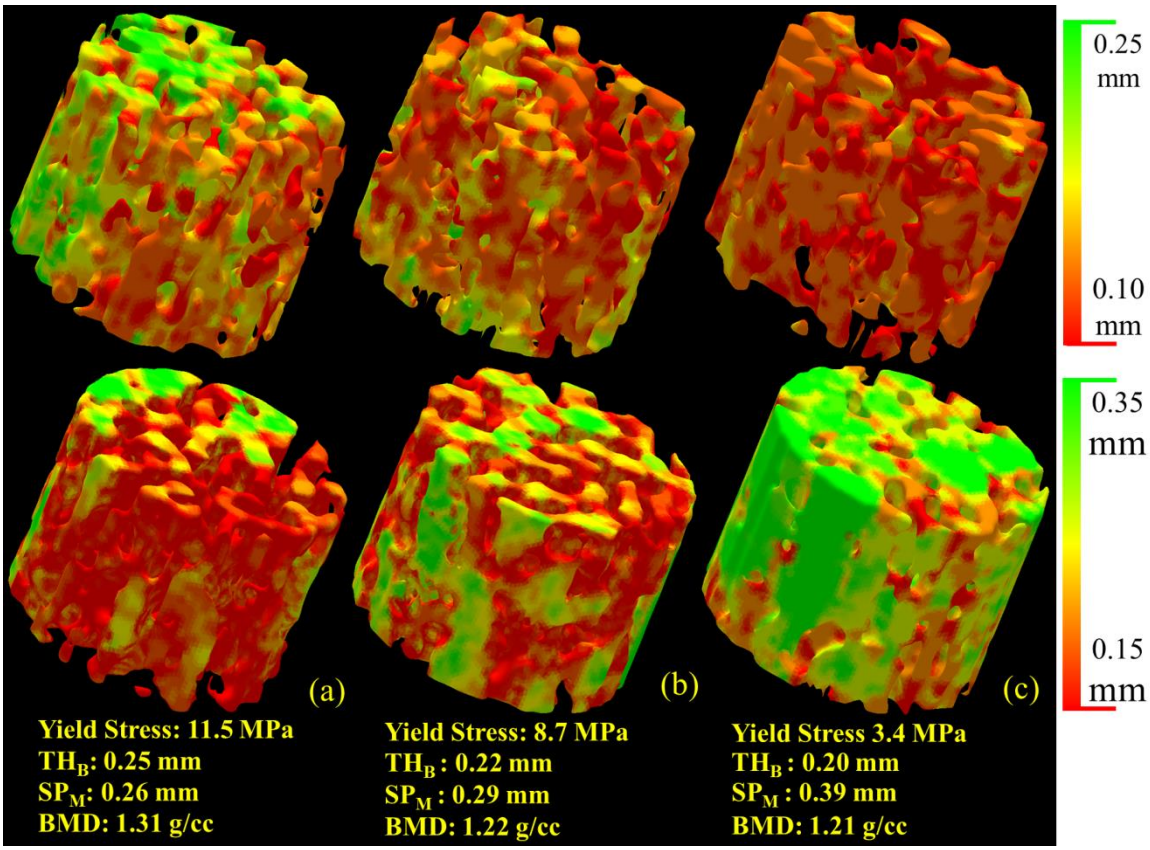

Figure 6 Illustration of the TB thickness and marrow spacing measures for three different TB specimens – (a) strong (yield stress: 11.5 MPa), (b) moderate (7.1 MPa) and (c) weak (3.4 MPa).

2.5.1 Accuracy results

To quantitatively examine the accuracy of the method, three-dimensional (3-D) binary phantoms along with ground true regional thickness distribution at high resolution were generated. Then the test phantom images were generated by down-sampling binary phantoms at $3 \times 3 \times 3$, $4 \times 4 \times 4$, and $5 \times 5 \times 5$ and by adding noise at signal-to-noise ratios (SNR) of 6, 12 and 24. Error was calculated at the individual voxel location in a phantom as the absolute difference between the true and computed thickness values. The

high resolution binary image and the true thickness distribution were generated as follows. The process starts with quasi-uniform sampling of an ideal mathematical skeleton in the continuous 3-D space R^3; let S_{T} be the set of N_{T} number of sampled points. A Euclidean distance transform (DT) was computed from S_{T} and let $DT_{\mathrm{T}}: Z^3 \rightarrow R^+$ denote that DT map. To generate a binary object with non-uniform thickness value, a smooth varying true thickness field, say $f_{\mathrm{thickness}}: Z^3 \rightarrow R^+$, was generated. Finally, a volumetric object corresponding to the true skeleton S_{T} was defined as the set of all voxels with its Euclidean distance DT_{T} not exceeding the local thickness value $f_{\mathrm{thickness}}$. The thickness field $f_{\mathrm{thickness}}$ was used as the true thickness distribution. For the current experiment, six binary objects with true thickness distribution were generated and an example binary object is shown in Figure 7. Let $O \subset R^3$ be the binary object and let $f_{\mathrm{computed},l,\sigma}: Z^3 \rightarrow R^+$ be the thickness distribution of the phantom generated from O at the downsampling rate of l and the noise at SNR of ρ. Thickness computation error is computed using the following equation:

$$Error_{l,\rho} = \frac{1}{|O|} \sum_{p \in O} \left| f_{\mathrm{thickness}}(p) - f_{\mathrm{computed},l,\sigma}(p) \right|.$$

Equation 6

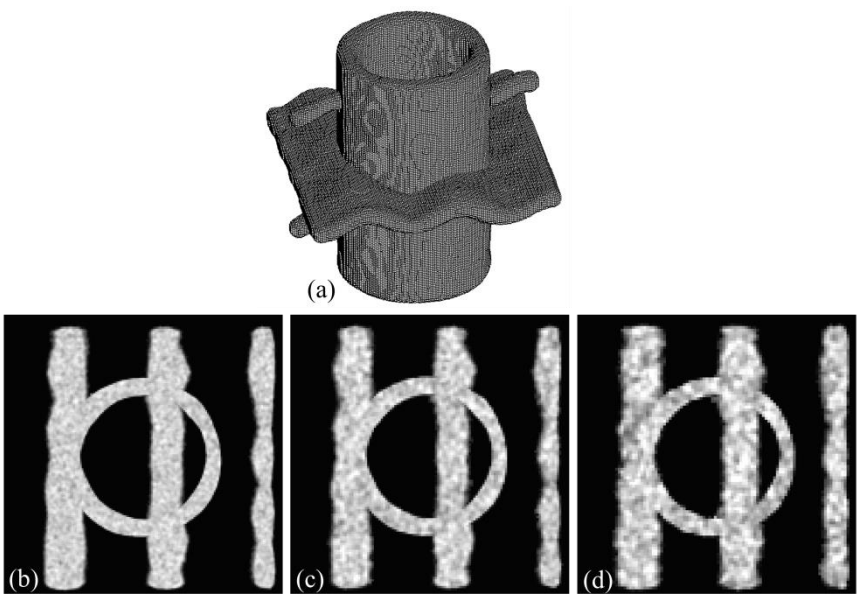

Figure 7 Computer-generated phantoms data at different levels of noise and down sampling. (a) Three-dimensional rendition of the true binary phantom. (b-d) Axial image slices of test phantoms at SNR values of 24, 12 and 6 and down-sampling rates of three, four, and five voxels.

Table 1 Computation error of thickness for different parameters

Different down-sampling	Different methods	Different signal to noise ratio			
		noise free	SNR 24	SNR 12	SNR 6
$3 \times 3 \times 3$	New method	1.04 ± 0.15	1.17 ± 0.22	1.37 ± 0.29	1.53 ± 0.20
	FDT-based	1.29 ± 0.25	1.53 ± 0.37	1.74 ± 0.35	2.18 ± 0.33
$4 \times 4 \times 4$	New method	1.19 ± 0.17	1.31 ± 0.16	1.62 ± 0.24	1.76 ± 0.20
	FDT-based	1.51 ± 0.37	1.78 ± 0.47	1.98 ± 0.47	2.38 ± 0.45
$5 \times 5 \times 5$	New method	1.22 ± 0.20	1.59 ± 0.14	1.82 ± 0.20	2.01 ± 0.20
	FDT-based	2.34 ± 0.10	2.56 ± 0.09	2.71 ± 0.09	2.98 ± 0.15

Note: Thickness computation errors on phantoms at different levels of down-sampling and noise. At each level of down-sampling and noise, the mean and standard deviation of voxel-by-voxel thickness computation errors over the entire object are presented.

The average errors using both the new method and previously reported FDT-based method [14] for six phantoms at each level of noise and down-sampling are presented in Table 1. Clearly, compared to the FDT-based method, the new method produces smaller errors at all different combinations of noise levels and down-sampling rates, and t-tests show the differences are significant, with a p-values < 0.001.

Also, we conducted factor analysis of thickness errors comparing the new and the FDT-based methods. Four factors, namely, Phantom, Method, SNR, and Down-Sampling (DS) were identified for this experiment. One model with the three-way interaction effect, three two-way interaction effects and the three main effects was developed. There was no evidence for a Method×SNR×DS three-way interaction effect. The next model deleted the three-way interaction effect and included the three two-way interaction effects and the three main effects. There was no evidence for Method×SNR or DS×SNR interaction effects; however, the Method×DS interaction effect was significant ($p<0.0001$). That indicates that the pattern of mean errors for the new and FDT-based methods are different across the three rates of DS (as can be seen in Figure 8 that a more dramatic increase in the FDT-based method mean errors across the three DS rates). The final model included the Method×DS interaction effect as well as the three main effects. The Method×DS interaction effect was significant ($p < 0.0001$) as was the SNR main effect ($p < 0.0001$). Because of the interaction effect, pairwise comparisons between methods were conducted at each level of DS and the results show that the two methods are significantly different ($p < 0.0005$). The Bonferroni procedure was used to correct for the three pairwise comparisons.

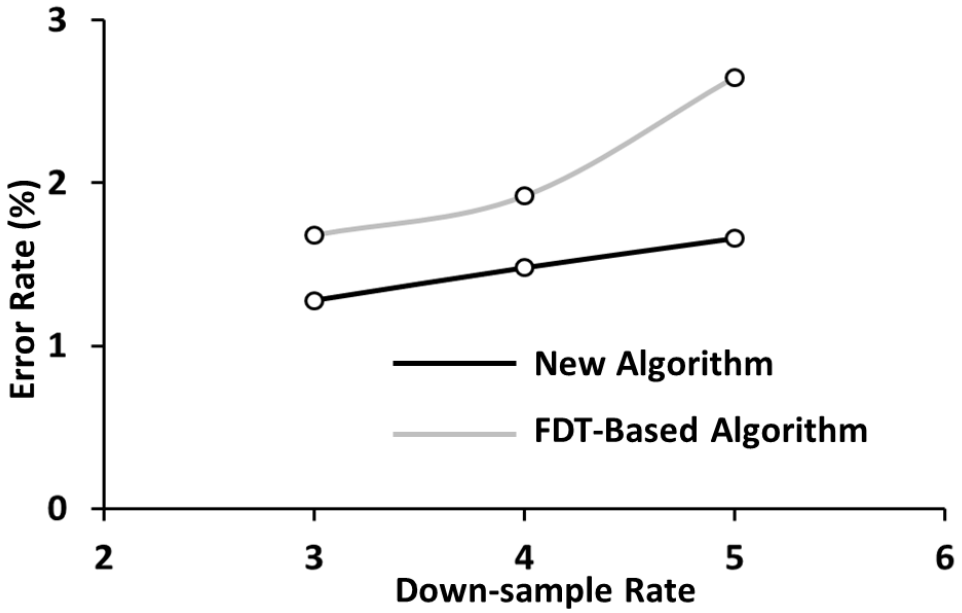

Figure 8 Illustration of the error rate against down-sampling rate between the proposed method and the FDT-based methods.

2.5.2 Robustness under various conditions

Three different experiments were under-taken to assess the robustness of the new method. The first experiment was designed to examine robustness of the method under errors in skeletal location. The motivation for this experiment was to examine whether the new thickness computation algorithm is prone to the digitization error of skeletal location, the issue discussed by Saha *et al.* [116]. For this purpose, each computed skeletal voxel [112] was randomly replaced by one of its $3 \times 3 \times 3$ neighbors and then Steps 2 and 3 of the thickness computation algorithm were followed. In this experiment, each image point is considered as a test instance generated from MD-CT images of fifteen ankle specimens. The mean and standard deviation of voxel-by-voxel errors in TB thickness computation were 8% and 6%, respectively. It should be mentioned that 8%

and 6% thickness computation errors at 150 μm resolution are equivalent to ~0.12 and 0.09 voxel errors. Further, it should be mentioned that the error was reduced to 3% or 0.04 voxel when an average thickness over VOI of 1 mm^3 was taken.

To quantitatively examine the stability of the thickness computation method, we applied the method on ten μ-CT images each down-sampled at six different resolutions. Specifically, ten μ-CT images of original isotropic voxel size of 28.5 μm were used for this experiment and each of these images was down sampled at six lower isotropic resolutions of 57.0 μm, 85.5 μm, 114.0 μm, 142.5 μm, 171.0 μm and 199.5 μm as shown in Figure 9. Computed mean thickness values for different specimens at various resolutions are illustrated in Figure 10(a). Thickness computation error for a specific μ-CT image at a given down-sampled resolution was computed as the difference of mean thickness values computed at the given and the original μ-CT resolutions. Finally, the average and standard deviation of thickness computation error at a given resolution was computed over the ten μ-CT images and the results are shown in Figure 10(b). As observed in Figure 10(a), despite a wide range of down-sampling resolutions covering *ex vivo* to *in vivo* resolution regimes, the average thickness error is only 4.3%. These results demonstrate that the new thickness computation method is highly stable across a wide range of resolutions.

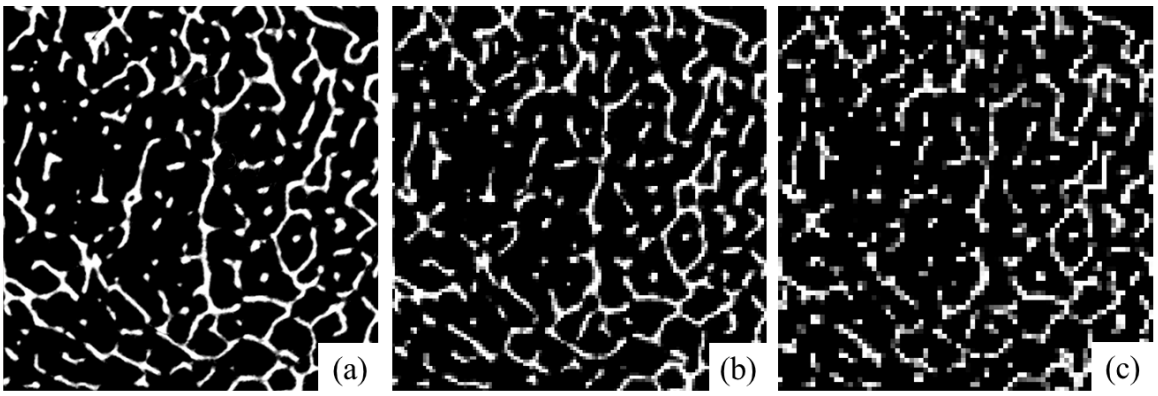

Figure 9 Illustration of the μ-CT down sampled at different levels of resolution: (a) 28.5 μm, (b) 114.0 μm, and (c) 199.5 μm.

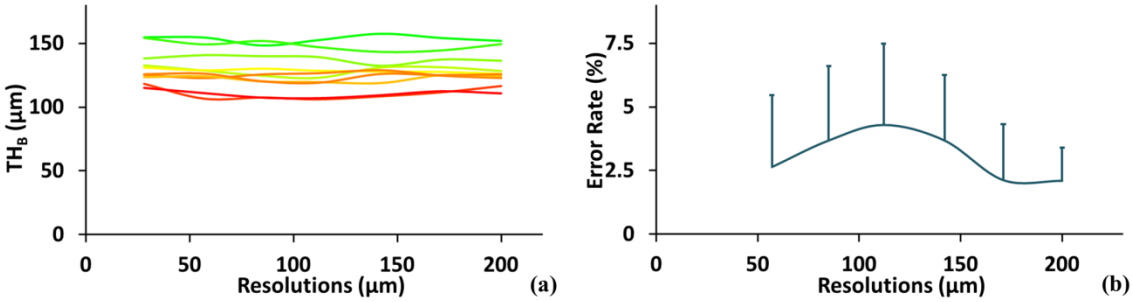

Figure 10 Illustration of the stability of the new algorithm across different image resolutions. (a) The mean thickness τ_O over a cylindrical VOI change as the resolution changes. (b) The Error of the mean thickness value τ_O as the resolution changes compared to the average thickness from all ten images.

To further examine the performance of the algorithm under different resolutions, the correlation of TB thickness computed from *ex vivo* μ-CT and *in vivo* MD-CT imaging was examined. The purpose of this experiment is different from the previous experiment. In the previous experiment, different resolutions were obtained computationally, while the current experiment examines the performance of the method for different image acquisitions using two widely different modalities in the presence of modality-dependent

artifacts. Matching axial image slices from post-registered μ-CT and MD-CT images of a cadaveric specimen are presented in Figure 11. As observed in the figure, the trabecular structures are generally thicker in MD-CT imaging due to a larger modulation transfer function (MTF) of the MD-CT image. The linear correlations of TB thickness and marrow spacing computed from post-registered μ-CT and MD-CT images are presented in Figure 12. The R^2 values from a linear regression model of TB thickness and marrow spacing measures in two different modalities are 0.93 and 0.91, respectively, with slopes of 1.66 and 1.08, respectively. For both measures, the regression line passes near the origin.

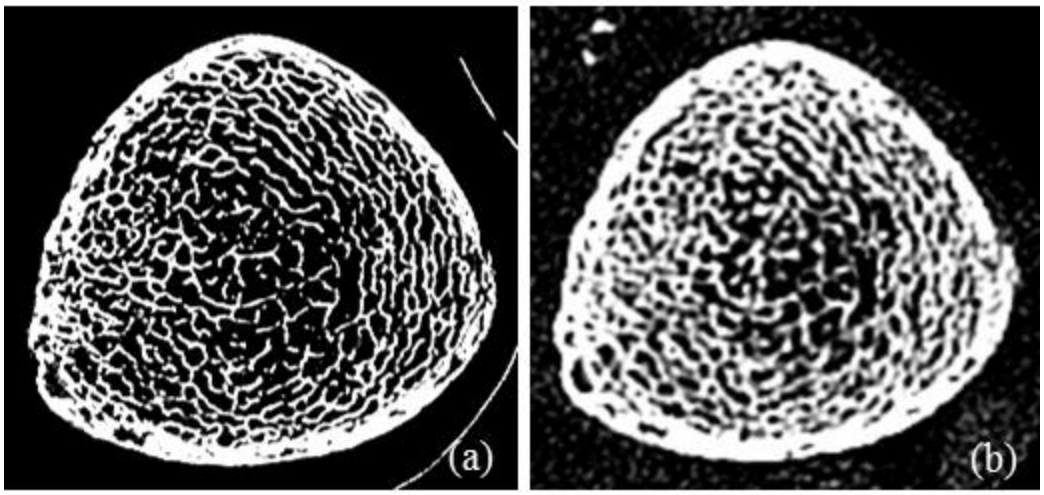

Figure 11 Illustration of matched axial image slices from post-registered μ-CT and MD-CT images of a cadaveric specimen: (a) μ-CT and (b) MD-CT.

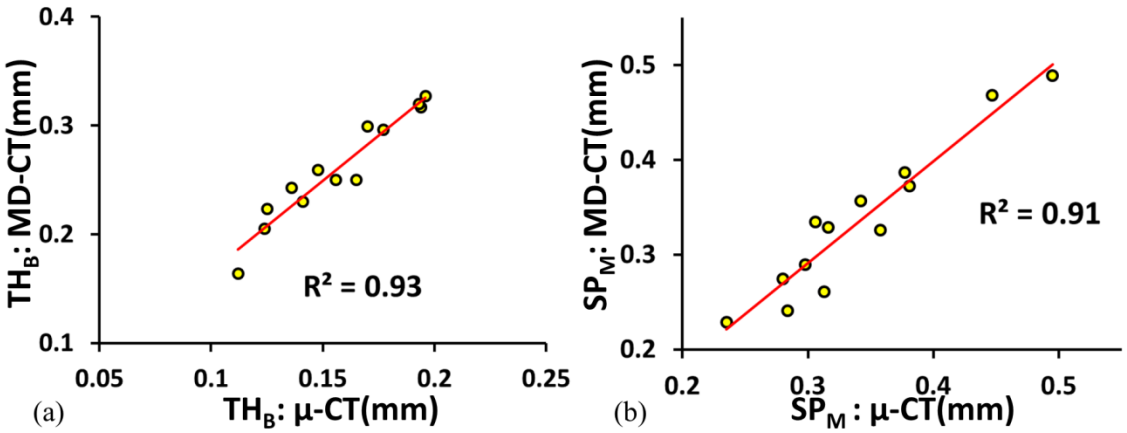

Figure 12 Illustration of the linear correlation of TB thickness and marrow spacing computed from post-registered μ-CT and MD-CT images: (a) TB thickness and (b) marrow spacing.

2.5.3 Reproducibility analysis

Three repeat MD-CT scans of fifteen cadaveric ankle specimens were used to examine the method's reproducibility. Figure 13 illustrates a color-coded TB thickness map over a matching volume in two repeat MD-CT-scans of the distal tibia. For quantitative analyses, ten spherical VOIs of the same radius were randomly selected in the first MD-CT scan of each specimen above the position 8 mm proximal to the distal endplate, leading to a total of 150 VOIs. A post-registration algorithm was used to locate the matching VOIs in the second and third repeat scans. It is obvious that the result of reproducibility analysis depends on the scale of VOI, with larger VOIs showing improved reproducibility. The relationship between the method's reproducibility and VOI size is presented in Figure 14. It is observed in the figure that, for the new method, at a VOI diameter of 3.45 mm or greater, the intra-class correlation coefficient (ICC) exceeds the value of 0.95, suggesting that the measure is highly reproducible for assessing regional bone alteration. For the conventional FDT-based approach, the VOI diameter has to reach 6.15 mm to achieve equivalent performance in terms of the ICC.

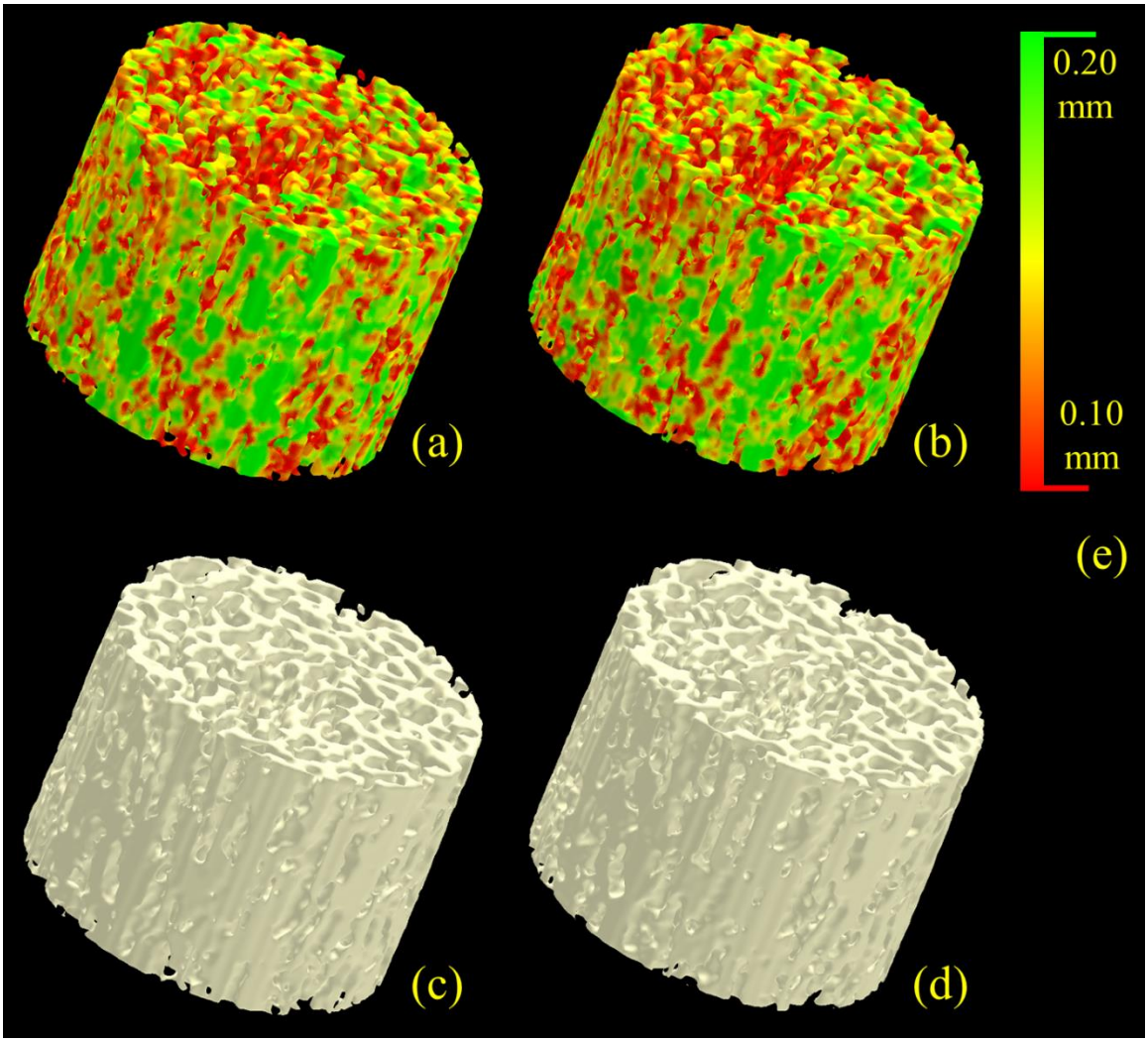

Figure 13 Illustration of reproducibility of the TB thickness measure under repeat MD-CT scans. (a-b) color coded trabecular bone thickness images. (c-d) trabecular bone image without color coding. (e) color coding bar. Specimens were repositioned on the CT table before each repeat scan.

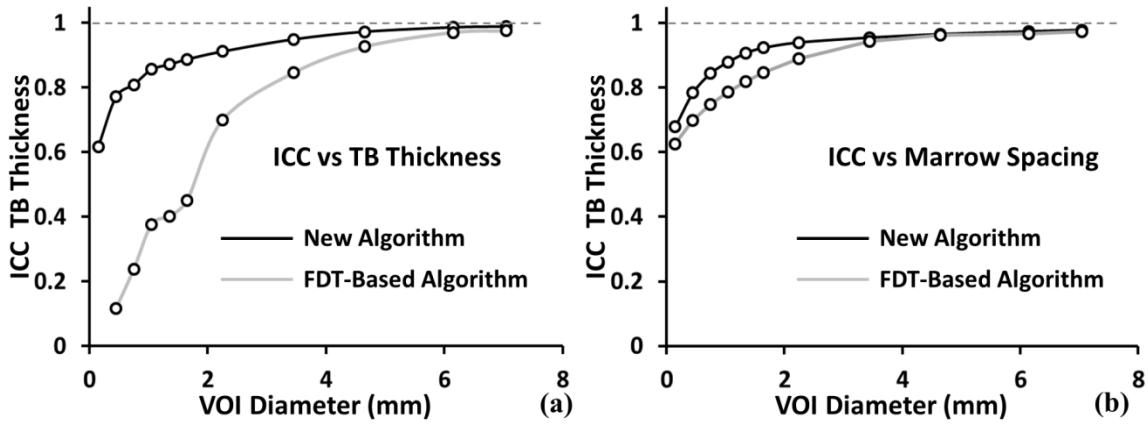

Figure 14 Illustration of repeat MD-CT scan ICC values at different VOI diameters using both the new algorithm and FDT-based algorithm. As displayed, at a VOI diameter of 3.45 mm or greater, the ICC value using the new algorithm exceeded the mark of 0.95, while the TB thickness measure using the FDT-based algorithm requires a VOI diameter of 6.15 mm or greater.

2.5.4 Predicting bone strength

To examine the ability of TB thickness and marrow spacing computed by the new method to predict bone strength, a linear correlation analysis between each of the two measures and the TB's experimental Young's modulus and Yield stress was performed. The image-based measures were computed over a cylindrical VOI with its axis aligned to that of the distal tibia and its length and position selected, as per the data recorded during specimen preparation and mechanical, testing as described in Chapter 2.4.5. The results of correlation analysis between Yield stress and each of the TB thickness and marrow spacing measures using the new method are shown in Figure 15(a,b) while the results using the FDT-based algorithm are shown in Figure 15(c,d). The values of R^2 of the linear correlation between TB Young's modulus and the different TB measures are presented in Table 2. For both Yield stress and Young's modulus parameters, the TB thickness and marrow spacing measures computed using the new method have

demonstrated superiority in predicting bone strength as compared to the FDT-based measures and MD-CT based volumetric BMD.

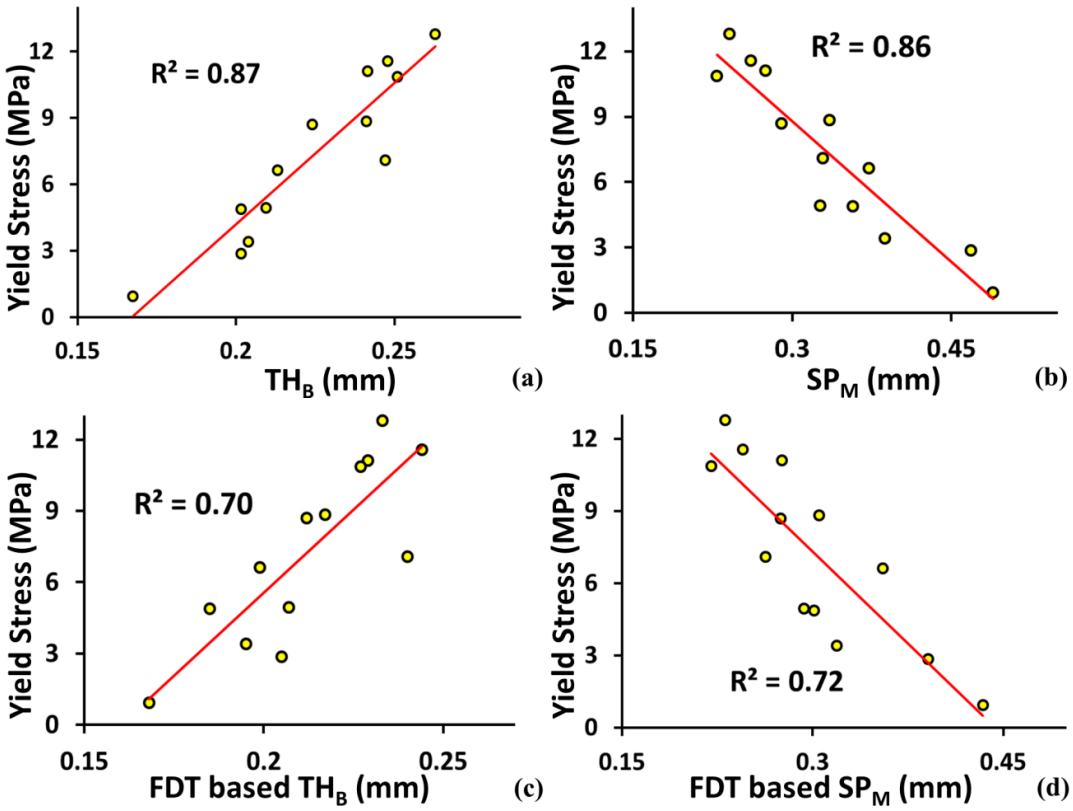

Figure 15 Ability of different TB measures using the new algorithm to predict bone strength shown in terms of R^2 values of linear correlation between yield stress and each of TH_B (a) and SP_M (b). (c,d) Same as (a,b) but for the FDT-based method [116].

Table 2 Results of linear correlation (R^2 values) between TB thickness and marrow spacing measures and experimental TB strength parameters.

TB strength parameters	New method		FDT-based method		BMD
	TH_B	SP_M	TH_B	SP_M	
Young's Modulus	0.83	0.85	0.61	0.74	0.78
Yield stress	0.87	0.86	0.70	0.72	0.79

2.5.5 Results of *in vivo* pilot study

To evaluate the effectiveness of the method, *in vivo* MD-CT data of twenty male and twenty female volunteers (19Y to 21Y) were used to form body mass index (BMI) order-matched male-female pairs. The BMI was 26.89$\pm$6.32 kg/m^2 (mean $\pm$ SD.) for males and 25.15$\pm$7.96 kg/m^2 for females, and R^2 for the two ordered groups of BMIs was 0.96. TB thickness and marrow spacing measures were computed for the 40 volunteers over the ROI discussed in Chapter 2.4.5. The colored results for one male-female pair are shown in Figure 16. Clearly, the results indicate that the male has thicker TB than the female. Quantitative results show that males on average have 6.7% thicker TB and 13.9% reduced marrow spacing as compared to females. Paired t-test results showed the differences were statistically significant with p-values $<$0.03 for both TB thickness and marrow spacing. Using the FDT-based methods, males on average have 2.6% thicker TB and 12.3% reduced marrow spacing as compared to females, with p-values of 0.29 and 0.12 for TB thickness and marrow spacing, respectively.

In vivo MD-CT data from ten athlete volunteers (six male and four female) were processed. Collegiate athletes who were actively participating at the varsity-level in volleyball or basketball were recruited from regional colleges and universities. All athletes were screened to ensure that they had not been injured in the previous year. A control group was formed by selecting among the 40 healthy volunteers, ten with the same gender and the most similar BMI index. The mean BMIs were 23.73 $\pm$ 1.56 kg/m^2 for athletes, and 24.07 $\pm$ 1.83 kg/m^2 for the control group, and R^2 for the two groups of height is 0.96. The colored results for one athlete and one non-athlete with similar BMI values are shown in Figure 17. Obviously, the results indicate that the athlete has thicker TB than the non-athlete. Quantitative results show that athletes on average have 9.4% thicker TB and 11.0% reduced marrow spacing as compared to sex and BMI-matched healthy controls. Results of paired t-tests showed the differences were statistically significant with p-values of 0.01 and 0.04 for TB thickness and marrow spacing,

respectively. Using FDT-based methods males on average have 10.0% thicker TB and 9.3% reduced marrow spacing as compared to females, with p-values of 0.07 and 0.14 for TB thickness and marrow spacing, respectively.

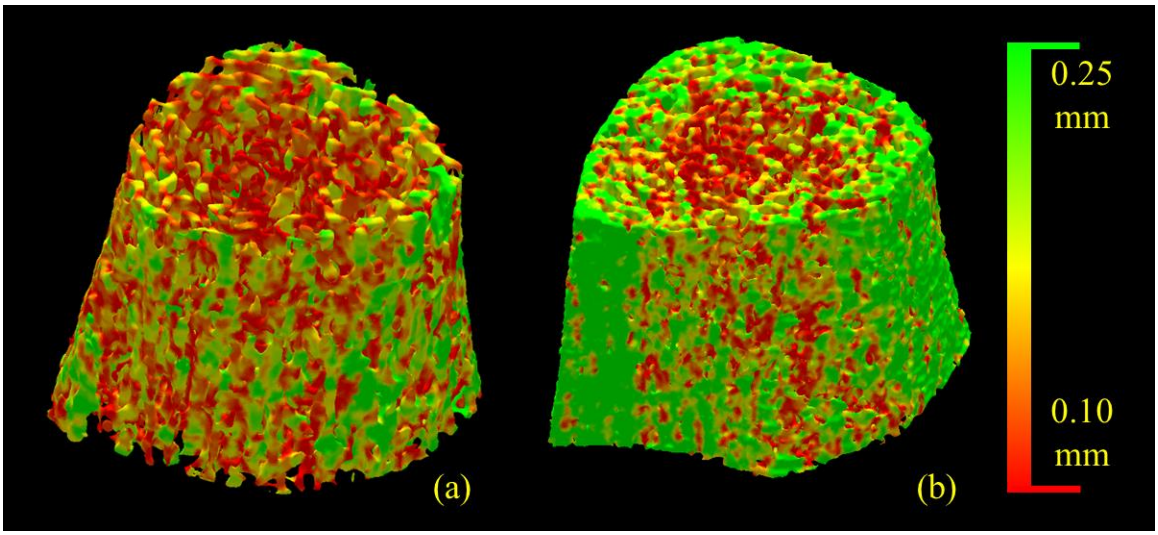

Figure 16 Illustration of the new thickness computation algorithm for *in vivo* imaging on an age-BMI-similar female and male pair: (a) female healthy volunteer and (b) male healthy volunteer.

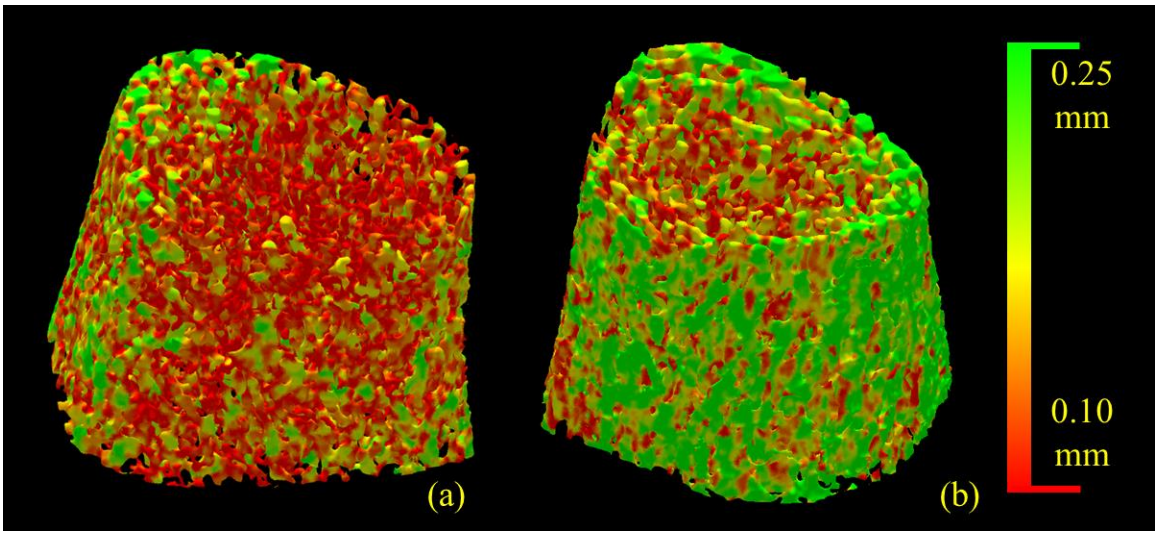

Figure 17 Same as Figure 16, but comparison between an age-sex-BMI-similar athlete and a non-athlete: (a) non-athlete and (b) athlete.

2.6 Conclusion

In this chapter, we presented a new thickness computation algorithm for fuzzy digital objects at relatively low resolution and have investigated its role in computing TB thickness and marrow spacing measures through MD-CT imaging under *in vivo* conditions. Results of a comprehensive study on computer-generated phantoms and fifteen cadaveric ankle specimens evaluating the new method were presented. Observed results demonstrated encouraging accuracy and stability of computed thickness at different levels of noise and down-sampling. Also, high repeat MD-CT scan reproducibility of the new thickness computation method was observed in the cadaveric ankle study. TB thickness and marrow spacing measures demonstrated higher ability to predict trabecular bone's experimental mechanical properties under *in vivo* conditions as compared to bone mineral density and conventional FDT-based methods. Currently, we are investigating the power of the new method to characterize clinical groups in terms of their bone health. Also, *in vivo* data from forty age-similar and BMI order-matched male and female volunteers demonstrated that males have significantly thicker trabeculae and significantly reduced marrow spacing as compared to females. Although similar differences in TB thickness and marrow spacing between males and females were observed for FDT-based measures, they were not statistically significant. A second experiment on ten basketball or volleyball athletes and age-sex-BMI-similar sex healthy matched the controls showed that, using the current method, athletes have significantly thicker TB and significantly reduced marrow spacing. A similar analysis using FDT-based measures marginally failed to demonstrate statistically significant differences in TB thickness and marrow spacing between and athletes and healthy matched controls.

CHAPTER 3. TENSOR-SCALE-BASED QUANTITATIVE ANALYSES OF TRABECULAR BONE MICRO-ARCHITACTURE

This chapter describes the theory and algorithm for t-scale computation that is applicable to fuzzy digital object representation (here, TB structure) at relatively low resolutions. For the current application, the membership value at a given image voxel is interpreted as a partial occupancy of bone within the voxel, termed the bone volume fraction (BVF). To characterize structural geometry the proposed algorithm finds the largest ellipsoid fitting within the local TB structure. In the rest of this chapter, we will use Z^3, where Z is the set of integers, to denote the underlying *image voxel grid* or *image grid* and $BVF: Z^3 \rightarrow [0,1]$ to denote the function providing bone volume fraction at image voxel s. Also, let R^3 denote the *continuous three-dimension (3-D) space*. An element of the image grid Z^3 will be referred to as an *image voxel*, or simply, a *voxel*. An element of R^3 will referred as a *point*. Several novel improvements are made for this 3D t-scale algorithm, listed as follows:

<u>Novel research works as presented in this chapter:</u>

1) Improvement in t-scale computation algorithm.
2) Introduction of t-scale-based "axial-point" with sub-voxel precision.
3) Computation of local structure measures at axial points and propagate those measures to non-axial points in the volumetric data using a feature propagation algorithm.
4) Computation of different t-scale-based TB measures.

3.1 Tensor Scale Computation

Tensor scale (t-scale) [131] at a point p inside an object O is the parametric representation of the maximally included ellipsoid centered at p, where the maximality of the three semi-principal axes is accomplished in the reverse order of their lengths. In other words, first, a ball is isotropically grown from its center p until it hits the boundary

of O and it defined the first semi-axis of t-scale; then the circle on the orthogonal sub-space is allowed to grow until it hits the boundary of O in the sub-space; and so on. Saha [131] provided a computational solution for tensor scale based on sample line tracing while Xu *et al*. [184] presented a computationally efficient algorithm using differential geometric approaches. Here, we leverage the original sample line-based approach since it alleviates digitization effects at low resolutions by ellipsoid fitting. The process of t-scale computation at point p is schematically illustrated in Figure 18. For simplicity, 2-D illustrations are used while the method is described in 3-D. The method is based on tracing pairs of radially opposite sample lines that emanate from a point p and locate the closest feature edge on every sample line (pink points in Figure 18(a)). The edge points are repositioned to ensure axial symmetry (yellow points in Figure 18(a)). Finally, the t-scale at p is determined by computing the best-fit ellipsoid to the repositioned edge points (Figure 18(b,c)). The following steps described this process in detail.

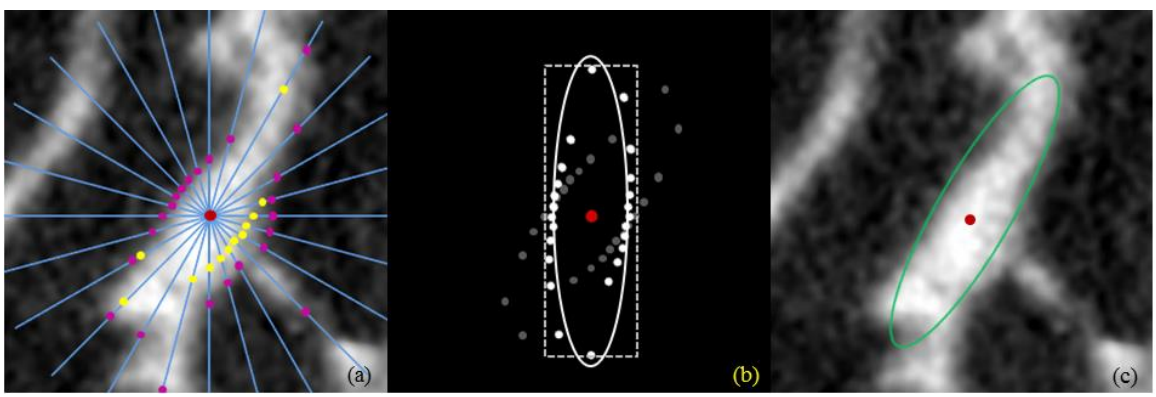

Figure 18 2D Illustration of steps in t-scale computation. (a) Radially opposite sample line pairs (blue) with the candidate point as origin (red), edge points (pink) on radial sample lines (blue) and repositioned edge points (yellow) from the center point (red). (b) The edge point and repositioned edge points (gray) are translated the original and rotated to align with the coordinate axis (white) after applying PAC on the points, bounding box (dotted) and the best-fit ellipse (grey) (c) Final t-scale ellipsoid (green).

Step 1: Edge detection along sample lines

First, m pairs of mutually opposite sample lines over the entire 3-D angular space are selected at a pseudo uniform distribution to ensure the final t-scale is not skewed in any direction. Here, we have used an approximate 22.5^{o} of angular separation between neighboring sample lines leading to m= 40 pairs of sample lines. The choice of m was made by analyzing the trade-off between computation time and accuracy performance; the current computation time for a human bone data over an ROI of $200 \times 200 \times 200$ voxels is approximately 40 minutes. Two other parameters, namely, the sampling interval, δ, and the sample line length, L, are necessary. L defines the set maximum possible length of individual trabeculae in one direction; here, we have used $L = 5$ mm. δ defines the step-size between two successive test edge points on a sample line and is set based on the scale of the finest detectable structure. Assuming that the image resolution is appropriate for the target application, we recommend choosing δ between '1' and '0.5' times the smallest dimension of a pixel. Following the Nyquist theorem of sampling, $\delta = 0.5$ is sufficient for reconstruction of a signal and therefore, setting $\delta < 0.5$ offers no additional benefit. On the other hand, if $\delta > 1$ is used, we clearly miss one voxel thick structures in an image. In this chapter $\delta = 0.5$.

The ith sample line γ_p^i emanating from any point p in the continuous 3-D space R^3 may be defined as a vector sequence of sample points $\gamma_p^i[0], \gamma_p^i[1], \cdots, \gamma_p^i[M_L]$, where, $\gamma_p^i[0] = p$ and $M_L = L/\delta$. The BVF value at each sample point $\gamma_p^i[j]$ is computed by tri-linear interpolation of BVF values at the eight image voxels on the $2 \times 2 \times 2$ bounding box of $\gamma_p^i[j]$. Finally, the edge on the sample line $\boldsymbol{\gamma}_p^i$ is located at a distance v_p^i from p,

$$v_p^i = \sum_{j=0}^{e_p^i - 1} \delta \frac{\left(BVF\left[\gamma_p^i[j]\right] + BVF\left[\gamma_p^i[j+1]\right]\right)}{2},$$

Equation 7

where, e_p^i is the first sample point on $\boldsymbol{\gamma}_p^i$ with interpolated BVF as zero indicating a full-background location. In the above equation, the term $\left(BVF\left[\gamma_p^i[j]\right] + BVF\left[\gamma_p^i[j+1]\right]\right)/2$ represents the average density over the interval between the two successive sample points $\gamma_p^i[j]$ and $\gamma_p^i[j+1]$. The multiplication of the average density with step-size δ accounts for partial voluming.

Step 2: Repositioning edge points

The edge points obtained in Step 1 describe the boundary of the local object centered at the image point p. Following the axial symmetry of an ellipsoid, as demonstrated by Saha [131], for each pair of opposite sample lines the two edge points should be equidistant from p, which is the center of the t-scale ellipsoid. However, the detected edge points on a local structure do not necessarily satisfy this property. For example, in Figure 18(a), the edge locations colored pink on the lower-right sample lines are mostly farther from the candidate point p than corresponding opposite sample lines. Therefore, the edge points need to be repositioned by analyzing the edge points on every pair of sample lines. Specifically, between the two edge points on a pair of sample lines, the one closer to p is selected and reflected on its complementary sample line. The edge locations colored yellow are obtained using this repositioning algorithm. In the rest of this chapter, "edge point" will refer to "repositioned edge point".

Step 3: T-scale ellipsoid fitting

The last step in t-scale computation is to fit an ellipsoid to the repositioned edge points. In our application, the number of edge points is significantly larger than the number of parameters needed to represent an ellipsoid. The literature on ellipsoid fitting is quite mature with several established approaches [185-187]. All ellipsoid fitting approaches essentially minimize the error between the observed data (here, the edge points) and the computed ellipsoid. Primarily, these methods differ with respect to the nature of these errors. When errors are defined using algebraic distance, a canonical solution can be

derived leading to a computational efficient solution. However, the solution may not be stable for highly anisotropic data sets, and in our application such situations may occur frequently. The geometric distance approach generates stable solutions for most ellipsoids and uses a more natural Euclidean distance metric. Unfortunately, it is difficult to derive a canonical form solution for ellipsoid fitting that optimizes geometric distance error, and therefore, a geometric distance based approach commonly utilizes optimization. Here, the geometric distance error is used and the fitting algorithm is summarized as follows (Figure 18(b)):

Step 3.1 Translate all edge points, moving the candidate point p to the origin.

Step 3.2 Apply principle component analysis (PCA) to edge points computing eigenvectors $\left(\mathbf{i}_1(p), \mathbf{i}_2(p), \mathbf{i}_3(p)\right)$ of the point-distribution.

Step 3.3 Rotate the edge points to align $\mathbf{i}_1(p)$, $\mathbf{i}_2(p)$, and $\mathbf{i}_3(p)$ with the three coordinate axes.

Step 3.4 Determine the smallest box enclosing all edge points and use it to determine the eigenvalues for the initial guess of the best-fit ellipsoid.

Step 3.5 Compute the final ellipsoid by applying iterative minimization of the sum of geometric distance errors using the Newton's optimization algorithm. Let $\left(\lambda_1(p), \lambda_2(p), \lambda_3(p)\right)$ be the length of the three semi-principal axes of the ellipsoid.

Step 3.6 Set the t-scale at the point p as the ellipsoid with the three semi axes – $(\lambda_1(p)\mathbf{i}_1(p), \lambda_2(p)\mathbf{i}_2(p), \lambda_3(p)\mathbf{i}_3(p))$.

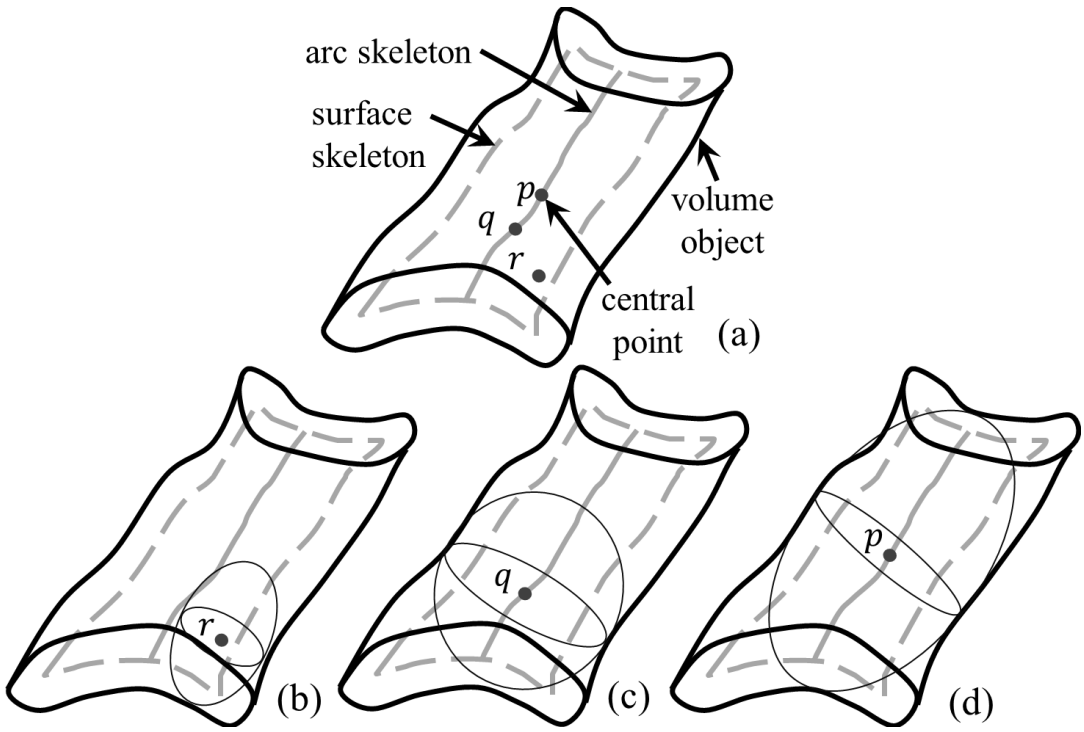

Figure 19 Illustration of the t-scale ellipsoid fits for different points on the TB structure. To obtain accurate descriptions of local dimensions, these measures must be derived from the mid-point of the respective dimension. (a) A generic trabeculae with sample points defined on the surface skeleton, r, the arc skeleton, q, and defined at the central point on the structure, p. (b) T-scale accurately captures the thickness information only when considering an arbitrary point on the surface skeleton; (c) captures the thickness and width information when considering a point on the arc skeleton; and (d) captures all three dimensions when considering the central point.

3.2 Characterization of Individual Trabeculae

As described in the previous chapter, t-scale at a point p is represented by three eigenvectors $\left(\mathbf{i}_1(p), \mathbf{i}_2(p), \mathbf{i}_3(p)\right)$ and corresponding eigenvalues $\left(\lambda_1(p), \lambda_2(p), \lambda_3(p)\right)$, which may be used to quantify geometric properties of the local structure. At this point, it is important to understand how the representative points are defined while characterizing a specific geometric property of a local structure. An elongated plate-like structure may be broken down into its surface skeleton and arc skeleton as shown in Figure 19(a), see

reference [41]. Three different geodesic measures may be defined on the structure – (1) thickness, i.e., the smallest dimension, (2) width, the second largest dimension, and (3) length, the largest dimension. To obtain accurate descriptions of local dimensions, these measures must be derived from the mid-point of the respective dimension. Thus on the surface skeleton (e.g., the point r in Figure 19(b)) of the structure, the smallest semi-axis provides the correct local thickness of the structure. However, the t-scale information at r may not be used to define local with of the structure. To accurately compute the width of local structure, it is important to reduce another dimension of freedom for representative points. In other words, the local width should be defined by the second largest semi-principal axis of t-scale at a point (a point q in Figure 19(c)) of the arc skeleton. The length of the structure should be defined at the mid-point p (see Figure 19(d)) of arc-skeleton. In the current application, t-scale is used to define the orientation and the plate-width of individual trabeculae, thus both local trabecular width and orientation is defined from t-scale at points on arc-skeleton; such points will be referred to as "axial points". Finally, at non-axial points, the local structure width and orientation are inherited from the nearest axial point. This step is solved using the classical feature propagation algorithm introduced in Chapter 2.3.

Spatial discretization of voxels in a digital image puts yet another hurdle that the axial voxel may not coincide to the true axial point of the object in the continuous space. This hurdle is solved by optimizing the location of each axial point using t-scale and initialization at axial voxels as follows:

begin *algorithm-find-axial-points*

input:

$\mathcal{O}$: a fuzzy object

A : the set A of axial voxels of $\mathcal{O}$ computed from skeletonizaion

a_{v}: axial voxel in A

output:

a_{p}: closest axial point at continuous space from a_{v}

initialization:

for all axial points $a_{\mathrm{v}} \in A$

$a_{\mathrm{p}} = a_{\mathrm{v}}$

repeat:

compute the t-scale at a_{p} with eigenvectors $\left(\mathbf{i}_1(a_{\mathrm{p}}), \mathbf{i}_2(a_{\mathrm{p}}), \mathbf{i}_3(a_{\mathrm{p}})\right)$

compute local structure intercepts v_2 and v_3 at a_{p} by $\mathbf{i}_2(a_{\mathrm{p}})$ and $\mathbf{i}_3(a_{\mathrm{p}})$

reposition a_{p} at the middle of the intercepts v_2 and v_3

until convergence of the axial point a_{p} or a maximum of three iterations

end *algorithm-find-axial-points*

In the rest of this chapter, the t-scale inherited from the nearest axial point will be used for characterization of local structure properties. Let $\mathbf{i}_j(p)$ and $\lambda_j(p)$, where $j = 1,2,3$, denote the three eigenvectors and eigenvalues, respectively, at a given axial voxel p. Relevant structural measures are demonstrated on a sample TB structure in Figure 20. The orientation of individual trabeculae, denoted by $TS_O(p)$, is defined by the cosine of the angle θ between the eigenvector $\mathbf{i}_1(p)$, corresponding to the largest eigenvalue, and the bone's longitudinal axis (see Figure 20(b)). The local structure width at p, denoted by $TS_W(p)$, may be defined using twice the length of the second largest eigenvalue $\lambda_2(p)$ (see Figure 20(d)). The normalized plateness measure in the [0,1] scale, denoted by $TS_P(p)$, is classically defined using the square of the anisotropy between the length of the second largest eigenvalue $\lambda_2(p)$ and the smallest eigenvalue $\lambda_3(p)$ as follows:

$$TS_P(p) = \sqrt{1 - \left(\frac{\lambda_3(p)}{\lambda_2(p)}\right)^2}.$$

Equation 8

It may be noted that the above plateness measure essentially provides a characterization of individual trabeculae between perfect plate and perfect rod. More importantly, it does not require threshold values as needed in VTA. The normalized rodness measure $TS_R(p)$ is defined as:

$$TS_R(p) = 1 - TS_P(p)$$

Equation 9

The entire process of t-scale based characterization may be summarized in the following steps.

Step 1. Compute the axial line A for the TB structure O where O is set of all voxels with nonzero BVF values.

Step 2. For each axial voxel $a_{\mathrm{v}} \in A$, derive the optmized location of the axial point a_{p} as described earlier.

Step 3. At each axial point a_{p}, compute t-scale and derive TB measures – $TS_W(p)$, $TS_O(p)$, $TS_P(p)$ and $TS_R(p)$ as defined above.

Step 4. At each non-axial voxel, inherit the TB measures from the nearest axial point as in Chapter 2.3.

In the above algorithm, axial lines are computed as the arc-skeleton using the algorithm by Saha *et al.* [41] and the noise removal procedure presented in [41]. Feature propagation uses the classical algorithm introduced in [41]. Finally, several TB measures are defined in the following. In these equations, V represents the volume of interest (VOI) over which these parameters are defined, $BMD(p)$ and $BVF(p)$ are used to indicate bone mineral density (mg/cc) and bone volume fraction at a voxel p:

1. Bone mineral density:

$$BMD = \sum_{p \in V} BMC(p)/|V|,$$

Equation 10

2. Surface width:

$$SW_{TS} = \sum_{p \in V} TS_W(p) BMC(p) / \sum_{p \in V} BMC(p) \ ,$$

Equation 11

3. Surface curve ratio:

$$SCR_{TS} = \sum_{p \in V} TS_P(p) BMC(p) / \sum_{p \in V} TS_R(p) BMC(p),$$

Equation 12

4. Longitudual bone mineral density:

$$BMD_{\text{Long}} = \sum_{p \in V} TS_O(p) BMC(p) / |V|,$$

Equation 13

5. Transverse bone mineral density:

$$BMD_{\text{Tran}} = \sum_{p \in V} \big(1 - TS_O(p)\big) BMC(p) / |V|.$$

Equation 14

3.3 Experimental Plan

The main experimental plan setup will be similar Chapter 2.4. Unlike Chapter 2.4.3, we use ten patients (five male, five female) with selective serotonin reuptake inhibitor (SSRI)-treated, who have been on continuous treatment with an SSRI for at least one year.

3.4 Results

Results of t-scale assessment of TB orientation, $TS_O(p)$, and plate width, $TS_W(p)$, on a μ-CT image of a cadaveric ankle specimen are illustrated in Figure 20. $TS_O(p)$ successfully distinguishes between the longitudinal (green) and transverse (red) trabeculae, Figure 20(b). $TS_W(p)$ on the same μ-CT image is presented in Figure 20(d) and the analogous measure from VTA [41] is presented in Figure 20(e). There is strong agreement between t-scale- and VTA-based plate/rod classifications of individual trabeculae. However, at several locations (indicated by arrows in Figure 20(d-e)), the

gradation of TB plate-width along individual trabeculae is smoother as compared to VTA based results. The sharp changes in VTA based assessment of TB plate-width is primarily due to digitization error of path propagation.

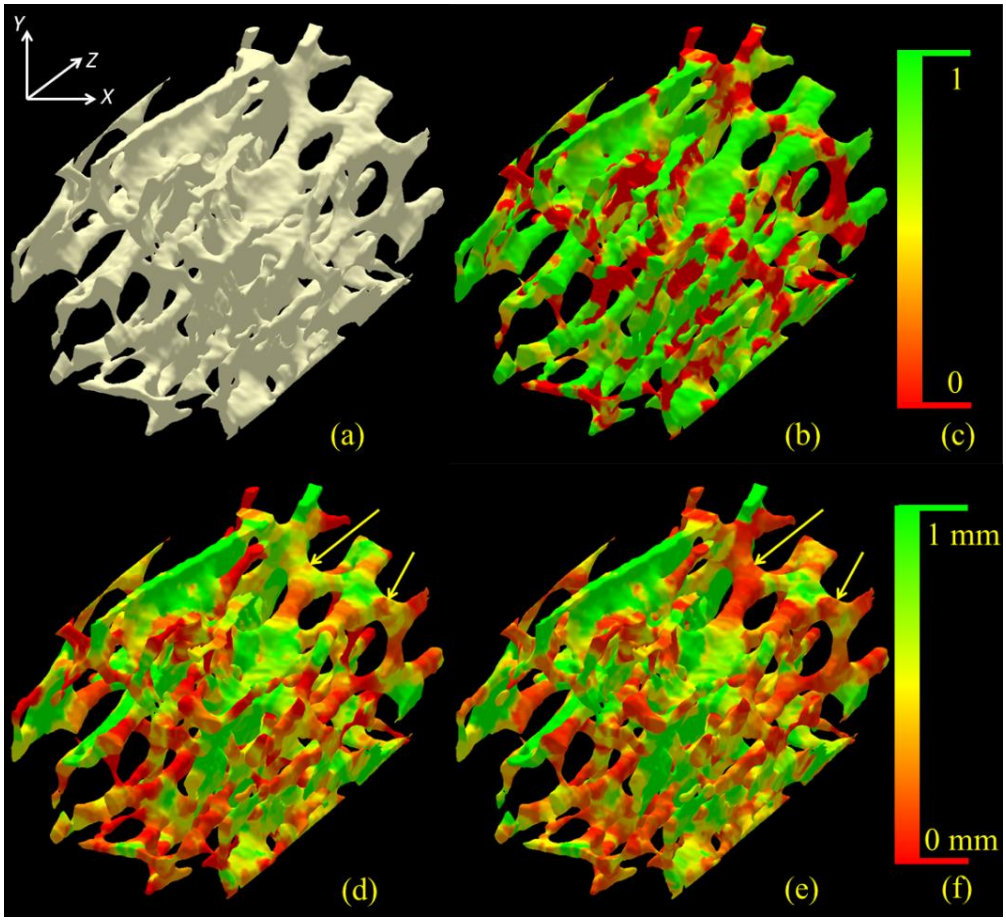

Figure 20 Characterization of TB structure analysis using the t-scale. (a) One TB region selected from μ-CT image of a human ankle specimen. (b) TB orientation analysis using t-scale. (c) Color-coding for (b). (d-e) TB characterization on the continuum be-tween a perfect plate (green) and a perfect rod (red) using the t-scale (d) and VTA (e). (f) Color-coding for (d-e).

Results of t-scale-based plateness classification of TB network for three specimens with different experimental bone strengths are shown in Figure 21. An 8% difference in BMD from a strong bone (a) to a weak bone (c) leads to a 70% loss in bone

strength and manifests into about 33% difference in TB plate-width SW_{TS}, 30% difference in surface to curve ratio SCR_{TS} measures and about 10% difference in TB longitudual bone mineral density $BMDl_{TS}$, establishing high sensitivity to bone degeneration.

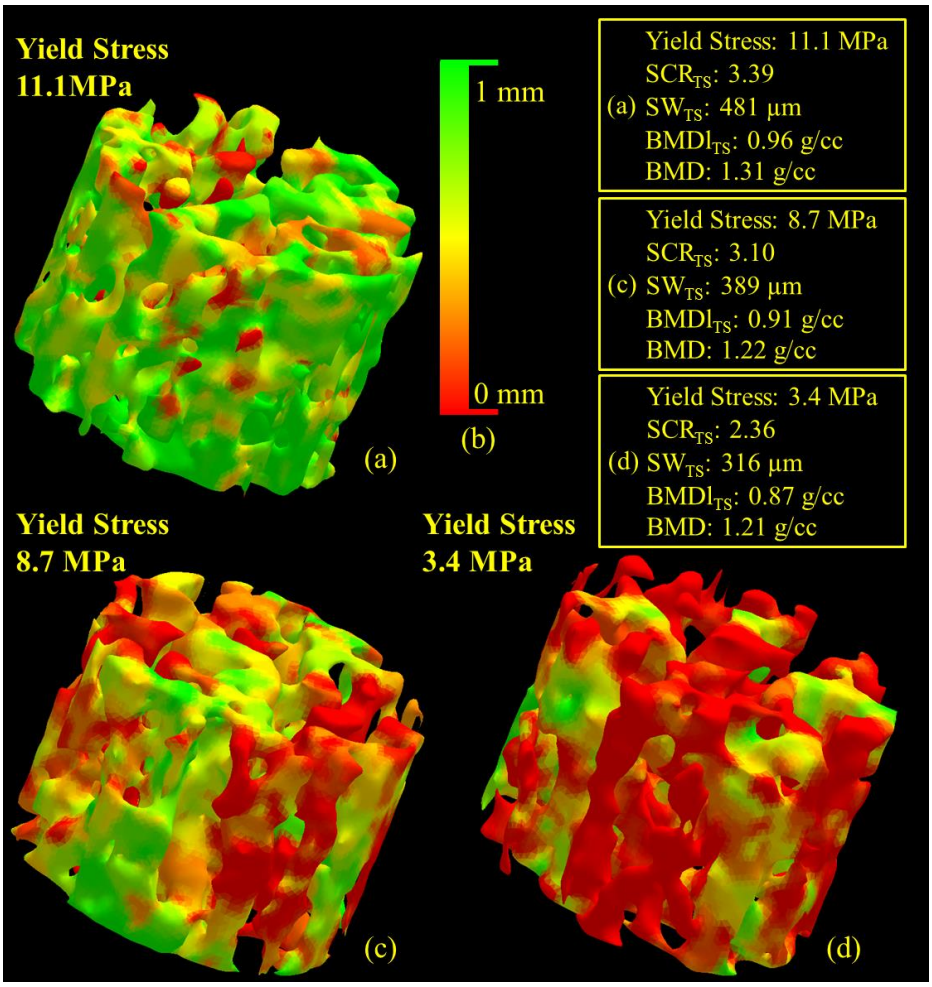

Figure 21 Illustration of the t-scale plate measure for three different TB specimens - (a) strong (Yield stress: 11.1MPa), (c) moderate (7.1MPa) and (d) weak (3.4 MPa). (b) Color bar.

3.4.1 Accuracy results

To quantitatively examine the accuracy of the method, 3-D binary phantoms with different widths at 50 μm resolution were generated. Then, the test phantom images were

generated by down-sampling binary phantoms to 150 μm resolution and by adding Gaussian noise at signal-to-noise ratios (SNR) of 12. SW_{TS} was calculated over the entire phantom region, and error was computed as the difference between the true width and SW_{TS}. Linear correlations between the known plate width and the computed mean plate width using t-scale, SW_{TS}, and VTA, SW_{VTA}, are shown in Figure 22. The average error for SW_{TS} was 0.364 mm compared to 0.663 mm error for SW_{VTA} with a p-value of 0.03, Figure 23.

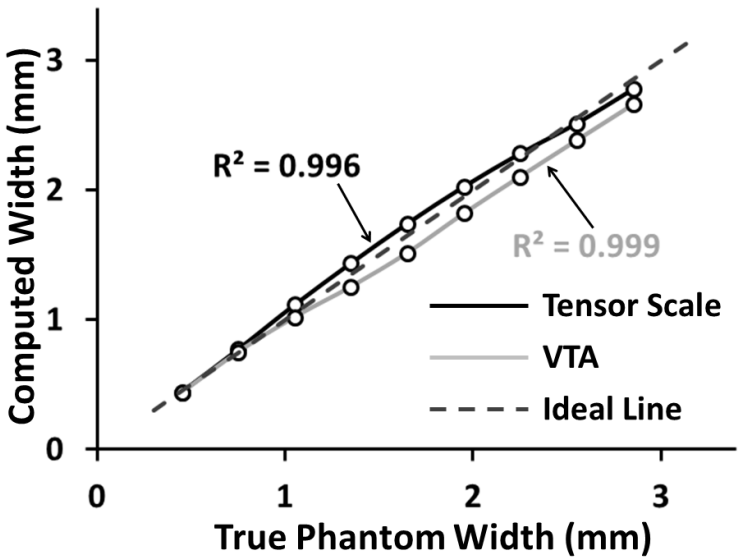

Figure 22 Results of linear correlation analysis between true structure width and computed width using t-scale and VTA methods on computational phantoms.

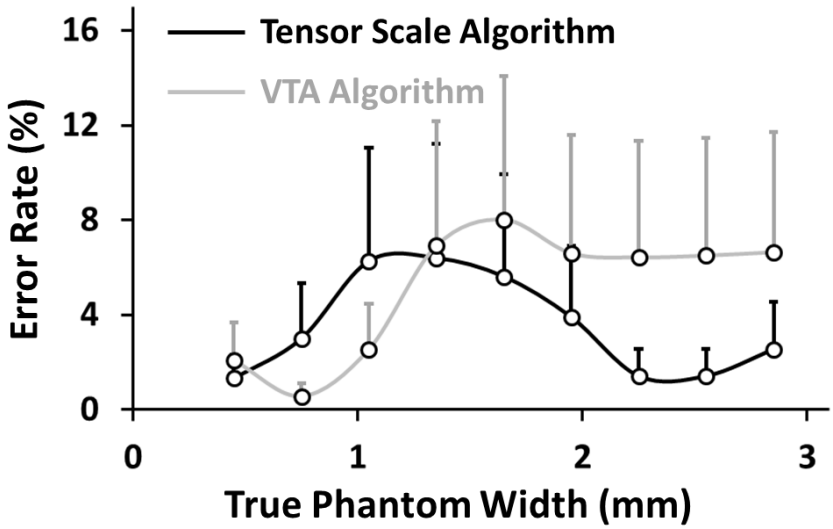

Figure 23 Illustration of error rate for different phantoms using t-scale and VTA.

3.4.2 Robustness under various conditions

The t-scale method stability was evaluated using down-sampled μ-CT images of cadaveric specimens. Specifically, ten μ-CT images of original isotropic voxel size of 28.5 μm were down-sampled to six isotropic resolutions of 57.0 μm, 85.5 μm, 114.0 μm, 142.5 μm, 171.0 μm and 199.5 μm. Variability in SW_{TS}, SCR_{TS}, and $BMDl_{TS}$ at the tested resolutions are illustrated in Figure 24(a-c). The error in the measures for a specific μ-CT image at a given down-sampled resolution was computed against the respective value at the original μ-CT resolution. Finally, the average error and standard deviation of all measures at a given resolution was computed over the ten μ-CT images, Figure 24(d-f). Despite a wide range of down-sampling resolutions covering *ex vivo* to *in vivo* resolution regimes, the average error is less than 6% for all t-scale measures. These results demonstrate high stability for the new t-scale computation method across a wide range of resolutions.

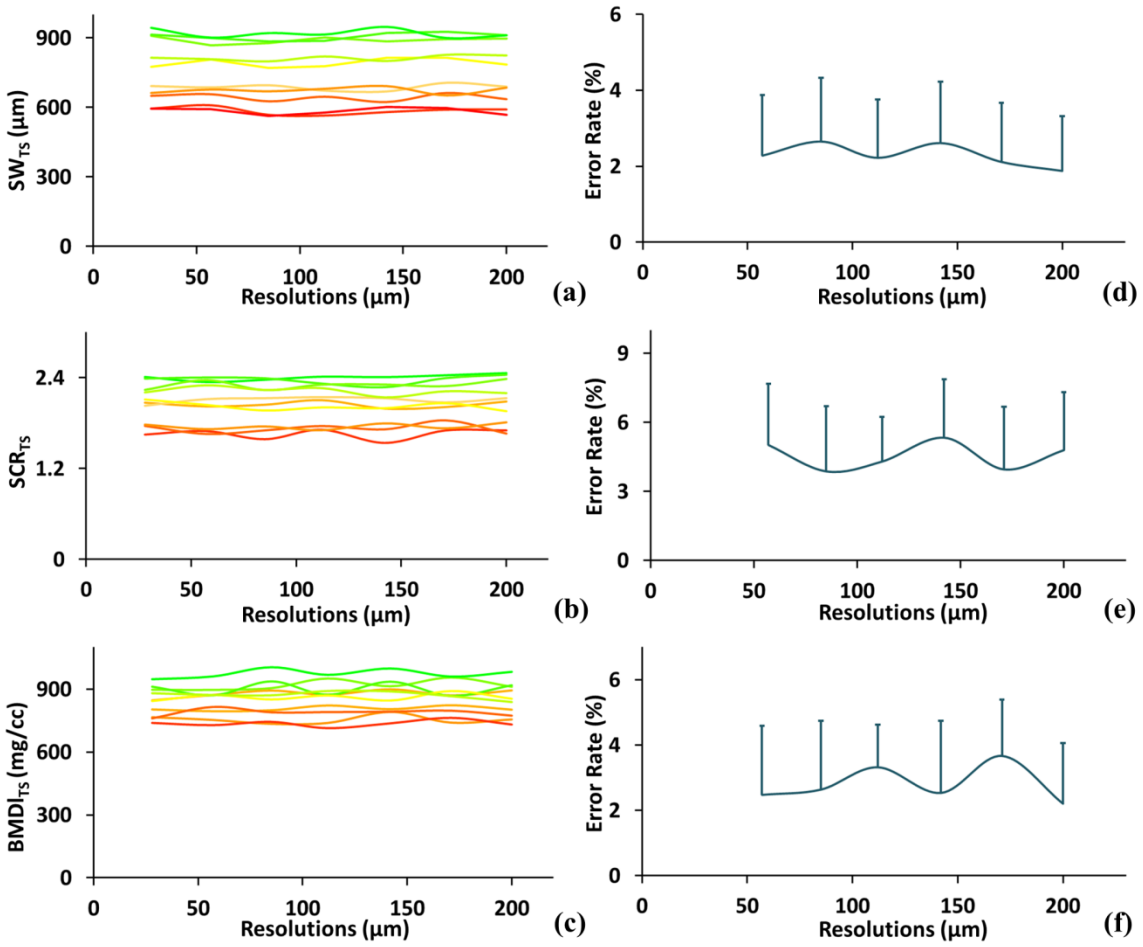

Figure 24 Illustration of the stability of the t-scale algorithm across different image resolutions. (a-c) The mean plate width measures SW_{TS} (a), the mean surface to curve ratio SCR_{TS} (b) and longitudual bone volume fraction $BMDl_{TS}$ (c) over a cylindrical VOI change as the resolution changes. (d-f) The Errors of the corresponding measures SW_{TS} (d), SCR_{TS} (e), and $BMDl_{TS}$ (f) as the resolution changes compared to the average thickness from all ten images.

To further examine the stability of the algorithm under different resolutions, the correlation between t-scale measures computed from *ex vivo* µ-CT and *in vivo* MD-CT imaging was examined. In the previous experiment, different resolutions were obtained computationally, while the current experiment examines the stability of the method between two different modalities in the presence of modality-dependent artifacts. Matching axial image slices from post-registered µ-CT and MD-CT images of a

cadaveric specimen are presented in Figure 11. The trabecular structures are generally wider in MD-CT imaging due to a larger modulation transfer function (MTF). The linear correlation between the MD-CT and μ-CT modalities was high for all TB measures; R^2 values are listed in Table 3:

Table 3 Results of linear correlation (R^2 values) of different TB measures between MD-CT and μ-CT

TB strength parameters	T-scale			VTA	
	SW_{TS}	SCR_{TS}	$BMDl_{TS}$	SW_{VTA}	SCR_{VTA}
MD-CT / μ-CT	0.84	0.82	0.82	0.81	0.81

3.4.3 Reproducibility analysis

Three repeat MD-CT scans of fifteen cadaveric ankle specimens were used to examine reproducibility. Ten spherical VOIs were randomly selected in the first MD-CT scan of each specimen (150 total VOIs). Every VOI was at least 8 mm proximal to the distal endplate. A post-registration algorithm was used to locate the matching VOIs in the second and third repeat scans. Reproducibility was tested at increasing VOI sizes. The relationship between the method reproducibility and VOI size is presented in Figure 25. SW_{TS} at a VOI diameter of 1.05 mm or greater has an intra-class correlation coefficient (ICC) that exceeds 0.95. Conversely, SW_{VTA} requires a VOI diameter of 3.15 mm to achieve equivalent reproducibility in terms of the ICC. For surface to curve ratio measures, both methods reach an ICC value of 0.95 with a VOI diameter of 3.15 mm or larger. $BMDl_{TS}$ reaches an ICC value of 0.95 with a VOI diameter of 5.85 mm or larger. The VOI diameter that achieves an ICC value of 0.95 represents the smallest region over which the measures can be reliably computed. In the case of surface width, the t-scale

algorithm proved to be considerably more reliable as the value stabilized at a much smaller VOI diameter.

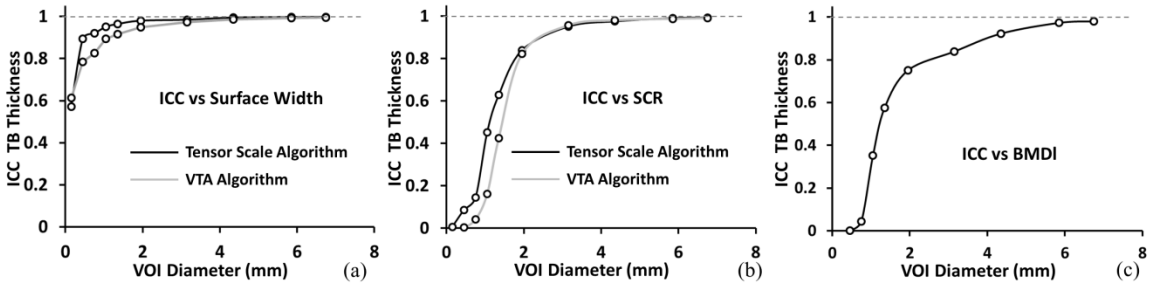

Figure 25 Illustration of repeat MD-CT scan ICC values at different VOI diameters using both the t-scale and VTA. (a) At a VOI diameter of 1.05 mm or greater, the ICC value of plate surface width SW_{TS} using t-scale exceeded the mark of 0.95, while the measure using VTA requires a VOI diameter of 3.15 mm or greater. (b) At a VOI diameter of 3.15 mm or greater, the ICC value of surface to curve ratio SCR_{TS} using both t-scale and VTA exceeded the mark of 0.95. (c) The ICC value of longitudual bone volume fraction $BMDl_{TS}$ at different VOI diameters.

3.4.4 Predicting bone strength

Quantitatively, the ability of t-scale measures to predict bone strength was evaluated by a linear correlation analysis between each measure and the experimental Young's modulus and yield stress assessed by mechanical testing. The image-based measures were computed over a cylindrical VOI as described in Chapter 2.4.5. The correlation analysis using the t-scale measures are shown in Figure 26(a-c) while the results using the VTA measures are shown in Figure 26(d,e). The R^2 values of the linear correlation between Young's modulus and the different image-based measures are presented in Table 4. A "leave-one-out" strategy was used to determine the error of the different measures in predicting bone strength, Equation 15.

$$E = \sqrt{\sum_{i=1}^{n}(e_i - t_i)^2 \Big/ \sum_{i=1}^{n} t_i^{\,2}},$$

Equation 15

where n is the total number of specimens, e_i is the predicted bone strength of the left out specimen i, and t_i is the actual bone strength. The results are shown in Table 5.

Table 4 Results of linear correlation (R^2 values) between different TB measures and experimental TB strength parameters.

TB strength parameters	T-scale		VTA			
	SW_{TS}	SCR_{TS}	SW_{VTA}	SCR_{VTA}	$BMDl_{TS}$	$vBMD$
Young's Modulus	0.79	0.82	0.83	0.85	0.78	0.78
Yield stress	0.92	0.91	0.92	0.87	0.92	0.79

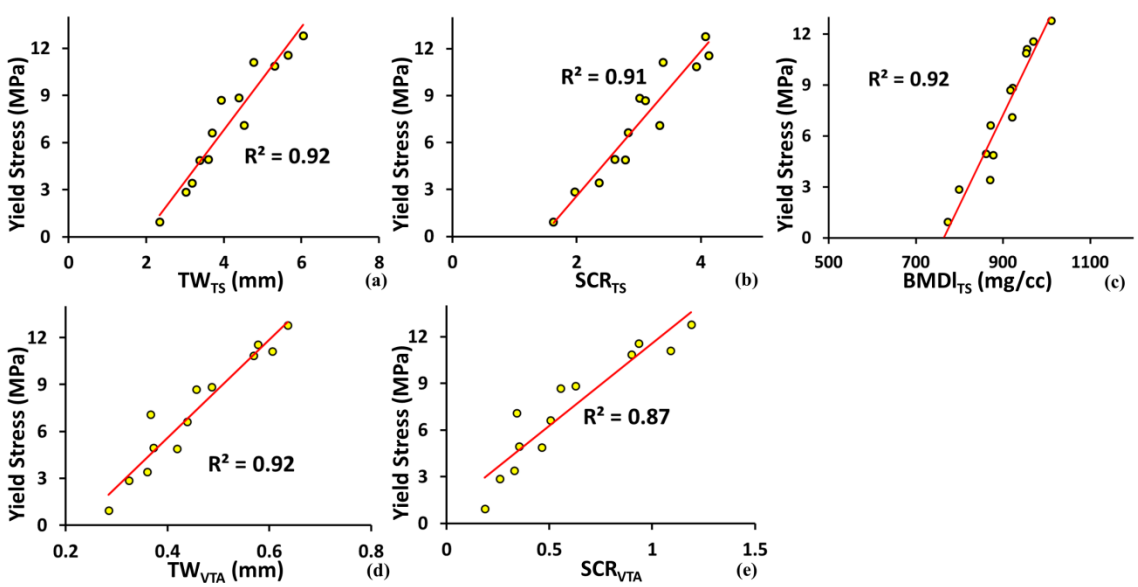

Figure 26 Ability of different TB measures using the t-scale-based method to predict bone strength shown in terms of R^2 values of linear correlation between yield stress and each of TW_{TS} (a), SCR_{TS} (b), and $BMDl_{TS}$. (d,e) Same as (a,b) but for the VTA method [116].

Table 5 Results of "leave-one-out" method for different TB measures in predicting bone strengths

TB strength parameters	T-scale		VTA			
	SW_{TS}	SCR_{TS}	SW_{VTA}	SCR_{VTA}	$BMDl_{TS}$	$vBMD$
Young's Modulus	19.18%	17.54%	21.86%	18.50%	19.41%	23.42%
Yield stress	14.21%	14.98%	14.49%	18.73%	13.94%	23.93%

The t-scale measures of SW_{TS}, SCR_{TS} and $BMDl_{TS}$ correlated higher with yield stress compared to Young's modulus. All architectural measures, by t-scale and VTA, were better predictors on yield stress as compared to $vBMD$, both by linear correlation and leave-one-out analysis. Due to the limited sample size, none of the differences in Table 4 reached statistical significance. Nevertheless, this underscores the importance of considering bone micro-architectural information in addition to bone mass measures when assessing bone health and fracture risk. Furthermore, it demonstrates the ability of t-scale derived architectural measures to capture bone strength information from MD-CT images at *in vivo* resolutions.

3.4.5 Results of *in vivo* pilot study

<u>Male/Female Comparison:</u> To evaluate the effectiveness of the method, *in vivo* MD-CT data of twenty male and twenty female volunteers (19Y to 21Y) were used to form body mass index (BMI) -matched male-female pairs. The BMI was 24.34 ± 3.08 kg/m^2 (mean $\pm$ SD) for males and 22.99 ± 2.27 kg/m^2 for females, with an R^2 value of 0.96 for the two ordered groups of BMIs. T-scale measures (structure plate-width SW_{TS}, surface to curve ratio SCR_{TS}, and longitudual bone mineral density $BMDl_{TS}$) were

computed for the forty volunteers over the ROI discussed in Chapter 2.4.6. The results are contoured on a 3-D representation of the TB structure for one male-female pair in Figure 26. Males on average have 15.7% wider SW_{TS} and 16.3% higher SCR_{TS} as compared to females. Paired t-test results showed the differences were statistically significant with p-values<0.05 for both measures. $BMDl_{TS}$ wasn't significantly different between male and female volunteers.

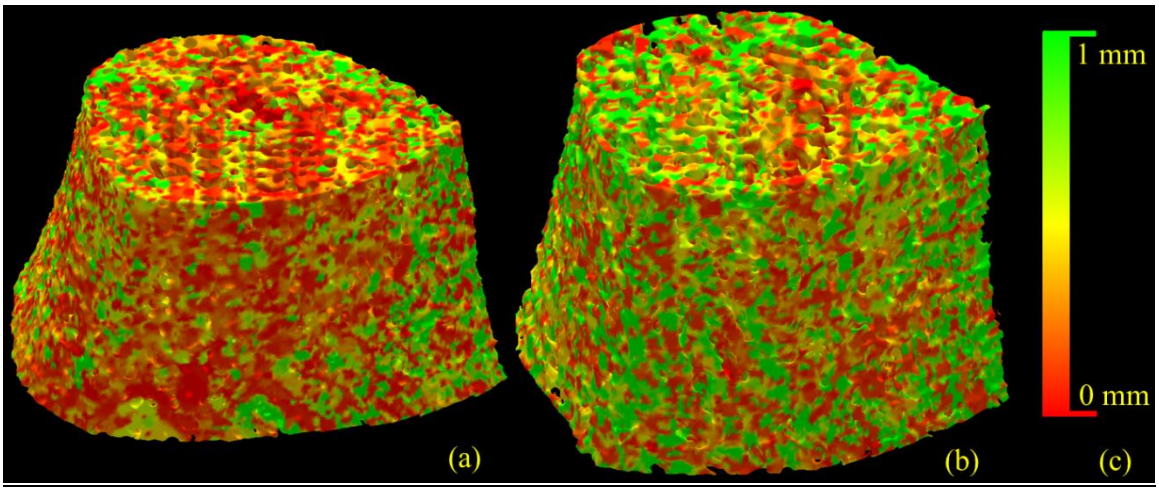

Figure 27 Illustration of the t-scale plate-width measure for *in vivo* imaging on an age-BMI-similar female and male pair: (a) female healthy volunteer and (b) male healthy volunteer.

<u>SSRI/Control Comparison:</u> *In vivo* MD-CT data from ten patients on SSRI treatment (five male and five female) were processed. A control group was formed by selecting gender-BMI-matched controls for the SSRI group participants from the forty healthy volunteers. The mean BMIs were 26.17 ± 2.68 kg/m^2 for the SSRI group, and 26.76 ± 3.08 kg/m^2 for the control group, and R^2 for the two groups of BMI is 0.988. The results indicate that the SSRI group had narrower SW_{TS}, lower SCR_{TS}, and lower $BMDl_{TS}$. The results are contoured on a 3-D representation of the TB structure for one SSRI group volunteer and the gender-BMI-matched healthy control volunteer in Figure 28. Quantitative results show that the SSRI group, on average, had 16.8% lower SW_{TS}, 13.5%

lower SCR_{TS}, and 1% lower $BMDl_{TS}$ as compared to the gender-BMI-matched healthy controls. Results of paired t-tests showed the differences were statistically significant ($p<0.0001$ for SW_{TS}, $p<0.05$ for SCR_{TS} and $BMDl_{TS}$). This study demonstrates the ability of the technique to differentiate between healthy and degenerative bone from images at *in vivo* resolution. Particularly, SSRI treatment affected SW_{TS} and SCR_{TS} to a greater extent by than $vBMD$ indicating that TB structure properties are more greatly affected than changes in bone mass. Coupled with the increased predictive value of SW_{TS} and SCR_{TS} with respect to yield stress as compared to $vBMD$, it may be that SSRI treatment affects bone fracture risk to a greater extent than traditional, bone mass centered techniques would suggest.

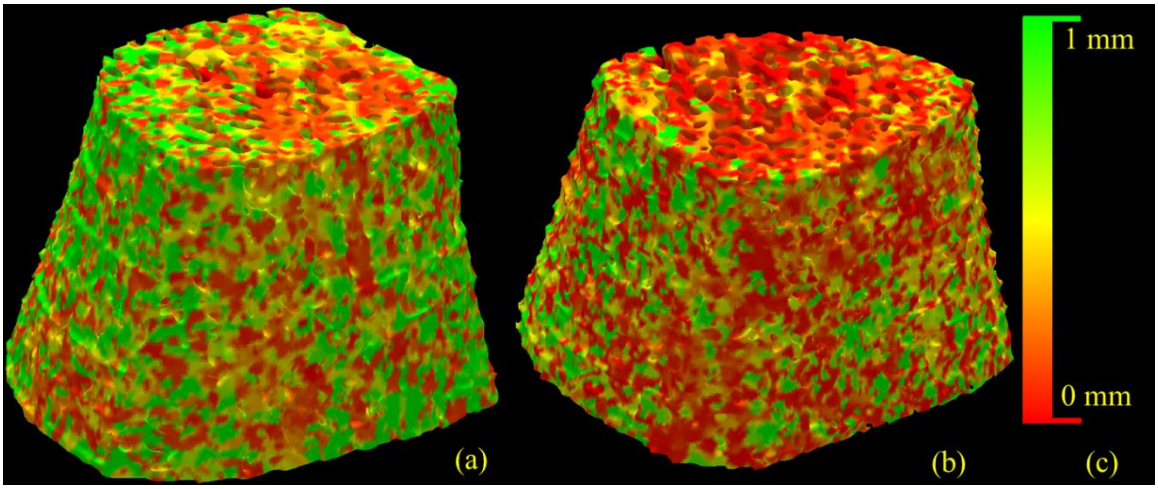

Figure 28 Same as Figure 27, but comparison between an age-sex-BMI-similar SSRI patient and a non-athlete: (a) health volunteer and (b) SSRI patient

3.5 Conclusion

An improved 3-D t-scale algorithm for fuzzy digital objects was presented. Results of a comprehensive study on computer-generated phantoms and fifteen cadaveric ankle specimens evaluating the new method were presented. Observed results demonstrated encouraging accuracy and stability of computed t-scale measures under

large different resolutions and different imaging modalities. Also, high repeat MD-CT scan reproducibility of the new t-scale computation method was observed in the cadaveric ankle study. T-scale computed plate-width and surface to curve ratio measures demonstrated higher ability to predict trabecular bone's experimental mechanical properties under *in vivo* conditions as compared to bone mineral density and previous proposed VTA methods. Currently, we are investigating the power of the new method to characterize clinical groups in terms of their bone health. Also, *in vivo* data from forty age similar and BMI order matched male and female volunteers demonstrated that males have significantly wider trabecular bone width, higher surface to curve ratio. By comparing the patient group using SSRI treatment with gender-BMI-matched healthy controls, we found that the patient group using SSRI treatment have significant narrower trabecular bone width, lower surface to curve ratio and lower longitudual bone mineral density.

CHAPTER 4. TRABECULAR BONE THRESHOLDING

In this chapter, we will introduce the thresholding of TB structure in CT imaging. The segmentation techniques for medical imaging are now pretty mature and there are a lot of existing advanced segmentation algorithms existing. As mentioned above, for our study, most images are in CT modality: MD-CT and μ-CT imaging. There are two big advantages from analyzing bone structure in CT images: 1) the bone structures have the highest intensity range in CT images, and 2) the intensity values for different tissues are highly reproducible. Based on those two observations, thresholding is utilized as the main algorithm for segmentation and the results are shown to be reliable. Here, we developed a new thresholding method combining class uncertainty and gradient information which would give accurate threshold for segmentation.

Novel research works in the current as presented in this chapter:

1) Development of a new thresholding method combining class uncertainty and gradient information.
2) Formulation of a new energy function to form a 2-D surface with intensity and gradient information.
3) Introduction of the novel intrinsic basin.

Automatic selection of a robust and accurate threshold parameter has remained a challenge in image segmentation. Over the past five decades, many automatic threshold selection methods have been reported in the literature. [154, 155, 158, 188-205] late 80's, Sahoo *et al*. [203] published a survey of optimum thresholding methods, while Lee *et al*. [204] reported results of a comparative study of several thresholding methods. Glasbey [205] published results of another comparative study involving eleven histogram-based thresholding algorithms. A relatively recent survey of thresholding algorithms for change detection in a surveillance environment has been presented by Rosin and Ioannidis. [158] Among early works on automatic thresholding, Prewitt and Mendelson [201] suggested

using valleys in a histogram, while Doyle [202] advocated the choice of median. Otsu [188] developed a thresholding method maximizing between-class variance. Tsai [191] proposed a choice of threshold at which resulting binary images have identical first three moments where the ith moment is defined by the sum of pixel intensity values raised to the ith power. Later works on thresholding methods have utilized entropy of original and thresholded images to construct an optimization criterion. For example, Pun [192] maximized the upper bound of posterior entropy of histogram. Wong and Sahoo's method [193] selects optimum threshold that maximizes posterior entropy subjected to certain inequality constraints characterizing the uniformity and shape of segmented regions. Pal and Pal [194] utilized the joint probability distribution of neighboring pixels which they further modified [195] using a new definition of entropy. Kapur *et al*. [196] proposed a thresholding method by maximizing the sum of entropies of segmented regions and a similar method was reported by Abutaleb [197] that maximizes 2D entropy. The method by Brink [198] maximizes the sum of entropies computed from two autocorrelation functions of thresholded image histograms. Li and Lee's method [154] minimizes relative cross entropy or Kullback-Leibler distance between original and thresholded images. Kitler and Illingworth [155] developed a thresholding method by minimizing segmentation errors defined from an information-theoretic perspective, while Dunn *et al*. [199] used a uniform error criterion. Leung and Lam [200] developed a method that maximizes segmented image information derived using an information-theoretic approach and demonstrated that their method is better than the methods based on minimum and uniform errors. [155, 199]

Although, Wong and Sahoo, [193] and Pal and Pal [194, 195] incorporated some spatial image information to their methods, others are mostly histogram-based techniques. One common shortcoming of a purely histogram-based approach is that it fails to utilize a significant amount of information embedded in image features formed by spatial arrangements of intensity values. Often, it is not possible for a human observer to select a

threshold in an image just from its histogram without seeing the original image. On the other hand, the image may contain clear partitions of different objects or tissue regions and it may only be a trivial task to select the threshold from the image. This observation inspired us to develop a method that directly makes use of impressions created on the image by different object interfaces. Class uncertainty is byproduct information of object classification and it's often ignored in the context of computer vision and imaging applications. In our previous work, it was demonstrated that high class uncertainty, commonly associated with intermediate intensity values between two object classes, appears at the vicinity of object or tissue interfaces in an image. This observation provides a unique theory relating histogram-based information with image-derived features. A new energy formulation is designed as a function of both intensity and gradient parameters and new algorithms are developed to automatically detect optimum pairs of threshold and gradient parameters on the energy surface for different tissue interfaces.

4.1 Class Uncertainty

Here we define class uncertainty based on priors possiblility and describe its relation with the gradient feature derived from spatial distribution of image intensity values. Let us consider a simple example of Figure 29 containing an object and a background region with their prior intensity distributions. Image points with intensity value of either t_1 or t_2 will be classified as object points; however, the class-uncertainty values for these two cases are significantly different. Specifically, points with intensity value t_1 should possess significantly high class-uncertainty as compared to those points with intensity value t_2. The relationship between class-uncertainty and image features may be better understood with the help of a real image. Figure 30 illustrates the idea on an image slice from a lower abdominal CT slice. The image depicts several regions, including fat/skin, bladder, muscles and bone which are partially separable using

intensity thresholding. Three threshold values are manually picked on the intensity histogram (Figure 30(b)) of the CT image slice (Figure 30(a)) among which two thresholds, namely th_1 and th_2, separate meaningful tissue regions (Figure 30(c,e)), while th_3 is intentionally selected as a bad threshold not representing any meaningful tissue region (Figure 30(g)). It should be noted that class-uncertainty images corresponding to thresholds th_1 and th_2 trace respective tissue boundaries (Figure 30(d,f)), while that for the wrong threshold th_3 doesn't and the uncertainty image shows high values all over the homogeneous region (Figure 30(h)).

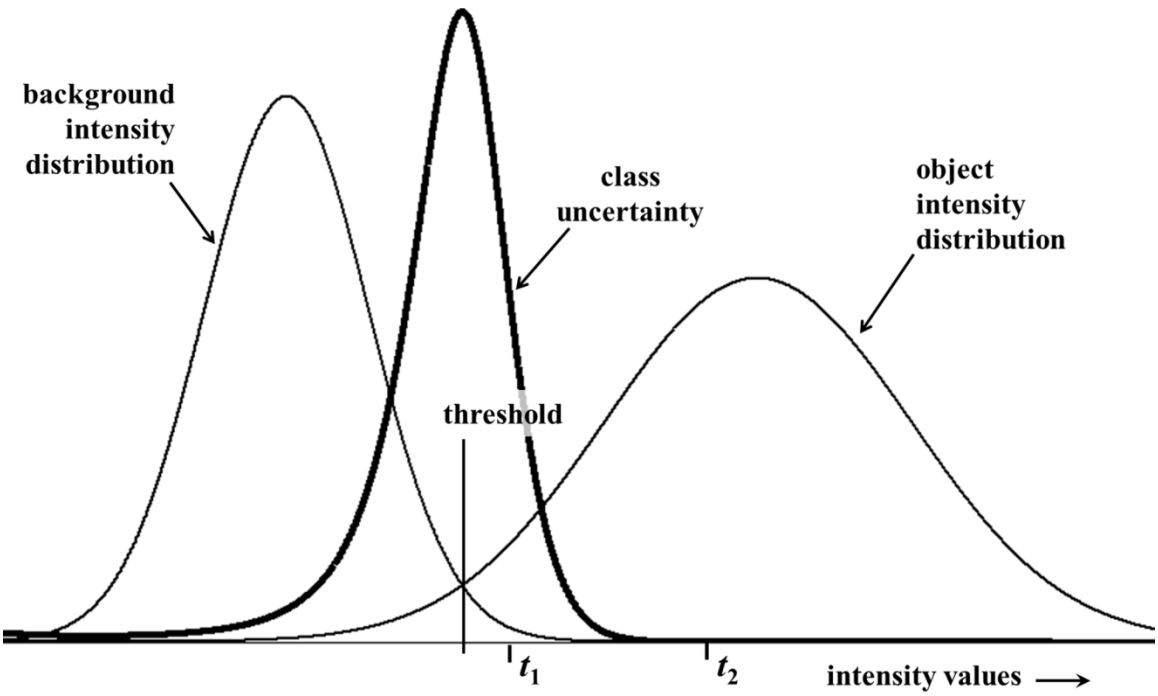

Figure 29 An illustration of the relationship between prior class distributions and class uncertainty for a two class problem. It should be noted that class uncertainty is maximum around the threshold selected under minimum-error criterion. Image points with intensity values of either t_1 or t_2 are classified as object points. However, the class-uncertainty associated with points having intensity t_1 is significantly higher than that for points with intensity t_2.

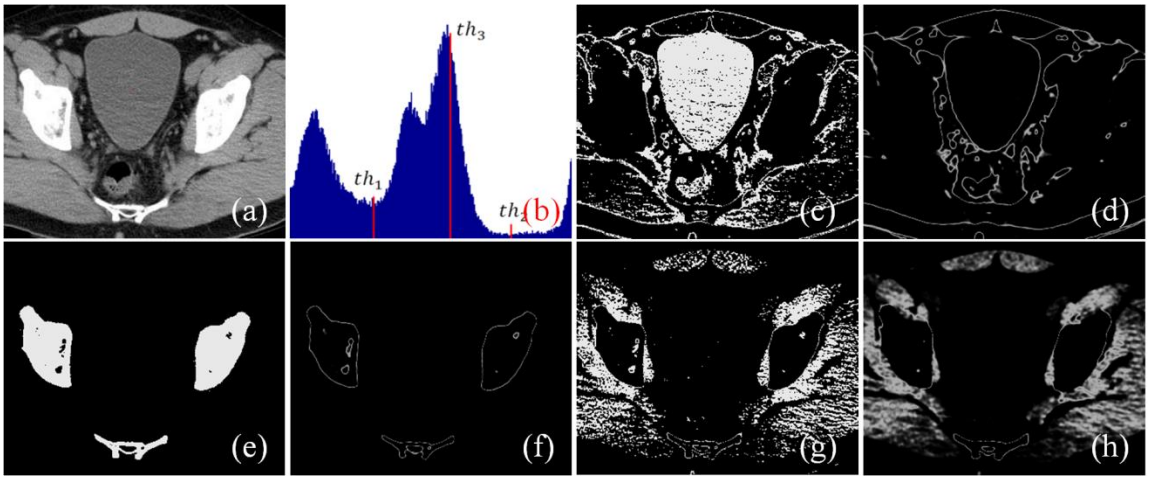

Figure 30 An illustration of the relationship between class uncertainty and tissue interfaces under different conditions of thresholding. (a) An image slice from a CT data of a patient's lower abdomen. (b) Image intensity histogram for (a) with three thresholds marked as th_1, th_2 and th_3. The first two thresholds are manually selected to segment proper tissue regions while the third one is intentionally picked as a bad threshold. (c,d) Thresholded tissue regions and class uncertainty image for the threshold th_1. (e,f), (g,h) Same as (c,d) but for thresholds th_2 and th_3, respectively. Note that class-uncertainty images in (d) and (f) depict respective tissue boundaries while the same in (h) fails to indicate any tissue interface and spills out into the entire soft tissue region.

An important observation in the above example is that, when proper thresholds are selected to separate different tissue regions, corresponding class-uncertainty maps depict interfaces among respective regions. On the other hand, when a visually incorrect threshold is selected, the class-uncertainty map no longer describes a region boundary. This correlation between the two independently defined features lays the theoretical foundation for our method, which is stated in the following postulate [206].

Postulate 1 In an image with fuzzy boundaries, under optimum partitioning of object classes, intensities with high class-uncertainty appear around object boundaries.

Although it is difficult to prove or disprove the postulate because of its nature, its validity can be justified on images as demonstrated in Figure 30 and the other experimental results presented in this chapter.

Here, we formulate the mathematical expression for class-uncertainty from priors using Bayes' rule [207] and Shannon and Weaver's entropy equation [208]. An image can be described by its intensity function $f: \mathbb{Z}^n \longrightarrow \mathbb{R}$, where $\mathbb{Z}$ denotes the set of integers and $\mathbb{R}$ denotes the set of real numbers. In most acquired digital images, intensity values are readily available at points with integral coordinates which are called a "pixel" in two-dimension (2D) and a "voxel" in three-dimension (3D); we denote the set of all pixels or voxels in an image as C. Let $F_O \subset C$ and $F_B \subset C$ represent the hypothetical true object and background regions, respectively, in an image. Let $p_A(g)|A = O$ or B denote the prior probability distribution for object/background region defined as follows:

$$p_A(g) = P(f(\mathbf{p}) = g|\mathbf{p} \in F_A)$$

Equation 16

where P represents "probability", $\mathbf{p}$ denotes an image point and g is a given intensity value. Let θ denote the density for object points so that $1 - \theta$ is the density for background points. Therefore, the probability of any point $\mathbf{p}$ having intensity value g, denoted by $p(g)$, may be expressed as follows:

$$p(g) = \theta p_O(g) + (1 - \theta) p_B(g)$$

Equation 17

Using the above priors, the posterior probabilities are defined by Bayes' rule, i.e.,

$$P(\mathbf{p} \in F_O|f(\mathbf{p}) = g) = \frac{\theta p_O(g)}{p(g)}$$

Equation 18

$$P(\mathbf{p} \in F_B|f(\mathbf{p}) = g) = \frac{(1 - \theta) p_B(g)}{p(g)}$$

Equation 19

Finally, the class-uncertainty measure [206] $h: \Re \rightarrow [0,1]$ at a point $\mathbf{p}$ with intensity value g is defined as the entropy of the above two posterior probabilities which is defined by the Shannon and Weaver's entropy equation [208], as follows:

$$h(g) = -\frac{\theta p_O(g)}{p(g)}\log\frac{\theta p_O(g)}{p(g)} - \frac{(1-\theta)p_B(g)}{p(g)}\log\frac{(1-\theta)p_B(g)}{p(g)}$$

Equation 20

Here, the idea is to model the prior probability distributions p_O and p_B and the density parameter θ as a function of the selected threshold t and the gradient parameter σ. Thus, the class-uncertainty map of an image varies as a function of threshold t and gradient parameter σ; we use $h_{t,\sigma}(g)$ to denote the threshold and gradient-dependent class-uncertainty function.

It's not difficult to find out from Equation (4) that the class uncertainty measure always lies in the normalized scale of [0, 1]. On the other hand, image gradient is measured in the image intensity scale. Therefore, a meaningful formulation of the energy function using Postulate 1 entails a normalized measure for image gradient values. To overcome this issue, a gradient parameter σ is introduced, which needs to be optimized and, quite possibly, the parameter may not remain constant for different tissue interfaces. Many models can be adopted to normalize the gradient measure; here a Gaussian model is used to compute a normalized measure ∇_σ of intensity gradients using the control parameter σ as follows:

$$\nabla_\sigma(\mathbf{p}) = 1 - e^{-\frac{(\nabla(\mathbf{p}))^2}{2\sigma^2}}$$

Equation 21

where ∇ is an intensity-gradient operator and ∇_σ is a normalized gradient parameter. Using these two normalized measures of class uncertainty and image gradient, the energy function E is formulated as follows:

$$E(t,\sigma) = \sum_{\mathbf{p}\in C}\left[h_{t,\sigma}(f(\mathbf{p})) \times \left(1-\nabla_\sigma(\mathbf{p})\right) + \left(1-h_{t,\sigma}(f(\mathbf{p}))\right) \times \nabla_\sigma(\mathbf{p})\right]$$

Equation 22

Following the above equation, each point **p** contributes a large amount of energy if it falls in any of the following two categories – (1) class uncertainty is high and

gradient is low, or (2) class-uncertainty is low and gradient is high. It should be noted that each of these two situations is a contradiction to Postulate 1. To some extent, the energy function E is formulated as an aggregate measure of contradictions to Postulate 1 over the entire image. On the other hand, if a pixel **p** has both high class uncertainty and high gradient or low value for both measures, it's in agreement with Postulate 1 and only contributes a small amount of energy. It should be noted that, under any of these two conditions, each of the two components on the right hand side of Equation 22 takes a small value (close to '0') due to the multiplication between a high (close to '1') and a low (close to '0') value, therefore, the sum of the two components is always a small value.

4.2 Optimum Threshold Selection

In the previous chapter, we have formulated an energy function E that captures the correlation between image gradient and class uncertainty as guided by Postulate 1. Specifically, the energy function is formulated as an aggregate measure of contradictions to Postulate 1 by all points in an image and is expressed as a function of threshold and gradient parameters t and σ, respectively. Thus, the energy function E essentially forms an energy surface over the parametric space of t and σ and an optimum choice of threshold and gradient parameters representing an object interface can be found by identifying a meaningful depression on the energy surface.

Because the search space is only two-dimensional over a limited range of values for t and σ, we adopt an exhaustive search technique. Therefore, the most critical factor here is to define the geometry of optimum locations on the energy surface. For the threshold parameter t, the entire intensity range $[I_{MIN}, I_{MAX}]$ is used for searching optimum locations. On the other hand, search-space for the gradient parameter σ is limited to $[1\% \times (I_{MAX} - I_{MIN}), 40\% \times (I_{MAX} - I_{MIN})]$; we stay away from the extreme values of σ to reduce computation burden and also, to avoid computational instability. We determine two types of optimum locations on the energy surface – a Type I optimum

location forms a meaningful or valid pit on the energy surface E while a Type II optimum location forms a meaningful valley on E. Let E_{σ_0} denote the energy function for a given value σ_0 of the gradient parameter and thus, only the threshold parameter is varied. Therefore, E_{σ_0} forms an energy curve for the gradient parameter value σ_0. A local minimum on the energy surface E is referred to as a pit while a local minimum on an energy line E_{σ_0} is referred to as a valley point. Depending upon the resolution of the search-space, both E and E_{σ_0} can contain a large number of noisy local minima. Here, we use the idea of intrinsic basin, an idea similar to catchment basins used in watershed segmentation methods [209, 210], to distinguish between noisy and meaningful local minima. Let (t_1, σ_1) denote the parameter values at a pit, i.e., a local minimum on the energy surface E. The intrinsic basin of (t_1, σ_1), denoted by $B(t_1, \sigma_1)$, is the set of all locations (t, σ) such that there exists a path from (t, σ) to (t_1, σ_1) with all points on the path having energy values greater than or equal to $E(t_1, \sigma_1)$. Essentially, $B(t_1, \sigma_1)$ corresponds to the region on E that can be flooded by pouring water from top at $E(t_1, \sigma_1)$ without water leaking to a location with energy value less than $E(t_1, \sigma_1)$. An intrinsic basin $B_{\sigma_1}(t)$ for a valley point (t_1, σ_1), i.e., a local minimum on the energy curve E_{σ_1} is defined similarly. The idea of intrinsic basin on an energy line E_{σ_1} is illustrated in Figure 31. The black line in Figure 31 denotes the energy line over the entire intensity range $[I_{MIN}, I_{MAX}]$ and each local minimum on the line represents a valley point. Different colors are used to indicate different intrinsic basins; however, one intrinsic basin can include multiple colors. For example, the intrinsic basin marked in blue on the right side of the figure can include the regions marked in yellow and cyan, along with the two small regions marked in red. The depth of a basin is defined as the height of its topmost layer with respect to its bottom. A pit (or, a valley point) is considered as a valid pit (respectively, a valid valley point) if the height of its intrinsic basin covers at least 3% of the maximum variation in the energy surface E (respectively, the energy line E_σ). The maximum variation for the energy curve E_σ, illustrated in Figure 31, is the depth of the

grey basin. Depths of basins marked in red are less than 3% of the maximum variation, thus fail to quality as valid valleys; all other basins in Figure 31 qualify as valid valleys. The choice of the parameter value of 3% for validity check was selected as it was experimentally observed that the height of intrinsic basins for noisy points were small and was always less than 1%. Therefore, the parameter value of 3% ensures exclusion of all noisy points.

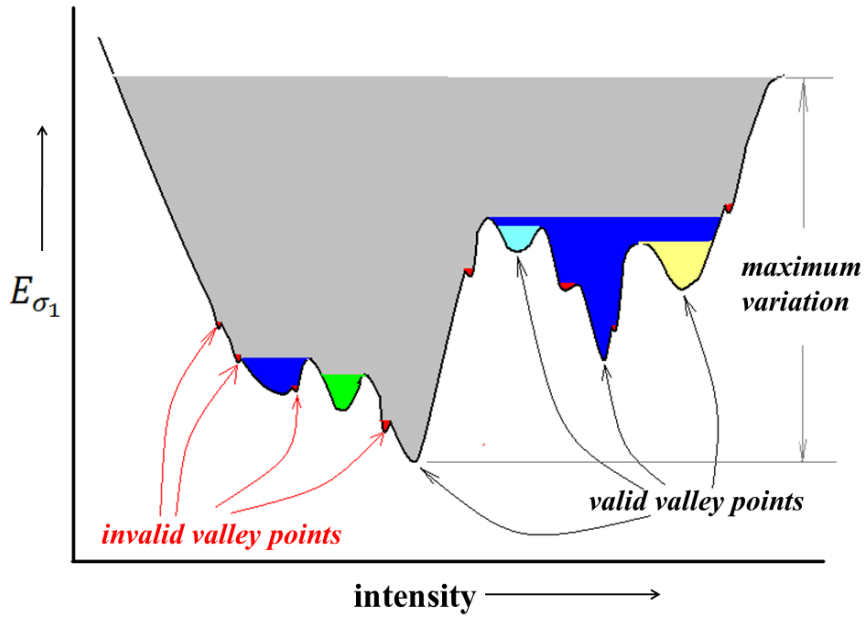

Figure 31 An illustration of intrinsic basins on an energy line E_{σ_1}. Different colors are used to indicate different intrinsic basins; however, one intrinsic basin may include multiple colors. For example, the intrinsic basin marked in blue on the right side includes all the regions marked in yellow and cyan along with the two small regions marked in red. All invalid valley points are marked red and others represent valid valley points.

In our experiments, both energy surfaces and curves are mostly found to be smooth functions, except for tiny fluctuations, especially over flat regions. The primary objective of adding a validity constraint on pits and valley points using intrinsic basins is to avoid such small fluctuations, while capturing all meaningful local minima. Each valid pit is considered as a Type I optimum location for threshold and gradient parameters. A

meaningful valley is defined as an 8-connected path [37, 174] of valid valley points for contiguous values of the gradient parameter. Finally, a Type II optimum point is defined at the center of a meaningful valley containing no pit or Type I optimum location.

An example of the energy surface/function and detected optimal locations are illustrated in Figure 32. For the current example, three valley lines, marked as red lines, were identified on the energy surface, among which two were associated with pits or Type I optimal locations (hollow black circle), while one valley had no pit on it. For the valley with no pit, a Type II optimal location (hollow red circle) was detected, following the algorithm described the above.

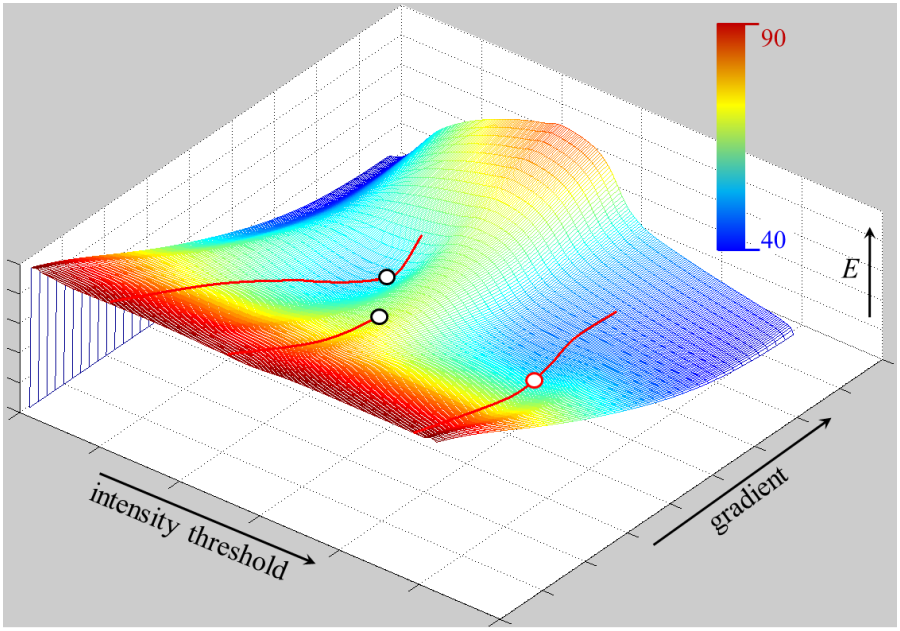

Figure 32 An illustration of different types of optimum locations on an energy surface/function. The energy function is rendered using a 3D MATLAB display function, with color indicating the energy value (red: high, blue: low). Here, valley lines are shown in red; Type I (pit) and II optimum locations on the energy surface are denoted by hollow black and hollow red circles, respectively.

4.3 Experimental Plan and Results

To examine the effectiveness of the proposed thresholding algorithm, it was compared with Otsu's method [188] and several other popular thresholding methods [198, 200, 206]. Although, the thresholding method by Otsu was proposed three decades ago, it has become quite popular because of its classical theoretical foundation. Recently, the method has been implemented within the ITK library [211] and has been used in several medical imaging [212-217] and other applications [218-221]. Essentially, the method is based on minimization of the class density weighted within-class variance which is also equivalent to maximization of between-class variance. A limitation of Otsu's method is that it requires that the number of tissue regions must be specified. In our experimental setup we used Otsu's method with the correct number of tissue regions specified by users. On the other hand, for the proposed method, this number is detected automatically by the algorithm. Also, we have compared the performance of the new method with the minimum error (ME) [155] and maximum segmented image information (MSII) [200] thresholding algorithms along with our previously published minimization of homogeneity- and uncertainty-based energy (MHUE) thresholding algorithm [206]. The principle of ME thresholding algorithm is to find the threshold that gives minimum classification error defined as follows. For a given threshold, an image is partitioned into two regions and the normal distribution of intensity values within each partition is determined. The classification error is determined as the average fraction of the normal intensity distribution of one partition falling inside the intensity range of the other. The principle of the MSII thresholding algorithm is based on maximization of segmented image information defined as the difference between initial scene uncertainty, computed from the original image, and residual uncertainty computed from the thresholded image. In the MHUE [206] thresholding algorithm, the class uncertainty theory is combined with a rank-based normalized measure of region homogeneity to formulate the criterion of threshold optimization.

Experiments were designed to evaluate both the accuracy and reproducibility of the new method and to compare with the other methods: 1) the accuracy of a method was computed by comparing its results with manual thresholding except for phantom data where truths were known. 2) The reproducibility was computed using repeat scan MD-CT data of cadaveric ankle specimens. In order to reduce subjectivity artifacts by individuals for accuracy analyses on clinical data, the mean of threshold values selected by three independent users for a given interface was used as truth. Toward defining an error measure between a computer-selected threshold s and a true threshold t, an important observation made was that pixel/voxel density is non-uniform over the intensity range. Therefore, a straight-forward difference between s and t may not be a good choice for error measure. Let $H: [I_{MIN}, I_{MAX}] \rightarrow \mathbb{Z}^+$, where $\mathbb{Z}^+$ is the set of positive integers, denote the image intensity histogram function. The value of $H(i)$ denotes the pixel/voxel density at the intensity value i. We use the following error function which essentially represents the pixel/voxel density weighted distance between s and t in the normalized scale of [0,1] defined as follows:

$$Error(s,t) = \frac{\sum_{i=s}^{t} H(i)}{\sum_{i=I_{MIN}}^{I_{MAX}} H(i)}$$

Equation 23

where $H(i)$ represents the intensity histogram of the test image. The idea of the above error measure is graphically illustrated in Figure 33. When there are multiple true thresholds t_1, t_2, t_3, … and computed thresholds s_1, s_2, s_3, … for different object regions, for each true threshold t_i, the closest computed threshold s_j is used for estimating the error. In the following, we describe different image data sets used in our experiments.

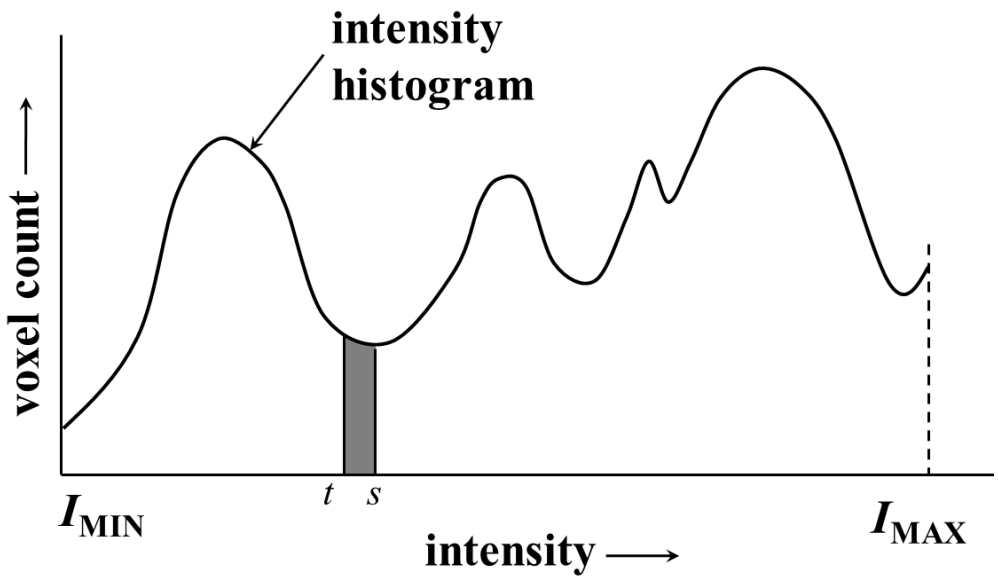

Figure 33 A graphical illustration of the error measure between a selected threshold s and the true threshold t. Essentially, it computes the pixel/voxel density weighted distance (the area of the grey region) between the two thresholds and normalized by image size, i.e., the total area under the histogram.

CT image of cadaveric ankle specimens: Four cadaveric ankle specimens were scanned in a Siemens Sensation 64 Multi-slice CT scanner at 120 kVp and 140 mAs and a pitch of 0.8 to adequately visualize the bony structures. After scanning in a helical mode at a slice thickness of 0.6 mm and collimation of 12×0.6 mm, the image was reconstructed at 0.3 mm slice thickness with a normal cone beam method utilizing a very sharp kernel of U75u to achieve high image resolution. Image parameters for these scans were as follow: matrix size = 512×512 pixels; number of slices = 334 to 336 and pixel size = 152 μm. Each ankle specimen was scanned three times after repositioning on the table. This CT data set was used for both accuracy and reproducibility analysis.

4.3.1 Accuracy analysis

Results of application of the method on 3-D CT images are presented in Figure 34. The new method successfully detected three thresholds producing visually satisfactory

segmentation of four regions, namely background (black), fat/skin (red), muscle (green), and bone (white). Salt and pepper noise, especially over thresholded regions for fat/skin and muscle (Figure 34(d)), was caused primarily by low contrast-to-noise-ratio between the two regions which disappeared after applying a simple smoothing filter (Figure 34(e)). More interesting, the amount of noise on each of the two regions is more or less similar indicating that the method selected the threshold nearly at the middle between mean intensities for the two regions. In Figure 34(b), the second threshold on the intensity histogram of the 3D image represents the threshold for the interface between the two regions which is located near the second pick of the histogram. Just by looking at the histogram, it's almost impossible to select this threshold. On the other hand, the two regions, therefore, the interface threshold is clearly visible in the image which allowed our algorithm to automatically detect the threshold. As shown in Figure 34(c), each of the first two thresholds led to pits (Type I optimum locations), while the third threshold produced only a valley (Type II optimum location). The class uncertainty image at different thresholds successfully depicts different interfaces with different colors. Otsu's method has failed to produce visually satisfactory results for this example. Also, ME and MSII thresholding methods have failed to find thresholds for all three tissue interfaces in these images, significantly increasing error measures. For this specific specimen, the MHUE has produced almost similar results (Figure 34(l)) as produced by the new algorithm.

For quantitative accuracy analysis, the gold standard threshold for each interface for each image was determined as the average of the thresholds selected using a graphical user interface by three independent users to reduce the effect of inter-user subjectivity errors. For a given CT image and a specific tissue interface, the threshold error by one method was determined from the true threshold and the closest computed threshold according to the error definition presented in Chapter 4.3. Finally, for a given image, the threshold error was computed as the sum of errors over all interfaces. Image threshold

errors for twelve images by the five methods are illustrated in Figure 35. Also, the standard deviation of threshold errors for different interfaces in an image is indicated in the figure. The new method has clearly outperformed the ME and MSII thresholding methods. Average image threshold errors by Otsu's and MHUE methods are 20.78% and 8.57%, respectively, while that by the new method is only 2.75% indicating a great reduction as compared to Otsu's and MHUE methods, respectively. Also, the standard deviation of threshold errors for different tissue interfaces by the new method is relatively small for all images indicating the consistency of our method in selecting the threshold for different tissue interfaces. Average image threshold error was measured by adding errors from all interfaces. For example, each set of ankle CT data used here has three tissue interfaces; therefore, the average interface threshold error by our method should be 0.92% computed by dividing the total image threshold error of 2.75% by three. We performed a paired t-test of threshold errors by the new, the Otsu's and the MHUE methods using the error values for all three interfaces in all images. The average threshold errors for an interface by Otsu' s, MHUE and the new methods are 6.93%, 2.86% and 0.92%, respectively, and the null hypothesis was rejected with p-value < 0.001 for comparisons between the new and either of Otsu's or MHUE methods.

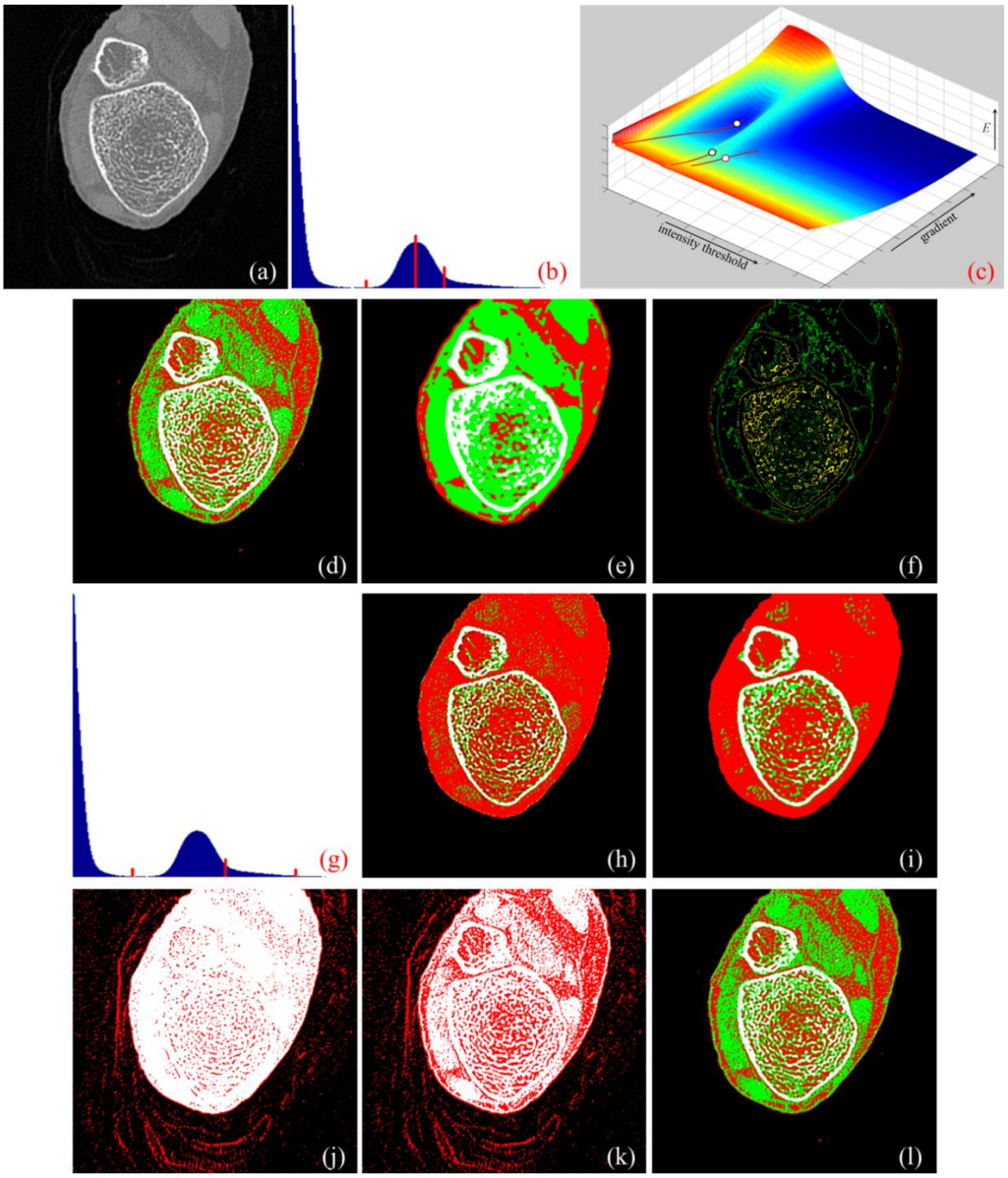

Figure 34 Results of application of different thresholding methods on a CT image slice of lower abdomen. (a) Original CT image slice. (b) Optimum thresholds (red lines). (c) The energy surface with valley lines (red) and optimum threshold and gradient parameters (hollow circles). (d) Thresholded regions in different colors as applied to the original image. (e) Same as (d), but applied to a smoothed image. (f) Object class uncertainty maps at different optimum thresholds. Note that the class uncertainty image highlights different tissue interfaces at different optimum thresholds. (g,h,i) Same as (b,d,e), respectively, but for Otsu's method. (j,k,l) Results of thresholding as obtained by the MSII, ME, MHUE algorithms, respectively.

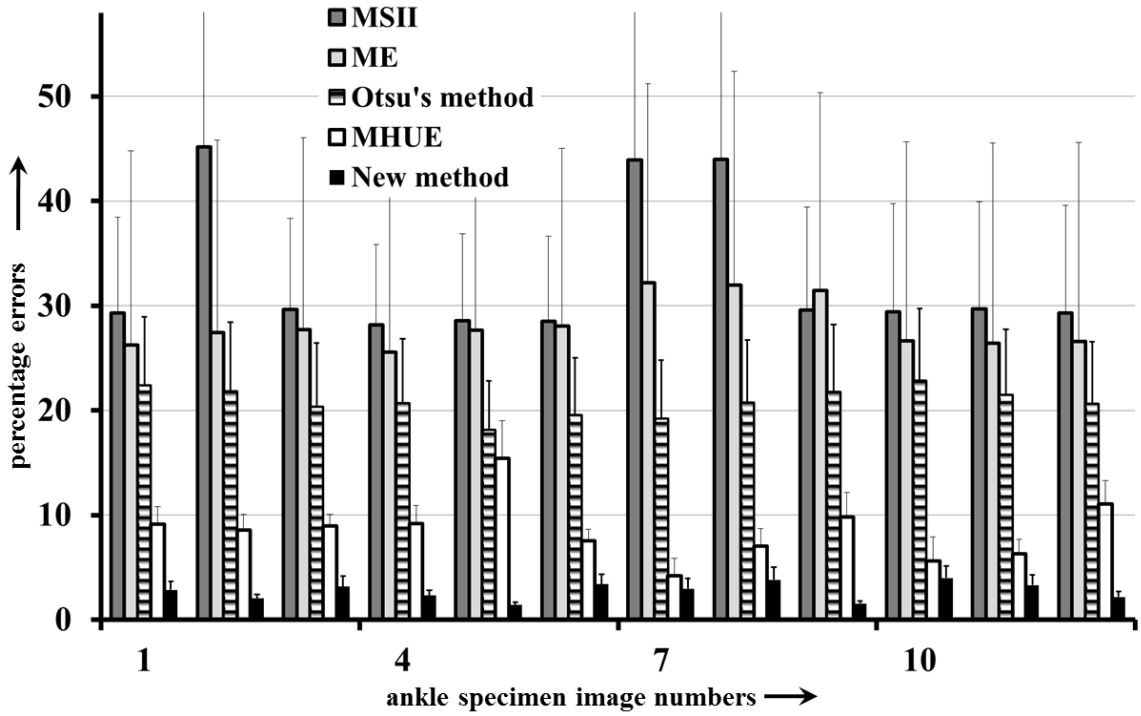

Figure 35 Results of quantitative analyses of image threshold errors by different methods. For each ankle CT image, indicated by a number between one and twelve on the horizontal axis, height of the bar indicates the percentage image threshold error. The line one each bar denotes the standard deviation (in percentage scale) of threshold errors for different interfaces of an image.

4.3.2 Reproducibility analysis

Data from three repeat CT scans of four cadaveric specimens were used for reproducibility analysis. We performed two reproducibility analyses as follows:

Experiment 1: For this experiment, repeat CT scans were used to examine the reproducibility of threshold values for different interfaces and specimens. From every CT image, we extracted three data values, each representing the threshold value for one of the three tissue interfaces (see Chapter 4.3.1). Thus, altogether there were twelve events, each representing the threshold for a specific interface in a given specimen (Figure 36 (a-c)). The threshold value computed from each repeat CT scan was considered as a repeat observation of the event; thus, there were three repeat observations. Results of this

experiment are presented in Figure 36(a-c), showing high repeat scan reproducibility for all three methods, except that the MHUE algorithm has underperformed for one specimen (specimen-interface number 5), where it missed the threshold for one tissue interface.

Experiment 2: The purpose of this experiment was to examine whether a method reproduce the same threshold for a specific tissue interface in different specimens. The argument behind this experiment is that, in CT images, intensity values for different tissues are highly reproducible [222] and therefore, different methods should produce similar thresholds for a specific interface in different specimens. For this experiment, we used the data from first CT scan for each of the four specimens. Here, threshold of a given tissue interface is considered as an event leading to three events for three interfaces. On the other hand, the threshold values of the specific tissue interface computed from different specimens are treated as repeat observations leading to four observations for each event. Results of this experiment for the new, Otsu's and MHUE methods are presented in Figure 36(d-f). ICC values for the three methods under this experiment are 0.999, 0.865 and 0.976, respectively. Similar results were found using images from other two scans.

Results of above two experiments show that all three methods successfully reproduce a threshold in repeat scans for a specific interface in a given specimen. However, Otsu's method has failed to guarantee high reproducibility of the threshold for a specific interface in different ankle specimens which is expected to be similar in CT images. The MHUE method is less robust in detecting all different tissue interfaces in images resulting reduced ICC values in both reproducibility experiments. The new method has shown high reproducibility under both experiments. In repeat CT scans of a given specimen, histograms are similar; on the other hand for different specimens, there were significant variations in histograms due to differences in tissue proportions. It explains the behavior of Otsu's method in above two experiments.

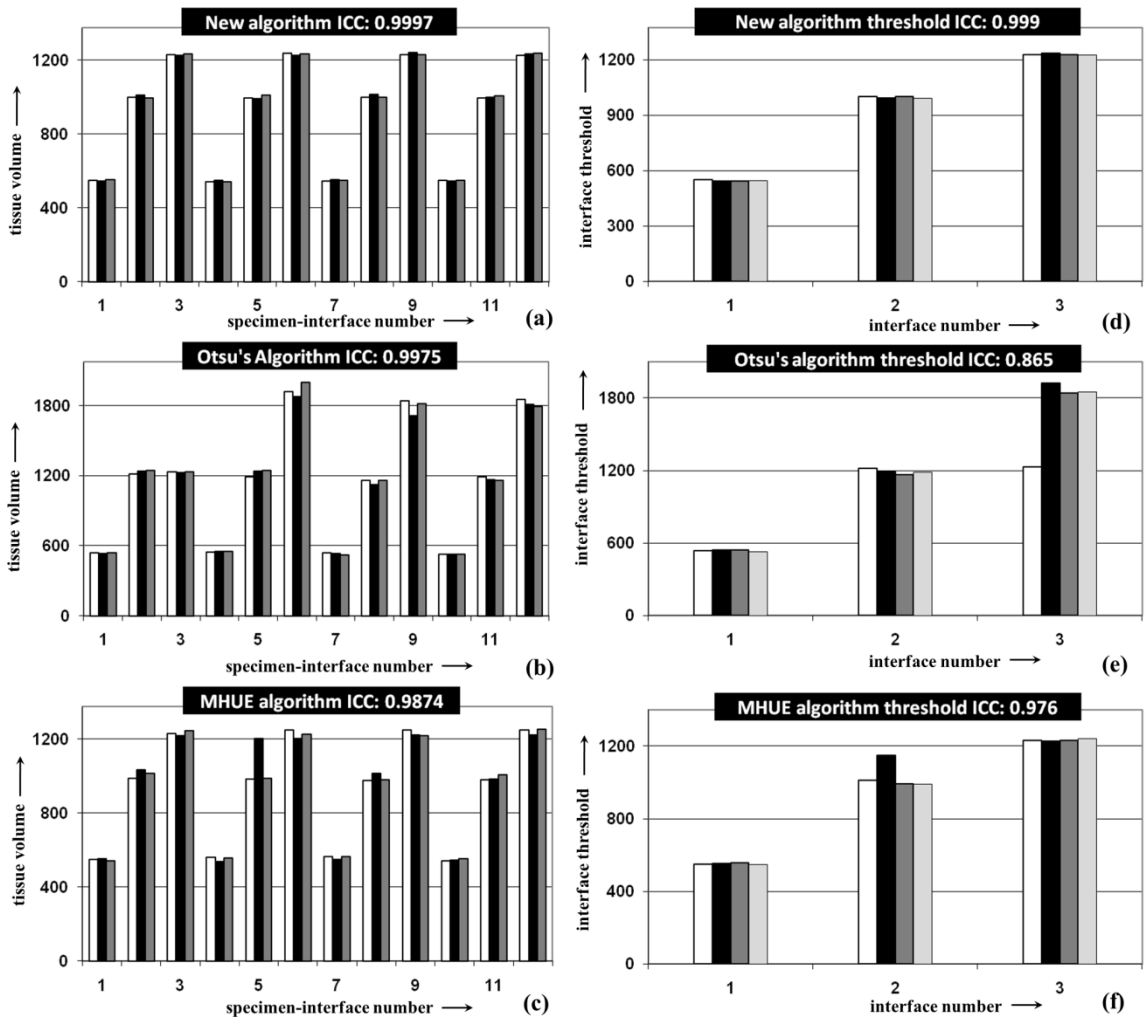

Figure 36 Results of reproducibility analysis and intra-class coefficient (ICC) of threshold values in repeat CT scans. (a) ICC for threshold values of different tissue interfaces of four specimens in three repeat scans using the new method. (b) Same as (a) but for Otsu's method. (c,d) Same as (a,b) but for ICC value of thresholds for matching interfaces in different specimens using the first CT scan.

4.4 Conclusion

In this chapter, we have presented a new method for simultaneously computing optimum values for thresholds and gradient parameters for different object interfaces. The method has been applied on several medical image data sets. For every example

presented here, the new method has successfully determined the number of object/tissue regions in the image and also detected visually satisfactory thresholds for different tissue interfaces even when some of the thresholds are almost impossible to locate in their histograms. Although, the method provides the optimum gradient parameter for each interface in an image, the accuracy and reproducibility of this parameter has not been examined in this chapter. The performance of the method has been compared with two types of methods – (1) methods with automatic detection of the number of object regions (ME, MSII, MHUE) and (2) methods with a pre-defined number of object regions (Otsu). Results of comparative experiments have shown that the new method significantly outperforms the other two methods (ME and MSII) under the first category. Results of comparison with Otsu's method has shown that, given the predefined number of object regions, Otsu's method produce visually similar results to our method where the thresholds are visible (e.g., a local plateau) on the histogram. However, Otsu's method being a purely histogram-based algorithm; it could fail to properly select a threshold when it is located near a local top on the histogram (Figure 34). On the other hand, our method effectively utilizes spatial information by combining the image gradient with class uncertainty. Therefore, although, the information on the histogram is not good enough to select the right threshold, the new method fills the gap by using spatial information. Further, one major advantage of the current method over Ostu's method is that the new method does not require any pre-defined number of object regions in an image which itself is a significant improvement. Even for the examples where Otsu's method produce results visually similar to the new method, quantitative analyses of accuracy and reproducibility have shown that the new method is superior to Otsu's method. As compared to the MHUE algorithm, the improvement in performance of the new algorithm is enhanced as higher levels of imaging artifacts by noise, intensity non-uniformity and resolution. Also, the MHUE algorithm was found less robust in detecting thresholds for all tissue interfaces.

CHAPTER 5. DISCUSSION AND FUTURE WORK

In this chapter, we will discuss the ultimate goal of this research work, the limitations of the current work, and possible future work based on the current results.

5.1 Ultimate Goal the Research

The ultimate goal of our current research is to establish a new group of criteria in early osteoporosis diagnosis using TB architectural measurements, including TB thickness, marrow spacing, plate/rod characterization and orientation, that can be used to effectively prevent osteoporotic fragility fracture.

A great deal of clinical research has been done regarding the relationship between the risk of fracture and osteoporosis [223-226]. Gay [226] led a study regarding 136 patients at an average of 10.6 years after distal radial fracture, discovered that 37.6% of the 109 women and 7.4% of the 27 men suffered a subsequent fracture. Sander *et al.* [225] conducted a coordinator program in post-fracture osteoporosis management as an analysis of the cost-effectiveness of the use of coordinator. Kanis [223] and WHO study group [224] led an assessment of fracture risk and screening for postmenopausal osteoporosis.

Besides the direct study, several studies regarding possible treatment of osteoporosis are conducted [227-229]. Meunier *et al.* [229] explored the effect of Strontium Ranelate on the risk of vertebral fracture in women with postmenopausal osteoporosis. Ettinger *et al.* [228] on the other hand evaluated the treatment of Raloxifene in a 3-year randomized clinical trial. Chesnut III *et al.* [227] led a study of the effects of oral Ibandronate administered daily or intermittently on fracture risk in postmenopausal osteoporosis. So far, all criteria for the research above are based on the examination of traditional BMD measurements.

The research we are doing now is to find more accurate and effective parameters in the diagnosis of osteoporosis, and thus it will enhance future research in the prevention of osteoporosis fracture, and eventually set as a part of the diagnosis criteria.

5.2 Limitation of the Current Research

Our current research gives two accurate, reproducible, robust and sensitive algorithms to predict TB strength using its architectural properties such as TB thickness, marrow spacing, plate/rod characterization and orientation. The experimental study using human cadaveric ankle specimens demostrated the accuracy, reproducibility, robustness and sensitivity in predicting TB strength. However, more work is needed especially on the clinical level, to determine the actual performance of our algorithm in osteoporosis diagnosis. Specifically, the current research is limited in following three aspects:

1. The current research is limited to the "peripheral site" (tibia), and does not include the "central site" (hip and spine) where most dangerous in osteoporosis related fracture and cost most.
2. The current research is still quite limited on the experiment level, the results are "statistically significant"; however, the algorithms needs more clinical level experiments to prove their "clinical significance".
3. The computation time for tensor scale is not short enough.

Regarding the first limitation, several groups have done research about the relationship between the bone quality comparison between peripheral site and central site or use the bone quality at peripheral site as the prediction for fracture risk [230]. Siris *et al* [230-234] conducted a research between 1997 and 1999 with over 200000 ambulatory postmenopausal white women aged 50 or older with no previous osteoporosis diagnosis. Almost half of the population had previously undetected low BMD, including 7% with osteoporosis, and the results showed that peripheral BMD results were highly predictive of fracture risk. Miller *et al.* [231] studied the association between BMD measurements at

peripheral sites and subsequent fracture risk at the hip, wrist/forearm, spine, and rib in 149,524 postmenopausal white women, without prior diagnosis of osteoporosis, and the results indicated that low BMD found by peripheral technologies, regardless of the site measured, was associated with at least a twofold increased risk of fracture within one year, even at skeletal sites other than the one measured. Crabtree *et al.* [232] studied the correlation between intracapsular hip fracture and peripheral quantitative computed tomography, showing the quality of this peripheral site bone would improve the detection of those at risk of hip fracture. Picard *et al.* [233] studied the ability of peripheral DXA measurement to diagnose osteoporosis as assessed by central DXA measurement, and the result indicated that a peripheral measurement of BMD, together with a good clinical evaluation of the osteoporosis risk profile of the patient, can be an useful tool for the diagnosis of osteoporosis in areas where central DXA is not available. Miller *et al.* [234] conducted a study about patients who may need additional central bone density measurements besides the peripheral site bone measurements.

Regarding the second limitation, the results of a study can be statistically significant but still be too small to be of any practical value. This is of great importance to physicians when looking at research evidence. Various quantitative measures are used to decide whether a treatment effect is large enough to make a difference to a patient or doctor. In our study, how much improvement with the new measurement can make the diagnosis of osteoporosis clinically significant? To answer this question, we would need more practical experiments with real clinical MD-CT imaging data to determine whether the measurements can be clinical significant in diagnosis of osteoporosis. However, so far this is beyond the work of current Ph.D. study.

As to the last limit which is a technical problem, the main time consuming part in the current tensor scale computation is the ellipsoid-fitting step. Although it has been improved, and only the axial points are computed in 3-D, it still needs about 40 minutes to compute a typical tibia TB patient data set, which can be improve in the later study.

5.3 Possible Future Research Work

As mentioned in the previous section, the experiments and results of the current study only show that the research work is statistically significant, and it is necessary to have more clinical experiments to determine the clinical significance of the our algorithms. Once the algorithm is proved to be clinical significant, it would be necessary to establish a further clinical study as clinical trial to achieve the ultimate goal of the research mentioned in Section 5.1.

Go back to the final goal of our research that we want to establish a new diagnoses standard for osteoporosis and osteopenia, instead of the current using BMD Z-score. To achieve the goal, the most important step is to establish the correlation between the TB architectural measurements and the risk of osteoporosis fracture. This can be divided into three steps:

1. Build the correlation between peripheral site measures with the central site measures. There are three main sites that are vulnerable for osteoporotic fracture: hip, spine and wrist. The problem is that the three sites are different from each other. The current research is focused on the tibia site, which is the not one of the three, so it will be necessary to build the correlations.
2. Utilize the correlation between the BMD measures and the risk of osteoporotic fracture to find the correlation between architectural measures and the risk of osteoporotic fracture. A simple solution for initial research is that use the subjects with both tibia scans and whole body DXA, compare the architectural measures with the DXA derived BMD measure of the legs.
3. Conduct clinical experiments to find the correlation between TB architectural measures and the osteoporotic fracture directly. Here, we need to take care of the age effect in bone loss. And also, it will be necessary to do some experiments will different drugs or calcium.

The last, we will talk about the improvement in the algorithm level. As mentioned in the previous section, the computation time for tensor scale is still a limitation for real clinical activity. Mainly improvements in two directions can be explored in the further research.

1. Rebuild a new tensor scale computation algorithm, such as proposed and implemented by Xu [184], even though it suffers accuracy problem in the current TB measurement study.
2. Conduct more clinical level experiments to find a proper trade-off point between the computation efficiency and the accuracy in predicting TB strength and thus osteoporosis diagnosis. And this work requires more collaboration between our group and clinical doctors.

REFERENCES

[1] J. Wolff, *Das Gesetz der Transformation der Knochen*. Berlin: A. Hirschwald, 1892.

[2] S. Boonen and A. J. Singer, "Osteoporosis management: impact of fracture type on cost and quality of life in patients at risk for fracture I," *Curr Med Res Opin,* vol. 24, pp. 1781-8, Jun 2008.

[3] L. J. Melton, 3rd, "Epidemiology of spinal osteoporosis," *Spine,* vol. 22, pp. 2S-11S, Dec 15 1997.

[4] F. W. Wehrli, P. K. Saha, B. R. Gomberg, H. K. Song, P. J. Snyder, M. Benito, A. Wright, and R. Weening, "Role of magnetic resonance for assessing structure and function of trabecular bone," *Topics in Magnetic Resonance Imaging,* vol. 13, pp. 335-356, 2002.

[5] P. Ammann and R. Rizzoli, "Bone strength and its determinants," *Osteoporos Int,* vol. 14 Suppl 3, pp. S13-8, 2003.

[6] R. D. Chapurlat and P. D. Delmas, "Bone microdamage: a clinical perspective," *Osteoporos Int,* vol. 20, pp. 1299-308, Aug 2009.

[7] E. Seeman and P. D. Delmas, "Bone quality--the material and structural basis of bone strength and fragility," *N Engl J Med,* vol. 354, pp. 2250-61, May 25 2006.

[8] E. Legrand, D. Chappard, C. Pascaretti, M. Duquenne, S. Krebs, V. Rohmer, M. F. Basle, and M. Audran, "Trabecular bone microarchitecture, bone mineral density and vertebral fractures in male osteoporosis," *Journal of Bone and Mineral Research,* vol. 15, pp. 13-19, 2000.

[9] L. Mosekilde, "Consequences of the remodelling process for vertebral trabecular bone structure: a scanning electron microscopy study (uncoupling of unloaded structures)," *Bone and Mineral,* vol. 10, pp. 13-35, 1990.

[10] N. Boutry, B. Cortet, P. Dubois, X. Marchandise, and A. Cotten, "Trabecular bone structure of the calcaneus: preliminary in vivo MR imaging assessment in men with osteoporosis," *Radiology,* vol. 227, pp. 708-17, Jun 2003.

[11] M. Benito, B. Gomberg, F. W. Wehrli, R. H. Weening, B. Zemel, A. C. Wright, H. K. Song, A. Cucchiara, and P. J. Snyder, "Deterioration of trabecular architecture in hypogonadal men," *J Clin Endocrinol Metab,* vol. 88, pp. 1497-502, Apr 2003.

[12] C. H. Chesnut, 3rd, S. Majumdar, D. C. Newitt, A. Shields, J. Van Pelt, E. Laschansky, M. Azria, A. Kriegman, M. Olson, E. F. Eriksen, and L. Mindeholm, "Effects of salmon calcitonin on trabecular microarchitecture as determined by magnetic resonance imaging: results from the QUEST study," *J Bone Miner Res,* vol. 20, pp. 1548-1561, Sep 2005.

[13] S. Majumdar, D. Newitt, M. Jergas, A. Gies, E. Chiu, D. Osman, J. Keltner, J. Keyak, and H. Genant, "Evaluation of technical factors affecting the quantification of trabecular bone structure using magnetic resonance imaging," *Bone,* vol. 17, pp. 417-430, 1995.

[14] S. Majumdar, D. Newitt, A. Mathur, D. Osman, A. Gies, E. Chiu, J. Lotz, J. Kinney, and H. Genant, "Magnetic resonance imaging of trabecular bone structure in the distal radius: relationship with X-ray tomographic microscopy and biomechanics," *Osteoporos Int,* vol. 6, pp. 376-385, 1996.

[15] S. Majumdar, R. S. Weinstein, and R. R. Prasad, "Application of fractal geometry techniques to the study of trabecular bone," *Medical Physics,* vol. 20, pp. 1611-1619, 1993.

[16] S. Majumdar, "Magnetic resonance imaging of trabecular bone structure," *Topics in Magnetic Resonance Imaging,* vol. 13, pp. 323-334, 2002.

[17] F. W. Wehrli, G. A. Ladinsky, C. Jones, M. Benito, J. Magland, B. Vasilic, A. M. Popescu, B. Zemel, A. J. Cucchiara, A. C. Wright, H. K. Song, P. K. Saha, H. Peachey, and P. J. Snyder, "In vivo magnetic resonance detects rapid remodeling changes in the topology of the trabecular bone network after menopause and the protective effect of estradiol," *J Bone Miner Res,* vol. 23, pp. 730-40, 2008.

[18] G. Chang, L. Wang, G. Liang, J. S. Babb, P. K. Saha, and R. R. Regatte, "Reproducibility of subregional trabecular bone micro-architectural measures derived from 7-Tesla magnetic resonance images," *European Society for Magnetic Resonance in Medicine & Biology,* vol. 2011 pp. 121-125, 2011

[19] S. Boutroy, M. L. Bouxsein, F. Munoz, and P. D. Delmas, "In Vivo Assessment of Trabecular Bone Microarchitecture by High-Resolution Peripheral Quantitative Computed Tomography " *The Journal of Clinical Endocrinology & Metabolism,* vol. 90, pp. 6508-6515, 2005.

[20] R. Krug, J. Carballido-Gamio, A. J. Burghardt, G. Kazakia, B. H. Hyun, B. Jobke, S. Banerjee, M. Huber, T. M. Link, and S. Majumdar, "Assessment of trabecular bone structure comparing magnetic resonance imaging at 3 Tesla with high-resolution peripheral quantitative computed tomography ex vivo and in vivo," *Osteoporos Int,* vol. 19, pp. 653-661, 2008.

[21] H. M. Macdonald, K. K. Nishiyama, D. A. Hanley, and S. K. Boyd, "Changes in trabecular and cortical bone microarchitecture at peripheral sites associated with 18 months of teriparatide therapy in postmenopausal women with osteoporosis," *Osteoporos Int*, 2010.

[22] C. Graeff, W. Timm, T. N. Nickelsen, J. Farrerons, F. Marin, C. Barker, and C. C. Gluer, "Monitoring teriparatide-associated changes in vertebral microstructure by high-resolution CT in vivo: results from the EUROFORS study," *J Bone Miner Res*, vol. 22, pp. 1426-33, 2007.

[23] P. K. Saha, O. I. Saba, M. Hudson, A. Pick, G. El-Khoury, and E. A. Hoffman, "Trabecular bone structural analysis using 64 multi-detector CT scanner," in *29th Annual Meeting of the American Society for Bone and Mineral Research*, Honolulu, HI, 2007, p. 193.

[24] M. A. Bredella, M. Misra, K. K. Miller, I. Madisch, A. Sarwar, A. Cheung, A. Klibanski, and R. Gupta, "Distal radius in adolescent girls with anorexia nervosa: trabecular structure analysis with high-resolution flat-panel volume CT," *Radiology*, vol. 249, pp. 938-46, 2008.

[25] G. Diederichs, T. M. Link, M. Kentenich, K. Schwieger, M. B. Huber, A. J. Burghardt, S. Majumdar, P. Rogalla, and A. S. Issever, "Assessment of trabecular bone structure of the calcaneus using multi-detector CT: correlation with microCT and biomechanical testing," *Bone*, vol. 44, pp. 976-83, 2009.

[26] J. S. Bauer, T. M. Link, A. Burghardt, T. D. Henning, D. Mueller, S. Majumdar, and S. Prevrhal, "Analysis of trabecular bone structure with multidetector spiral computed tomography in a simulated soft-tissue environment," *Calcif Tissue Int*, vol. 80, pp. 366-73, 2007.

[27] G. Diederichs, T. Link, K. Marie, M. Huber, P. Rogalla, A. Burghardt, S. Majumdar, and A. Issever, "Feasibility of measuring trabecular bone structure of the proximal femur using 64-slice multidetector computed tomography in a clinical setting," *Calcif Tissue Int*, vol. 83, pp. 332-41, 2008.

[28] A. S. Issever, T. M. Link, M. Kentenich, P. Rogalla, A. J. Burghardt, G. J. Kazakia, S. Majumdar, and G. Diederichs, "Assessment of trabecular bone structure using MDCT: comparison of 64- and 320-slice CT using HR-pQCT as the reference standard," *Eur Radiol*, vol. 20, pp. 458-68, 2010.

[29] P. K. Saha, Y. Liu, C. Pauley, T. Burns, J. Torner, and S. M. Levy, "Quantitative bone micro-architecture in young adults using multi-detector CT imaging and volumetric topological analysis – a feasibility study," presented at the American Society for Bone and Mineral Research, San Diego, CA, 2010.

[30] D. Aghassi, R. R. Anderson, and S. González, "Time-sequence histologic imaging of laser-treated cherry angiomas with in vivo confocal microscopy," *Journal of American Academy of Dermatology,* vol. 43, pp. 37-41, 2000.

[31] T. Hildebrand, A. Laib, R. Muller, J. Dequeker, and P. Rüegsegger, "Direct three-dimensional morphometric analysis of human cancellous bone: microstructural data from spine, femur, iliac crest, and calcaneus," *Journal of Bone Mineral Research,* vol. 14, pp. 1167-1174, 1999.

[32] M. L. Bouxsein, S. K. Boyd, B. A. Christiansen, R. E. Guldberg, K. J. Jepsen, and R. Muller, "Guidelines for assessment of bone microstructure in rodents using micro-computed tomography," *J Bone Miner Res,* vol. 25, pp. 1468-86, 2010.

[33] M. Benito, B. Gomberg, F. W. Wehrli, R. H. Weening, B. Zemel, A. C. Wright, H. K. Song, A. Cucchiara, and P. J. Snyder, "Deterioration of trabecular architecture in hypogonadal men," *J Clin Endocrinol Metab,* vol. 88, pp. 1497-1502, 2003.

[34] r. C. H. Chesnut, S. Majumdar, D. C. Newitt, A. Shields, J. V. Pelt, E. Laschansky, M. Azria, A. Kriegman, M. Olson, E. F. Eriksen, and L. Mindeholm, "Effects of salmon calcitonin on trabecular microarchitecture as determined by magnetic resonance imaging: results from the QUEST study," *J Bone Miner Res,* vol. 20, pp. 1548-1561, 2005.

[35] M. Kleerekoper, A. R. Villanueva, J. Stanciu, D. S. Rao, and A. M. Parfitt, "The role of threedimensional trabecular microstructure in the pathogenesis of vertebral compression fractures," *Calcified Tissue International,* vol. 37, pp. 594-597, 1985.

[36] P. K. Saha and F. W. Wehrli, "In vivo assessment of trabecular bone architecture via three-dimensional tensor scale," in *SPIE: Medical Imaging,* San Diego, CA, 2004, pp. 750-760.

[37] P. K. Saha and B. B. Chaudhuri, "3D digital topology under binary transformation with applications," *Computer Vision and Image Understanding,* vol. 63, pp. 418-429, 1996.

[38] P. K. Saha, B. R. Gomberg, and F. W. Wehrli, "Three-dimensional digital topological characterization of cancellous bone architecture," *International Journal of Imaging Systems and Technology,* vol. 11, pp. 81-90, 2000.

[39] M. Ding, "Age variations in the properties of human tibial trabecular bone and cartilage," *Acta Orthop Scand Suppl,* vol. 292, pp. 1-45, 2000.

[40] F. W. Wehrli, G. A. Ladinsky, C. Jones, M. Benito, J. Magland, B. Vasilic, A. M. Popescu, B. Zemel, A. J. Cucchiara, A. C. Wright, H. K. Song, P. K. Saha, H. Peachey, and P. J. Snyder, "In vivo magnetic resonance detects rapid remodeling changes in the topology of the trabecular bone network after menopause and the protective effect of estradiol," *J Bone Miner Res,* vol. 23, pp. 730-40, May 2008.

[41] P. K. Saha, Y. Xu, H. Duan, A. Heiner, and G. Liang, "Volumetric topological analysis: a novel approach for trabecular bone classification on the continuum between plates and rods," *IEEE Trans Med Imaging,* vol. 29, pp. 1821-38, 2010.

[42] Z. M. Oden, D. M. Selvitelli, W. C. Hayes, and E. R. Myers, "The effect of trabecular structure on DXA-based predictions of bovine bone failure," *Calcified Tissue International,* vol. 63, pp. 67-73, 1998.

[43] R. S. Siffert, G. M. Luo, S. C. Cowin, and J. J. Kaufman, "Dynamic relationships of trabecular bone density, architecture, and strength in a computational model of osteopenia," *Bone,* vol. 18, pp. 197-206, 1996.

[44] A. Odgaard, J. Kabel, B. v. Rietbergen, M. Dalstra, and R. Huiskes, "Fabric and elastic principal directions of cancellous bone are closely related," *Journal of Biomechanics,* vol. 30, pp. 487-495, 1997.

[45] P. K. Saha, J. K. Udupa, and D. Odhner, "Scale-based fuzzy connected image segmentation: theory, algorithms, and validation," *Computer Vision and Image Understanding,* vol. 77, pp. 145-174, 2000.

[46] P. K. Saha and J. K. Udupa, "Scale based image filtering preserving boundary sharpness and fine structures," *IEEE Transactions on Medical Imaging,* vol. 20, pp. 1140-1155, 2001.

[47] Y. Liu, P. K. Saha, and Z. Xu, "Quantitative Characterization of Trabecular Bone Micro-Architecture using Tensor Scale and Muti-Detector CT Imaging," presented at the MICCAI, Nice, France, 2012.

[48] Y. Liu, D. Jin, and P. K. Saha, "A New Algorithm for Trabecular Bone Thickness Computation at Low Resolution Achieved under in Vivo Condition," in *International Symposium on Biomedical Imaging: From Nano to Macro*, San Francisco, CA, USA, 2013, pp. 390-393.

[49] R. Pacific, "Chapter 41: Post menopausal osteoporosis: how the hormonal changes of menopause cause bone loss," in *Osteoporosis*. vol. 2, R. Marcus, D. Feldman, and J. Kelsey, Eds., ed San Diego, CA: Academic Press, 2001, pp. 85-102.

[50] r. L. J. Melton, "Epidemiology of spinal osteoporosis," *Spine,* vol. 22, pp. 2-11, 1997.

[51] W. H. O. Report, "Assessment of fracture risk and its application to screening for postmenopausal osteoporosis," World Health Organization, Geneva 1994.

[52] W. C. Hayes, S. J. Piazza, and P. K. Zysset, "Biomechanics of Fracture Risk Prediction by Quantitative Computed Tomography," *Radiological Clinics of North America,* vol. 29, pp. 1-18, 1991.

[53] J. H. Kinney, J. T. Ryaby, D. L. Haupt, and N. E. Lane, "Three-dimensional in vivo morphometry of trabecular bone in the OVX rat model of osteoporosis," *Technol Health Care,* vol. 6, pp. 339-350, 1998.

[54] S. Sarkar, B. H. Mitlak, M. Wong, J. L. Stock, D. M. Black, and K. D. Harper, "Relationships between bone mineral density and incident vertebral fracture risk with raloxifene therapy," *Journal of Bone Mineral Research,* vol. 17, pp. 1-10, 2002.

[55] r. C. H. Chesnut, S. Silverman, K. Andriano, H. Genant, A. Gimona, S. Harris, D. Kiel, M. LeBoff, M. Maricic, P. Miller, C. Moniz, M. Peacock, P. Richardson, N. Watts, and D. Baylink, "A randomized trial of nasal spray salmon calcitonin in postmenopausal women with established osteoporosis: the prevent recurrence of osteoporotic fractures study," *American Journal of Medicine,* vol. 109, pp. 267-276, 2000.

[56] B. L. Riggs and r. L. J. Melton, "Bone turnover matters: the raloxifene treatment paradox of dramatic decreases in vertebral fractures without commensurate increases in bone density," *Journal of Bone Mineral Research,* vol. 17, pp. 11-14, 2002.

[57] M. Parfitt, "Implications of architecture for the pathogenesis and prevention of vertebral fracture," *Bone,* vol. 13, pp. 41-47, 1992.

[58] L. Mosekilde, "Sex differences in age-related loss of vertebral trabecular bone mass and structure-biomechanical consequences," *Bone,* vol. 10, pp. 425-432, 1989.

[59] J. E. Aaron, R. M. Francis, M. Peacock, and N. B. Makins, "Contrasting microanatomy of idiopathic and corticosteroid-induced osteoporosis," *Clinical Orthopedics and Related Research,* pp. 294-305, 1989.

[60] S. N. Hwang, F. W. Wehrli, and J. L. Williams, "Probability-based structural parameters from 3D NMR images as predictors of trabecular bone strength," *Medical Physics,* vol. 24, pp. 1255-1261, 1997.

[61] P. Chavassieux, M. Arlot, and P. J. Meunier, *Clinical use of bone biopsy* vol. 2. New York: Academic Press, 2001.

[62] R. R. Recker, *Bone histomorphometry: techniques and interpretation*. Boca Raton: CRC Press, 1983.

[63] L. Pothuaud, P. Porion, E. Lespessailles, C. L. Benhamou, and P. Levitz, "A new method for threedimensional skeleton graph analysis of porous media: application to trabecular bone microarchitecture," *J Microsc,* vol. 199, pp. 149-161, 2000.

[64] S. Boutroy, M. L. Bouxsein, F. Munoz, and P. D. Delmas, "In Vivo Assessment of Trabecular Bone Microarchitecture by High-Resolution Peripheral Quantitative Computed Tomography," *J Clin Endocrinol Metab,* 2005.

[65] S. Khosla, B. L. Riggs, E. J. Atkinson, A. L. Oberg, L. J. McDaniel, M. Holets, J. M. Peterson, and r. L. J. Melton, "Effects of sex and age on bone microstructure at the ultradistal radius: a population-based noninvasive in vivo assessment," *J Bone Miner Res,* vol. 21, pp. 124-31, 2006.

[66] T. M. Link, "Osteoporosis Imaging: State of the Art and Advanced Imaging," *Radiology,* vol. 263, pp. 3-17, 2012.

[67] A. J. Burghardt, T. M. Link, and S. Majumdar, "High-resolution computed tomography for clinical imaging of bone microarchitecture," *Clin Orthop Relat Res,* vol. 469, pp. 2179-93, 2011.

[68] A. J. Burghardt, K. A. Dais, U. Masharani, T. M. Link, and S. Majumdar, "In vivo quantification of intra-cortical porosity in human cortical bone using hr-pQCT in patients with type II diabetes " *J Bone Miner Res,* vol. 8, p. S450, 2008.

[69] M. Burrows, D. Liu, and H. McKay, "High-resolution peripheral QCT imaging of bone microstructure in adolescents," *Osteoporos Int,* vol. 21, pp. 515-520, 2010.

[70] R. Krug, A. J. Burghardt, S. Majumdar, and T. M. Link, "High-resolution imaging techniques for the assessment of osteoporosis.," *Radiol Clin North Am,* vol. 48, pp. 601-621, 2010.

[71] T. M. Link, V. Vieth, C. Stehling, A. Lotter, A. Beer, D. Newitt, and S. Majumdar, "Highresolution MRI vs multislice spiral CT: which technique depicts the trabecular bone structure best?," *Eur Radiol,* vol. 13, pp. 663-671, 2003.

[72] A. S. Issever, V. Vieth, A. Lotter, N. Meier, A. Laib, D. Newitt, S. Majumdar, and T. M. Link, "Local differences in the trabecular bone structure of the proximal femur depicted with high-spatial-resolution MR imaging and multisection CT " *Acad Radiol,* vol. 9, pp. 1395-1406, 2002.

[73] G. Diederichs, T. M. L. M. Kentenich, K. Schwieger, and M. B. H. A. J. B. S. M. P. R. A. S. Issever, "Assessment of trabecular bone structure of the calcaneus using multi-detector CT: correlation with microCT and biomechanical testing.," *Bone,* vol. 44, pp. 976-983, 2009.

[74] C. Graeff, W. T. T. N. Nickelsen, J. F. F. Marín, C. B. C. C. Glüer, and E. H. R. C. T. S. Group, "Monitoring teriparatide-associated changes in vertebral microstructure by high-resolution CT in vivo: results from the EUROFORS study. ," *J Bone Miner Res,* vol. 22, pp. 1426-1433, 2007.

[75] A. E. Rodríguez-Soto, K. D. Fritscher, B. Schuler, A. S. Issever, T. Roth, F. Kamelger, C. Kammerlander, and M. B. R. S. T. M. Link, "Texture analysis, bone mineral density, and cortical thickness of the proximal femur: fracture risk prediction. ," *J Comput Assist Tomogr* vol. 34, pp. 949-957, 2010.

[76] M. Ito, K. Ikeda, M. Nishiguchi, H. Shindo, M. Uetani, T. Hosoi, and H. Orimo, "Multi-Detector Row CT Imaging of Vertebral Microstructure for Evaluation of Fracture Risk," *J Bone Miner Res,* vol. 20, pp. 1828-1836, 2005.

[77] T. M. Keaveny, "Biomechanical computed tomography-noninvasive bone strength analysis using clinical computed tomography scans.," *Ann N Y Acad Sci* vol. 1192, p. 57, 2010.

[78] T. M. K. P. F. H. M. Singh and L. P. J. P. B. S. L. G. D. M. Black, "Femoral bone strength and its relation to cortical and trabecular changes after treatment with PTH, alendronate, and their combination as assessed by finite element analysis of quantitative CT scans. ," *J Bone Miner Res,* vol. 23, pp. 1974-1982, 2008.

[79] T. Mawatari, H. M. S. Hamai, T. S. Y. Nakashima, K. Okazaki, N. K. S. Sakai, P. F. H. Y. Iwamoto, and T. M. Keaveny, "Vertebral strength changes in rheumatoid arthritis patients treated with alendronate, as assessed by finite element analysis of clinical computed tomography scans: a prospective randomized clinical trial. ," *Arthritis Rheum,* vol. 58, pp. 3340-3349, 2008.

[80] B. Cortet, N. B. P. D. P. Bourel, and A. Cotten, "Marchandise X. In vivo comparison between computed tomography and magnetic resonance image analysis of the distal radius in the assessment of osteoporosis.," *J Clin Densitom,* vol. 3, pp. 15-26, 2000.

[81] T. M. L. S. M. P. Augat, J. C. L. D. Newitt, Y. Lu, and N. E. L. H. K. Genant, "In vivo high resolution MRI of the calcaneus: differences in trabecular structure in osteoporosis patients.," *J Bone Miner Res* vol. 13, pp. 1175-1183, 1998.

[82] S. M. T. M. Link, P. Augat, J. C. Lin, D. Newitt, and N. E. L. H. K. Genant, "Trabecular bone architecture in the distal radius using magnetic resonance imaging in subjects with fractures of the proximal femur. Magnetic Resonance Science Center and Osteoporosis and Arthritis Research Group.," *Osteoporos Int,* vol. 10, pp. 231-239, 1999.

[83] F. W. Wehrli, M. B. Leonard, P. K. Saha, and B. G. Gomberg, "Quantitative high-resolution MRI reveals structural implications of renal osteodystrophy on trabecular and cortical bone," *J Magn Reson Imaging,* vol. 20, pp. 83-89, 2004.

[84] T. M. Link, V. Vieth, C. Stehling, A. Lotter, A. Beer, D. Newitt, and S. Majumdar, "High-resolution MRI vs multislice spiral CT: Which technique depicts the trabecular bone structure best?," *Eur Radiol,* vol. 13, pp. 663-671, 2003.

[85] H. D. N. E. M. H. T. Dana, C. Bougatsos, and R. Chou, "Screening for osteoporosis: an update for the U.S. Preventive Services Task Force.," *Ann Intern Med,* vol. 153, pp. 99-111, 2010.

[86] C. C. Gluer, "A new quality of bone ultrasound research.," *IEEE Trans Ultrason Ferroelectr Freq Control,* vol. 55, pp. 1524-1528, 2008.

[87] M. Barkmann S.Gonnelli, A. S. D. C. Bauer, L.M. Lewiecki, and D. Hans, "Quantitative ultrasound in the management of osteoporosis: the 2007 ISCD Official Positions.," *J Clin Densitom* vol. 11, pp. 163-187, 2008.

[88] M. Reid, D. F. C. Roux, and S. Kolta, "Association of five quantitative ultrasound devices and bone densitometry with osteoporotic vertebral fractures in a population-based sample: the OPUS Study.," *J Bone Miner Res,* vol. 19, pp. 782-793, 2004.

[89] C. Ruffieux and R. Theiler, A. Tyndall, K. Wimpfheimer, P. Burckhardt, "Comparison of three bone ultrasounds for the discrimination of subjects with and without osteoporotic fractures among 7562 elderly women.," *J Bone Miner Res,* vol. 18, pp. 1261-1266, 2003.

[90] D. Bauer, C. Cauley, and T. Black, "Broadband ultrasound attenuation predicts fractures strongly and independently of densitometry in older women. A prospective study. Study of Osteoporotic Fractures Research Group.," *Arch Intern Med* vol. 157, pp. 629-634, 1997.

[91] A. M. Parfitt, C. H. E. Mathews, A. R. Villanueva, M. Kleerekoper, B. Frame, and D. S. Rao, "Relationships between surface, volume, and thickness of iliac trabecular bone in aging and in osteoporosis. Implications for the microanatomic and cellular mechanisms of bone loss," *Journal of Clinical Investigation,* vol. 72, pp. 1396-1409, 1983.

[92] N. J. Garrahan, R. W. Mellish, and J. E. Compston, "A new method for the two-dimensional analysis of bone structure in human iliac crest biopsies," *J Microsc,* vol. 142, pp. 341-349, 1986.

[93] L. A. Feldkamp, S. A. Goldstein, A. M. Parfitt, G. Jesion, and M. Kleerekoper, "The direct examination of three-dimensional bone architecture in vitro by computed tomography," *Journal of Bone and Mineral Research,* vol. 4, pp. 3-11, 1989.

[94] A. Vesterby, H. J. Gundersen, and F. Melsen, "Star volume of marrow space and trabeculae of the first lumbar vertebra: sampling efficiency and biological variation," *Bone,* vol. 10, pp. 7-13, 1989.

[95] A. Vesterby, H. J. Gundersen, F. Melsen, and L. Mosekilde, "Marrow space star volume in the iliac crest decreases in osteoporotic patients after continuous treatment with fluoride, calcium, and vitamin D2 for five years," *Bone,* vol. 12, pp. 33-37, 1991.

[96] R. W. Mellish, M. W. Ferguson-Pell, G. V. Cochran, R. Lindsay, and D. W. Dempster, "A new manual method for assessing two-dimensional cancellous bone structure: comparison between iliac crest and lumbar vertebra," *Journal of Bone and Mineral Research,* vol. 6, pp. 689-696, 1991.

[97] M. Hahn, M. Vogel, M. Pompesius-Kempa, and G. Delling, "Trabecular bone pattern factor--a new parameter for simple quantification of bone microarchitecture," *Bone,* vol. 13, pp. 327-330, 1992.

[98] C. L. Gordon, C. E. Webber, J. D. Adachi, and N. Christoforou, "In vivo assessment of trabecular bone structure at the distal radius from high-resolution computed tomography images," *Physics in Medicine and Biology,* vol. 41, pp. 495-508, 1996.

[99] A. Laib, T. Hildebrand, H. J. Hauselmann, and P. Rüegsegger, "Ridge number density: a new parameter for in vivo bone structure analysis," *Bone,* vol. 21, pp. 541-546, 1997.

[100] T. Hildebrand and P. Rüegsegger, "Quantification of bone microarchitecture with the structure model index," *Computer Methods in Biomechanics and Biomedical Engineering,* vol. 1, pp. 15-23, 1997.

[101] F. W. Wehrli, B. R. Gomberg, P. K. Saha, H. K. Song, S. N. Hwang, and P. J. Snyder, "Digital topological analysis of in vivo magnetic resonance microimages of trabecular bone reveals structural implications of osteoporosis," *Journal of Bone Mineral Research,* vol. 16, pp. 1520-1531, 2001.

[102] M. Rotter, A. Berg, H. Langenberger, S. Grampp, H. Imhof, and E. Moser, "Autocorrelation analysis of bone structure," *J Magn Reson Imaging,* vol. 14, pp. 87-93, 2001.

[103] L. Pothuaud, B. V. Rietbergen, L. Mosekilde, O. Beuf, P. Levitz, C. L. Benhamou, and S. Majumdar, "Combination of topological parameters and bone volume fraction better predicts the mechanical properties of trabecular bone," *J Biomech,* vol. 35, pp. 1091-1099, 2002.

[104] B. Stampa, B. Kuhn, C. Liess, M. Heller, and C. C. Gluer, "Characterization of the integrity of threedimensional Trabecular bone microstructure by connectivity and shape analysis using high-resolution magnetic resonance imaging in vivo," *Top Magn Reson Imaging,* vol. 13, pp. 357-363, 2002.

[105] D. C. Newitt, B. v. Rietbergen, and S. Majumdar, "Processing and analysis of in vivo high-resolution MR images of trabecular bone for longitudinal studies: reproducibility of structural measures and microfinite element analysis derived mechanical properties," *Osteoporos International Journal of Imaging Systems and Technology,* vol. 13, pp. 278-287, 2002.

[106] B. G. Gomberg, P. K. Saha, H. K. Song, S. N. Hwang, and F. W. Wehrli, "Topological analysis of trabecular bone MR images," *IEEE Transactions on Medical Imaging,* vol. 19, pp. 166-174, 2000.

[107] H. W. Chung, F. W. Wehrli, J. L. Williams, S. D. Kugelmass, and S. L. Wehrli, "Quantitative analysis of trabecular microstructure by 400 MHz nuclear magnetic resonance imaging," *Journal of Bone and Mineral Research,* vol. 10, pp. 803-811, 1995.

[108] W. J. Whitehouse, "The quantitative morphology of anisotropic trabecular bone," *J Microsc,* vol. 101 pp. 153-168, 1974.

[109] T. P. Harrigan and R. W. Mann, "Characterization of microstructural anisotropy in orthotropic materials using a second rank tensor," *Journal of Materials Science,* vol. 19, pp. 761-767, 1984.

[110] B. R. Gomberg, P. K. Saha, and F. W. Wehrli, "Topology-based orientation analysis of trabecular bone networks," *Medical Physics,* vol. 30, pp. 158-168, 2003.

[111] S. A. Goldstein, R. Goulet, and D. McCubbrey, "Measurement and significance of three-dimensional architecture to the mechanical integrity of trabecular bone," *Calcif Tissue Int,* vol. 53, pp. 127-132, 1993.

[112] P. K. Saha, B. B. Chaudhuri, and D. D. Majumder, "A new shape preserving parallel thinning algorithm for 3D digital images," *Pattern Recognition,* vol. 30, pp. 1939-1955, 1997.

[113] R. R. Recker, "Architecture and vertebral fracture," *Calcified Tissue International,* vol. 53, pp. 139-142, 1993.

[114] P. Rüegsegger, B. Koller, and R. Müller, "A microtomographic system for the nondestructive evaluation of bone architecture," *Calcif Tissue Int,* vol. 58, pp. 29-24, 1996.

[115] T. Hildebrand and P. Ruegsegger, "A new method for the model-independent assessment of thickness in three-dimension images," *Journal of Microscopy,* vol. 185, pp. 67-75, 1997.

[116] P. K. Saha and F. W. Wehrli, "Measurement of trabecular bone thickness in the limited resolution regime of in vivo MRI by fuzzy distance transform," *IEEE Transactions on Medical Imaging,* vol. 23, pp. 53-62, 2004.

[117] A. Vesterby, H. J. G. Gundersen, and E. Melsen, "Star Volume of Marrow Space and Trabeculae of the First Lumbar Vertebra: Sampling Efficiency and Biological Variation," *Bone,* vol. 10, pp. 7-13, 1989.

[118] P. I. Croucher, N. J. Garrahan, and J. E. Compston, "Assessment of cancellous bone structure: comparison of strut analysis, trabecular bone pattern factor, and marrow space star volume," *J Bone Miner Res,* vol. 11, pp. 955-61, 1996.

[119] D. Marr, *Vision*. San Francisco, CA: W. H. Freeman and Company, 1982.

[120] A. P. Witkin, "Scale-space filtering," presented at the 8th International Joint Conference Artificial Intelligence, Karlsruhe, West Germany, 1983.

[121] J. J. Koenderink, "The structure of images," *Biological Cybernatics,* vol. 50, pp. 363-370, 1984.

[122] T. Lindeberg, "Scale-space for discrete signals," *IEEE Transactions on Pattern Recognition and Machine Intelligence,* vol. 12, pp. 234-254, 1990.

[123] K. L. Vincken, A. S. E. Koster, and M. A. Viergever, "Probabilistic multiscale image segmentation," *IEEE Transactions on Pattern Analysis and Machine Intelligence,* vol. 19, pp. 109-120, 1997.

[124] Y. Leung, J. S. Zhang, and Z. B. Xu, "Clustering by scale space filtering," *IEEE Transactions on Pattern Analysis and Machine Intelligence,* vol. 22, pp. 1396-1410, 2000.

[125] B. C. Lovell and A. P. Bradley, "The multiscale classifier," *IEEE Transactions on Pattern Analysis and Machine Intelligence,* vol. 18, pp. 124-137, 1996.

[126] M. Ferraro, G. Bocclgnone, and T. Caell, "On the representation of image structures via scale space entropy conditions," *IEEE Transactions on Pattern Analysis and Machine Intelligence,* vol. 21, pp. 1190-1203, 1999.

[127] M. Tabb and N. Ahuja, "Multiscale image segmentation by integrated edge and region detection," *IEEE Transactions on Image Processing*, vol. 6, pp. 642-655, 1997.

[128] S. M. Pizer, D. Eberly, and D. S. Fritsch, "Zoom-invariant vision of figural shape: the mathematics of core," *Computer Vision and Image Understanding*, vol. 69, pp. 55-71, 1998.

[129] J. H. Elder and S. W. Zucker, "Local scale control for edge detection and blur estimation," *IEEE Transactions on Pattern Analysis and Machine Intelligence*, vol. 20, pp. 699-716, 1998.

[130] P. Liang and Y. F. Wang, "Local scale controlled anisotropic diffusion with local noise estimate for image smoothing and edge detection," presented at the International Conference in Computer Vision, Bombay, India, 1998.

[131] P. K. Saha, "Tensor scale: a local morphometric parameter with applications to computer vision and image processing," *Computer Vision and Image Understanding*, vol. 99, pp. 384-413, 2005.

[132] J. Weickert, *Anisotropic Diffusion in Image Processing*. Stuttgart, Germany: ECMI Series, Teubner-Verlag, 1998.

[133] B. Burgeth, M. Breuß, L. Pizarro, and J. Weickert, "PDE-driven adaptive morphology for matrix fields," in *Scale Space and Variational Methods in Computer Vision, Lecture Notes in Computer Science*, Berlin, 2009, pp. 247-258.

[134] P. K. Saha, J. C. Gee, Z. Xie, and J. K. Udupa, "Tensor scale-based image registration," in *SPIE: Medical Imaging*, San Diego, CA, 2003, pp. 743-753.

[135] P. K. Saha and F. W. Wehrli, "A robust method for measuring trabecular bone orientation anisotropy at in vivo resolution using tensor scale," *Pattern Recognition*, vol. 37, pp. 1935-1944, 2004.

[136] F. A. Andalo, P. A. V. Miranda, R. d. S. Torres, and A. X. Falcao, "A new shape descriptor based on tensor scale," in *the 8th International Symposium on Mathematical Morphology*, Rio de Janeiro, Brazil, 2007, pp. 141–152.

[137] F. A. Andalo, P. A. V. Miranda, R. d. S. Torres, and A. X. Falcao, "Detecting contour saliences using tensor scale," presented at the IEEE International Conference on Image Processing, 2007.

[138] P. K. Sahoo and S. Soltani, "A survey of thresholding techniques," *Computer Vision Graphics Image Processing*, vol. 41, pp. 233-260, 1988.

[139] S. U. Lee, S. Y. Chung, and R. H. Park, "A comparative performance study of several global thresholding techniques for segmentation," *Computer Vision, Graphics, and Image Processing,* vol. 52, pp. 171-190, 1990.

[140] C. A. Glasbey, "An analysis of histogram based thresholding algorithms," *CVGIP: Graphical Models and Image Processing,* vol. 55, pp. 532-537, 1993.

[141] J. Prewitt and M. Mendelsohn, "The analysis of cell images," *Annals of the New York Academy of Sciences,* vol. 128, pp. 1035-1053, 1966.

[142] W. Doyle, "Operations useful for similarity-invariant pattern recognition," *Journal of the ACM,* vol. 9, pp. 259-267, 1962.

[143] N. Otsu, "A threshold selection methods from grey-level histograms," *IEEE Transactions on Pattern Analysis and Machine Intelligence,* vol. 9, pp. 62-66, 1979.

[144] T. W. Ridler and S. Calvard, "Picture thresholding using an iterative selection method," *IEEE Transactions on System, Man and Cybernetics,* vol. 8, pp. 630-632, 1978.

[145] H. J. Trussell, "Comments on 'picture thresholding using an iterative selection method'," *IEEE Transactions on Systems, Man and Cybernetics,* vol. 9, p. 311, 1979.

[146] W. H. Tsai, "Moment-preserving thresholding: A new approach," *Computer Vision, Graphics, and Image Processing,* vol. 29, pp. 377-393, 1985.

[147] T. Pun, "A new method for gray level picture thresholding using the entropy of the histogram," *Signal Processing,* vol. 2, pp. 223-237, 1980.

[148] A. K. C. Wong and P. K. Sahoo, "A gray-level threshold selection method based on maximum entropy principle," *IEEE Transactions on Systems, Man and Cybernetics,* vol. 19, pp. 866 - 871, 1989.

[149] N. R. Pal and S. K. Pal, "Entropy thresholding," *Signal Processing,* vol. 16, pp. 97-108, 1989.

[150] N. R. Pal and S. K. Pal, "Entropy: A new definition and its applications," *IEEE Transactions on Systems, Man, and Cybernetics,* vol. 21, pp. 1260-1270, 1991.

[151] J. N. Kapur, P. K. Sahoo, and A. K. C. Wong, "A new method for gray-level picture thresholding using the entropy of the histogram," *Computer Vision, Graphics, and Image Processing,* vol. 29, pp. 273-285, 1985.

[152] A. S. Abutableb, "Automatic thresholding of gray-level pictures using two-dimensional entropy," *Computer Vision, Graphics, and Image Processing,* vol. 47, pp. 22-32, 1989.

[153] A. Brink, "Maximum entropy segmentation based on the autocorrelation function of the image histogram," *Journal of Computing and Information Technology,* vol. 2, pp. 77-85, 1994.

[154] C. H. Li and C. K. Lee, "Minimum entropy thresholding," *Pattern Recognition,* vol. 26, pp. 617–625, 1993.

[155] J. Kittler and J. Illingworth, "Minimum error thresholding," *Pattern Recognition,* vol. 19, pp. 41–47, 1986.

[156] S. M. Dunn, D. Harwood, and L. S. Davis, "Local estimation of the uniform error threshold," *IEEE Transactions on Pattern Analysis and Machine Intelligence,* vol. 1, pp. 742-747, 1984.

[157] C. K. Leung and F. K. Lam, "Maximum segmented image information thresholding," *Graphical Models and Image Processing,,* vol. 60, pp. 57-76, 1998.

[158] P. L. Rosin and E. Ioannidis, "Evaluation of global image thresholding for change detection," *Pattern Recognition Letters,* vol. 24, pp. 2345–2356, 2003.

[159] P. Sahoo, C. Wilkins, and J. Yeager, "Threshold selection using Renyi's entropy," *Pattern Recognition,* vol. 30, pp. 71-84, 1997.

[160] S. Di Zenzo, L. Cinque, and S. Levialdi, "Image thresholding using fuzzy entropies," *IEEE Trans Syst Man Cybern B Cybern,* vol. 28, pp. 15-23, 1998.

[161] W. Oh and W. B. Lindquist, "Image thresholding by indicator kriging," *IEEE Transactions on Pattern Analysis and Machine Intelligence,* vol. 21, pp. 590-602, 1999.

[162] M. P. d. Albuquerque, I. A. Esquef, A. R. G. Mello, and M. P. d. Albuquerque, "Image thresholding using Tsallis entropy," *Pattern Recognition Letters,* vol. 25, pp. 1059-1065, 2004.

[163] P. K. Sahoo and G. Arora, "Image thresholding using two-dimensional Tsallis-Havrda-Charvát entropy," *Pattern Recognition Letters,* vol. 27, pp. 520-528, 2006.

[164] C. Tsallis, "Possible generalization of Boltzmann-Gibbs statistics," *J. Stat. Phys.,* vol. 52, pp. 480-487, 1988.

[165] H. R. Tizhoosh, "Image thresholding using type II fuzzy sets," *Pattern Recognition,* vol. 38, pp. 2363 – 2372, 2005.

[166] Y. Bazi, L. Bruzzone, and F. Melgani, "Image thresholding based on the EM algorithm and the generalized Gaussian distribution," *Pattern Recognition,* vol. 40, pp. 619 - 634, 2007.

[167] D. Trier and T. Taxt, "Evaluation of Binarization Methods for Document Images," *IEEE Transactions On Pattern Analysis And Machine Intelligence,* vol. 17 pp. 312-315, 1995.

[168] Y. Solihin and C. G. Leedham, "Integral ratio: A new class of global thresholding techniques for handwriting images," *IEEE Trans. Pattern Anal. Mach. Intell,* vol. 21, pp. 761-768, 1999.

[169] J. Sauvola and M. Pietaksinen, "Adaptive document image binarization," *Pattern Recognition,* vol. 33, pp. 225-236, 2000.

[170] K. Ramar, S. Arunigam, S. N. Sivanandam, L. Ganesan, and D. Manimegalai, "Quantitative fuzzy measures for threshold selection," *Pattern Recogn. Lett.,* vol. 21, pp. 1-7, 2000.

[171] C. M. Tsai and H. H. Lee, "Binarization of color document images via luminance and saturation color features," *IEEE Trans. Image Processing,* vol. 11, pp. 434-451 2002.

[172] Y. Yang and H. Yan, "An adaptive logical method for binarization of degraded document images," *Pattern Recognition,* vol. 33, pp. 787-807, 2002.

[173] P. K. Saha and B. B. Chaudhuri, "Detection of 3D simple points for topology preserving transformation with application to thinning," *IEEE Transactions on Pattern Analysis and Machine Intelligence,* vol. 16, pp. 1028-1032, 1994.

[174] P. K. Saha, B. B. Chaudhuri, B. Chanda, and D. D. Majumder, "Topology preservation in 3D digital space," *Pattern Recognition,* vol. 27, pp. 295-300, 1994.

[175] A. Bonnassie, F. Peyrin, and D. Attal, "A new method for analyzing local shape in three-dimensional images based on medial axis transformation," *IEEE Trans. Syst. Man Cybern,* vol. 33, pp. 700–705, 2003.

[176] T. Hildebrand and P. Rüegsegger, "A new method for the model independent assessment of thickness in three-dimensional images," *Journal of Microscopy,* vol. 185, pp. 67-75, 1997.

[177] R. Moreno, M. Borga, and Ö. Smedby, "Estimation of trabecular thickness in gray-scale images through granulometric analysis," presented at the SPIE: Medical Imaging, San Diego, CA, 2012.

[178] Y. Liu, D. Jin, and P. K. Saha, "A new algorithm for trabecular bone thickness computation at low resolution achieved under in vivo condition," presented at the International Symposium on Biomedical Imaging, San Francisco, CA, 2013 (to appear).

[179] G. Borgefors, "On digital distance transformation in three dimensions," *Computer Vision Graphics Image Processing,* vol. 64, pp. 368-376, 1996.

[180] P. K. Saha, F. W. Wehrli, and B. R. Gomberg, "Fuzzy distance transform: theory, algorithms, and applications," *Computer Vision and Image Understanding,* vol. 86, pp. 171-190, 2002.

[181] P. K. Saha, Y. Xu, H. Duan, A. Heiner, and G. Liang, "Volumetric topological analysis: a novel approach for trabecular bone classification on the continuum between plates and rods," *IEEE Trans Med Imaging,* vol. 29, pp. 1821-38, Nov 2010.

[182] T. M. Keaveny, R. E. Borchers, L. J. Gibson, and W. C. Hayes, "Trabecular bone modulus and strength can depend on specimen geometry," *J Biomech,* vol. 26, pp. 991-1000, 1993.

[183] C. J. Hernandez, G. S. Beaupre, T. S. Keller, and D. R. Carter, "The influence of bone volume fraction and ash fraction on bone strength and modulus," *Bone,* vol. 29, pp. 74-8, Jul 2001.

[184] Z. Xu, S. Dasgupta, and P. K. Saha, "Tensor Scale: An Analytic Approach with Efficient Computation and Applications," *Computer Vision and Image Understanding,* vol. 116, pp. 1060-1075, 2012.

[185] F. L. Bookstein, "Fitting conic sections to scattered data," *Computer Graphics and Image Processing,* vol. 9, pp. 56-71, 1979.

[186] A. Fitzgibbon, M. Pilu, and R. B. Fisher, "Direct least square fitting of ellipses," *IEEE Transactions on Pattern Analysis and Machine Intelligence,* vol. 21, pp. 476-480, 1999.

[187] P. L. Rosin, "A note on the least squares fitting of ellipses," *Pattern Recognition Letters,* vol. 14, pp. 799-808, 1993.

[188] N. Otsu, "A threshold selection methods from grey-level histograms," *IEEE Trans. Pattern Anal. Mach. Intell.,* vol. 9, pp. 62–66, 1979.

[189] T. W. R. Calvard, "Picture thresholding using an iterative selection method," *IEEE Trans Syst. Man Cybern,* vol. 8, pp. 630–632, 1978.

[190] H. J. Trussell, "Comments on 'picture thresholding using an iterative selection method'," *IEEE Trans. Syst. Man Cybern.,* vol. 9, p. 311, 1979.

[191] W. H. Tsai, "Moment-preserving thresholding: A new approach," *Comput. Vis. Graph. Image Process.*, vol. 29, pp. 377–393, 1985.

[192] T. Pun, "A new method for gray level picture thresholding using the entropy of the histogram," *Signal Process.*, vol. 2, pp. 223–237, 1980.

[193] A. K. C. Wong and P. K. Sahoo, "A gray-level threshold selection method based on maximum entropy principle," *IEEE Trans. Syst. Man Cybern.*, pp. 866–871, 1989.

[194] N. R. Pal and S. K. Pal, "Entropy thresholding," *Signal Process.*, vol. 16, pp. 97–108, 1989.

[195] N. R. Pal and S. K. Pal, "Entropy: A new definition and its applications," *IEEE Trans. Syst. Man Cybern.*, vol. 21, pp. 1260–1270, 1991.

[196] J. N. Kapur, P. K. Sahoo, and A. K. C. Wong, "A new method for graylevel picture thresholding using the entropy of the histogram," *Comput. Vis. Graph. Image Process.*, vol. 29, pp. 273–285, 1985.

[197] A. S. Abutableb, "Automatic thresholding of gray-level pictures using two-dimensional entropy," *Comput. Vis. Graph. Image Process.* , vol. 47, pp. 22–32, 1989.

[198] A. Brink, "Maximum entropy segmentation based on the autocorrelation function of the image histogram," *J. Comput. Inf. Technol.*, vol. 2, pp. 77–85, 1994.

[199] S. M. Dunn, D. Harwood, and L. S. Davis, "Local estimation of the uniform error threshold," *IEEE Trans. Pattern Anal. Mach. Intell.*, vol. 1, pp. 742–747, 1984.

[200] C. K. Leung and F. K. Lam, "Maximum segmented image information thresholding," *Graph. Models Image Process.* , vol. 60, pp. 57–76, 1998.

[201] J. Prewitt and M. Mendelsohn, "The analysis of cell images," *Ann. N. Y. Acad. Sci.* , vol. 128, pp. 1035–1053, 1966.

[202] W. Doyle, "Operations useful for similarity-invariant pattern recognition," *J. ACM*, vol. 9, pp. 259–267, 1962.

[203] P. K. Sahoo and S. Soltani, "A survey of thresholding techniques," *Comput. Vis. Graph. Image Process*, vol. 41, pp. 233–260, 1988.

[204] S. U. Lee, S. Y. Chung, and R. H. Park, "A comparative performance study of several global thresholding techniques for segmentation," *Comput. Vis. Graph. Image Process.* , vol. 52, pp. 171–190, 1990.

[205] C. A. Glasbey, "An analysis of histogram based thresholding algorithms," *CVGIP: Graph. Models Image Process,* vol. 55, pp. 532–537, 1993.

[206] P. K. Saha and J. K. Udupa, "Optimum threshold selection using class uncertainty and region homogeneity," *IEEE Transactions on Pattern Analysis and Machine Intelligence,* vol. 23, pp. 689-706, 2001.

[207] M. Sonka, V. Hlavac, and R. Boyle, *Image Processing, Analysis, and Machine Vision, Third Edition*. Pacific Grove, CA: PWS Publishing, 2007.

[208] C. E. Shannon and W. Weaver, *The Mathematical Theory of Communication*. Champaign, IL: University of Illinois Press, 1964.

[209] P. Soille and M. Ansoult, "Automated basin delineation from DEMs using mathematical morphology," *Signal Processing,* vol. 20, pp. 171-182, 1990.

[210] L. Vincent and P. Soille, "Watersheds in digital spaces: An efficient algorithm based on immersion simulations," *IEEE Transactions on Pattern Analysis and Machine Intelligence,* vol. 13, pp. 583-598, 1991.

[211] ITK. *The NLM Insight Segmentation and Registration Toolkit*. Available: http://www.itk.org

[212] E. Filho, Y. Saijo, A. Tanaka, T. Yambe, S. Li, and M. Yoshizawa, "Automated calcification detection and quantification in intravascular ultrasound Images by adaptive thresholding," presented at the World Congress on Medical Physics and Biomedical Engineering, COEX Seoul, Korea, 2007.

[213] I. P. Pappas, M. Styner, P. Malik, L. Remonda, and M. Caversaccio, "Automatic method to assess local CT-MR imaging registration accuracy on images of the head," *AJNR Am. J. Neuroradiol,* vol. 26, pp. 137–144, 2005.

[214] Y. Yang, S. Huang, and N. Rao, "An automatic hybrid method for retinal blood vessel extraction," *Int. J. Appl. Math. Comput. Sci.,* vol. 18, pp. 399–407, 2008.

[215] K. V. Asari, T. Srikhanthan, S. Kumar, and D. Radhakrishnan, "A pipelined architecture for image segmentation by adaptive progressive thresholding," *J. Microprocess. Microsyst.,* vol. 23, pp. 493–499, 1999.

[216] S. Kumar, K. V. Asari, and D. Radhakrishnan, "Real-time automatic extraction of luman region and boundary from endoscopic images," *Med. Biol. Eng. Comput.* , vol. 37, pp. 600–604, 1999.

[217] H. Tian, T. Srikanthan, and K. V. Asari, "Automatic segmentation algorithm for the extraction of lumen region and boundary for exdoscopic images," *Med. Biol. Eng. Comput.,* vol. 39, pp. 8–14 2001.

[218] S. Arseneau and J. R. Cooperstock, "Real-time image segmentation for action recognition," presented at the IEEE Pacijk Rim Conference on Computers and Signal Processing, Victoria, B. C., Canada, 1999.

[219] L. Eikvil, T. Taxt, and K. Moen, "A fast method for adaptive binarization," presented at the 1st International Conference Document Analysis and Recognition, St. Malo, France, 1991.

[220] P. Li, A. L. Abbot, and D. L. Schmoldt, "Automated analysis of CT images for the inspection of hardwood logs," presented at the IEEE International Confernece on Neural Networks, Washington D.C., 1996.

[221] J. W. Miller, V. Shridhar, E. Wicker, and C. Griffth, "Very low-cost in-process gauging system," presented at the IEEE Pacific Rim Confernece on Communications, Computers and Signal Processing, Victoria, B.C., Canada, 1999.

[222] R. A. Brooks, L. G. Mitchell, C. M. O. Connor, and G. D. Chiro, "On the relationship between computed tomography numbers and specific gravity," *Phys. Med. Biol.,* vol. 26, pp. 141–147, 1981.

[223] J. A. Kanis, "Diagnosis of osteoporosis and assessment of fracture risk," *Lancet,* vol. 359, pp. 1929-36, 2002.

[224] J. A. Kanis and W. S. Group, "Assessment of Fracture Risk and its Application to Screening for Postmenopausal Osteoporosis: Synopsis of a WHO Report," *Osteoporosis Int,* vol. 4, pp. 368-381, 1994.

[225] B. Sander, V. E. Gibson, D. E. Beaton, E. R. Bogoch, and A. Maetzel, "A Coordinator Program in Post-Fracture Osteoporosis Management Improves Outcomes and Saves Costs," *THE JOURNAL OF BONE AND JOINT SURGERY,* vol. 90, pp. 1197-1205, 2008.

[226] J. D. L. Gay, "Radial fracture as an indicator of osteoporosis: a 10-year follow-up study," *Can Med Assoc J,* vol. 111, pp. 156-157, 1974.

[227] r. C. H. Chesnut, A. Skag, C. Christiansen, R. Recker, J. A. Stakkestad, A. Hoiseth, D. Felsenberg, H. Huss, J. Gilbride, R. C. Schimmer, and P. D. Delmas, "Effects of Oral Ibandronate Administered Daily or Intermittently on Fracture Risk in Postmenopausal Osteoporosis," *JOURNAL OF BONE AND MINERAL RESEARCH,* vol. 19, pp. 1241-1249, 2004.

[228] B. Ettinger, D. M. Black, B. H. Mitlak, R. K. Knickerbocker, T. Nickelsen, H. K. Genant, C. Chistiansen, P. D. Delmas, J. R. Zanchetta, J. Stakkestad, C. C. Gluer, K. Krueger, F. J. Cohen, S. Eckert, K. E. Ensrud, L. V. Avioli, P. Lips, and S. R. Cummings, "Reduction of Vertebral Fracture Risk in Postmenopausal Women

with Osteoporosis Treated with Raloxifene," *Journal of American Medical Association,* vol. 282, pp. 637-646, 1999.

[229] P. J. Meunier, C. Roux, E. Seeman, S. Ortolani, J. E. Badurski, T. D. Spector, J. Cannata, A. Balogh, E. Lemmel, S. Pors-Nielsen, R. Rizzoli, H. K. Genant, and J. Reginster, "The Effects of Strontium Ranelate on the Risk of Vertebral Fracture in Women with Postmenopausal Osteoporosis," *The New England Journal of Medicine,* vol. 350, pp. 459-438, 2004.

[230] E. S. Siris, P. D. Miller, E. B. Connor, K. G. Faulkner, L. E. Wehren, T. A. Abbott, M. L. Berger, A. C. Santora, and L. M. Sherwood, "Identification and fracture outcomes of undiagnosed low bone mineral density in postmenopausal women," *Journal of American Medical Association,* vol. 286, pp. 2815-2823, 2001.

[231] P. D. Miller, E. S. Siris, E. B. Connor, K. G. Faulkner, L. E. Wehren, T. A. Abbott, Y. Chen, M. L. Berger, A. C. Santora, and L. M. Sherwood, "Prediction of Fracture Risk in Postmenopausal White Women With Peripheral Bone Densitometry: Evidence From the National Osteoporosis Risk Assessment," *JOURNAL OF BONE AND MINERAL RESEARCH,* vol. 17, pp. 2222-2230, 2002.

[232] N. Crabtree, N. Loveridge, M. Parker, N. Rushton, J. Power, K. L. Bell, T. J. Beck, and J. Reeve, "Intracapsular Hip Fracture and the Region-Specific Loss of Cortical Bone: Analysis by Peripheral Quantitative Computed Tomography," *JOURNAL OF BONE AND MINERAL RESEARCH,* vol. 16, pp. 1318-1328, 2001.

[233] D. Picard, J. P. Brown, L. Rosenthall, M. Couturier, J. Lévesque, M. Dumont, L.-G. Ste-Marie, A. Tenenhouse, and S. Dodin, "Ability of Peripheral DXA Measurement to Diagnose Osteoporosis As Assessed By Central DXA Measurement," *Journal of Clinical Densitometry,* vol. 7, pp. 111-118, 2004.

[234] P. D. Miller, S. L. Bonnick, C. C. J. Jr., M. Kleerekoper, R. L. Lindsay, L. M. Sherwood, and E. S. Siris, "The Challenges of Peripheral Bone Density Testing," *Journal of Clinical Densitometry,* vol. 1, pp. 211-217, 1998.